HELLENIC REPUBLIC
UNIVERSITY OF IOANNINA
SCHOOL OF SCIENCES
DEPARTMENT OF MATERIALS SCIENCE AND ENGINEERING

Theory-guided bottom-up design of low-rigidity Ti-based alloys (ab initio and molecular dynamics simulations)

JOSÉ JULIO GUTIÉRREZ MORENO

PhD THESIS

IOANNINA 2014

HELLENIC REPUBLIC
UNIVERSITY OF IOANNINA
SCHOOL OF SCIENCES
DEPARTMENT OF MATERIALS SCIENCE AND ENGINEERING

Theory-guided bottom-up design of low-rigidity Ti-based alloys (ab initio and molecular dynamics simulations)

JOSÉ JULIO GUTIÉRREZ MORENO

PhD THESIS

IOANNINA 2014

Η έγκριση της διδακτορικής διατριβής από το Τμήμα Μηχανικών Επιστήμης Υλικών της Σχολής Θετικών Επιστημών του Πανεπιστημίου Ιωαννίνων δεν υποδηλώνει αποδοχή των γνωμών του συγγραφέα Ν. 5343/32, άρθρο 202, παράγραφος 2

Ημερομηνία αίτησης της/του κ. José Julio Gutiérrez Moreno: 10.03.2011
Ημερομηνία ορισμού Τριμελούς Συμβουλευτικής Επιτροπής: 16.03.2011

Μέλη Τριμελούς Συμβουλευτικής Επιτροπής:
Επιβλέπουσα
Λέκκα Χριστίνα, Επίκουρος Καθηγήτρια του Τ.Μ.Ε.Υ. του Πανεπιστημίου Ιωαννίνων
Μέλη
Ευαγγελάκης Γεώργιος, Καθηγητή του Τμήματος Φυσικής του Πανεπιστημίου Ιωαννίνων
Παπαγεωργίου Δημήτριος, Αναπληρωτής Καθηγητής του Τ.Μ.Ε.Υ. του Πανεπιστημίου Ιωαννίνων

Ημερομηνία ορισμού θέματος: 16.03.2011

Theory-guided bottom-up design of low rigidity Ti-based alloys (ab initio and molecular dynamics simulations)

ΔΙΟΡΙΣΜΟΣ ΕΠΤΑΜΕΛΟΥΣ ΕΞΕΤΑΣΤΙΚΗΣ ΕΠΙΤΡΟΠΗΣ:

Λέκκα Χριστίνα, Επίκουρος Καθηγήτρια του Τ.Μ.Ε.Υ. του Πανεπιστημίου Ιωαννίνων

Ευαγγελάκης Γεώργιος, Καθηγητή του Τμήματος Φυσικής του Πανεπιστημίου Ιωαννίνων

Παπαγεωργίου Δημήτριος, Αναπληρωτή Καθηγητή του Τ.Μ.Ε.Υ. του Πανεπιστημίου Ιωαννίνων

Καλπακίδης Βασίλειος, Καθηγητή του Τ.Μ.Ε.Υ. του Πανεπιστημίου Ιωαννίνων

Φωτιάδης Δημήτριος, Καθηγητή του Τ.Μ.Ε.Υ. του Πανεπιστημίου Ιωαννίνων

Λοιδωρίκης Ελευθέριος, Αναπληρωτή Καθηγητή του Τ.Μ.Ε.Υ. του Πανεπιστημίου Ιωαννίνων

Γεργίδης Λεωνίδας, Επίκουρος Καθηγητής του Τ.Μ.Ε.Υ. του Πανεπιστημίου Ιωαννίνων

Έγκριση Διδακτορικής Διατριβής με βαθμό **«ΑΡΙΣΤΑ»** στις **12.11.2014**

Ο Πρόεδρος του Τμήματος

Καρακασίδης Μιχαήλ
Καθηγητής

Η Γραμματέας του Τμήματος

Ξανθή Τουτουνζόγλου

Abstract

This thesis investigates the structural, electronic and mechanical properties of Ti-based alloys aiming in understanding the electronic origin of low-rigidity materials suitable as metallic implants. This necessity is originated from the currently used Ti-6Al-4V metallic implants that consist of cytotoxic elements (causing diseases) and exhibit higher Young's moduli (E) (~112GPa) than that of the bone (E < 30GPa) (resulting in bone atrophy and implant loosening). Therefore, a second generation of Ti-based alloys was proposed consisting with non-toxic β-stabilizers like Nb, which although reduced by almost half the Young's modulus, the bone-like E values are still unreachable.

Starting from the Ti-Nb alloy, the ab initio calculations predict several Ti-Nb phases (α', β, α" and ω) depending on the Nb concentration, in line with experimental observations. The α' and ω are energetically favoured for Ti-xNb ($x \leq 6.25$%at), the β phase is stable at high Nb compositions ($x \geq 18.75$at%) while the α" phase may exist in intermediate stoichiometries. The Young's moduli (E) follows the $E_{\omega} > E_{\alpha'} > E_{\alpha''} > E_{\beta}$ sequence, revealing high E_{ω} and $E_{\alpha'}$ values (> 120GPa) and although the E_{β} converges to 87GPa, the coexistence of all phases affects significantly the E reduction. The calculated Young's modulus surface revealed high anisotropic E values for all Ti-Nb phases, while interestingly the E_{β} along the [100] direction exhibits really low values (below 30GPa) suggesting the importance of a Ti-Nb single-crystal growth for the design of low rigidity alloys, especially at small Nb substitutions.

In order to investigate an alternative pathway for reducing the rigidity, *sp* or *sd*-dopants were added in the Ti-xNb ($x \geq 18.75$at%) alloys. For the *sp*-dopant Ti-25at%Nb-x(Sn/In) ($x < 6.25$%at) alloys, new energy states below the Ti-Nb valence band with anti-bonding character are introduced, explaining the experimentally observed E decrease (down to 49GPa), while high *sp*-substitutions ($x \geq 12.5$at%) result in β-phase destabilization. For the s*d*-electron dopant, Hf (11at%) may act as precursor of the $\alpha'' \rightarrow \beta$ phase transition when is substituted in the α″ Ti-18.75at%Nb alloy. This is attributed to Hf-Hf first and second neighbour interactions that introduce new well localized Hf 4f energy states (-11eV) only at the high Hf substitutions (> 12.5at%), thus affecting the calculated band energy and inducing β-phase stability.

Finally, the *sd*-electron Ti-Zr-Hf alloys were studied by molecular dynamics

simulations that yielded disordered polycrystalline structures with E = 64GPa, which although lower than the Ti-6Al-4V, it is unfortunately comparable to the β-Ti-25at%Nb E values.

Acknowledgments

We have no cause for anything but gratitude and joy, so I would like to start my thesis expressing my gratitude to all people that contributed doing the work carried out during this period more bearable. For this reason I would like to make participant of this thesis to all people who helped me, each in his/her own way, during the last years.

First of all I would like to express my most sincere gratitude to my PhD supervisor, Assistant Professor Christina Lekka for her trust and constant support from the very first moment. I would like to thank her for introducing me in the world of density functional theory calculations as well as for her involvement in the research project together with her help and attention in extra-scientific issues. I would like to extend my deepest gratitude to Professor Georgios Evangelakis for his kind help, guidance, fruitful discussion and very important contribution to this work. In addition, I would like to thank Associated Professor Dimitrios Papageorgiou, who was always ready to help all times I knocked on his office's door and for his training on molecular dynamics simulations. Moreover I would like to mention Mr. Konstantinos Dimakopoulos and Mr. Konstantinos Prouskas for their indispensable technical support. I would also like also to thank Associated Professor Eleftherios Lidorikis, Professor Vasileios Kalpakidis, Professor Dimitrios Fotiadis and Assistant Professor Leonidas Gergidis for being members of the dissertation committee.

This thesis is especially dedicated to my parents and my grandparents who always supported me in the distance. In special to my grandfather, whose dream was to see myself graduated as a PhD. Also to all the good friends I have made along these years in Ioannina, who are actually too many to write their names here, and who were constant support in my everyday life. I am very glad to have met you all during these amazing years. I will miss you. Lastly I would like to acknowledge the entire BioTiNet network, in special the ESR and ER for the great time spent together in our numerous meetings and the BioTiNet ITN (No. 264635) FP7 Marie Curie project for the economic support.

Abbreviations

APW	Augmented Plane Waves
APW+lo	Augmented Plane Waves with local orbitals
B	Bulk Modulus
bcc	Body Centered Cubic
DFT	Density Functional Theory
E	Young's Modulus
E_b	Band Energy
EDOS	Electronic Density of States
E_F	Fermi Energy
G	Shear Modulus
hcp	Hexagonal Closely Packed
H-K	Hohenberg - Kohn
K-S	Kohn – Sham
LAPW	Linearized Augmented Plane Waves
LAPW+LO	Linearized Augmented Plane Waves with local orbitals
MD	Molecular Dynamics
MT	Muffin Tin
PW	Plane Waves
VRH	Voigt-Reuss-Hill
XRD	X-Ray Diffraction
ν	Poisson's Ratio

Contents

CHAPTER 1: Introduction

1.1 Biomedical implants 1

1.1.1 Present and future perspectives 1

1.1.2 Biomaterials 1

1.1.3 Biocompatibility 4

1.1.4 Mechanical biocompatibility 4

1.2 Titanium and Titanium-based alloys for biomedical applications 6

1.2.1 Titanium and Ti-alloys as a biomaterial 6

1.2.2 β-Ti alloys 7

1.2.3 Shape Memory Alloys 9

1.3 Structural and mechanical characteristics of Titanium and Ti-Nb alloys 10

1.3.1 Pure Ti 10

1.3.2 Ti-Nb alloys 11

1.3.3 Young's modulus of Ti-Nb alloys 16

1.4 References 18

CHAPTER 2: Theoretical background

2.1 Density Functional Theory 23

2.1.1 Quantum many-body problem 23

2.1.2 The Born-Oppenheimer approximation 23

2.1.3. Density Functional Theory 24

2.1.4 Total energy in terms of density …….. 26

2.1.5 The exchange-correlation functional …… 30

2.1.6 Approximations to exchange and correlation …….. 30

a) Local Density Approximation (LDA) ……. 30

b) Generalized Gradient Approximation (GGA) ……..... 31

2.1.7 Augmented Plane Wave Method (APW) ……..... 32

2.1.8 Linearized Augmented Plane Wave Method (LAPW) ……... 33

2.1.9 Linearized Augmented Plane Wave + Local Orbitals Method (LAPW+LO) ……. 34

2.1.10 The Augmented Plane Wave Method + Local Orbitals method (APW+lo) 35

2.2 Molecular Dynamics …… 36

2.2.1 Molecular Dynamics ……..... 36

2.2.2 Interatomic potential …… 39

2.3 Theory of Elasticity …….. 39

2.3.1 Hooke's law ……. 39

2.3.2 Voigt's notation ……... 40

2.3.3 Strain and Energy …… 41

2.3.4 Elastic Stability ……..... 42

2.3.5 Voigt-Reuss-Hill approximation ...……... 43

2.3.6 Young's modulus surface …… 45

2.4 Computational details …….. 45

2.4.1 Ab initio simulations ……... 45

2.4.2 Molecular Dynamics simulations …… 48

2.5 References ……... 51

CHAPTER 3: Results

3.1 Ti-Nb alloys …….. 55

3.3.1 Introduction……... 55

3.3.2 Results and discussion ……. 56

a) Structural properties …….. 56

b) Electronic properties ……. 60

c) Mechanical properties ……... 66

i) Elastic stiffness and mechanical stability ……. 66

ii) Elastic properties …… 68

3.3.3 Conclusions ……..... 75

3.4.4 References …… 77

3.2 Ti-Nb-Hf alloys …..…….... 80

3.3.1 Introduction …….. 80

3.3.2 Results and discussion ……. 81

a) Structural and mechanical properties …… 81

b) Electronic properties ……. 84

3.3.3 Conclusions ……. 89

3.4.4 References …… 90

3.3 Ti-Nb-In alloys ……. 92

3.3.1 Introduction ……. 92

3.3.2 Results and discussion ……..... 92

a) Structural properties …….. 92

b) Electronic properties ……. 95

c) Mechanical properties ……... 100

3.3.3 Conclusions …….. 100

3.4.4 References …… 102

3.4 Ti-Nb-Sn alloys ……..... 104

3.4.1 Introduction …….. 104

3.4.2 Results and discussion ……. 104

a) Structural and mechanical properties …… 104

b) Electronic properties ……. 106

3.4.4 Conclusions …….. 111

3.4.5 References …… 112

3.5 Ti-Zr-Hf alloys ……. 114

3.4.1 Introduction ……. 114

3.4.2 Results and discussion ……. 115

3.4.3 References …… 118

CHAPTER 4: Conclusions

4.1 Concluding remarks …….. 120

4.2 Future work …… 123

ANNEX

- **Dissemination ……. 124**
  - **Scientific publications ……. 124**
  - **Dissemination in conferences ……. 125**

SUPPLEMENTARY MATERIAL

- **Electronic Density of States …….. 128**

CHAPTER 1: Introduction

1.1 Biomedical implants

1.1.1 Present and future perspectives

Musculoskeletal disorders are recognized as among the most significant human health problems that exist today while it has been estimated that 90% of population over the age of 40 suffers from these kinds of diseases. The demand for bone replacement and repair is directly related with the continuous aging of the population and the changing lifestyle habits within the last decades [1]. The most common reasons for joint replacements (Figure 1.1.1) are attributed to diseases such as osteoporosis (weakening of the bones), osteoarthritis (inflammation in the bone joints) and trauma. Nevertheless not only the replacement surgeries have increased, but also the revision surgery due to failures of the implants (Figure1.1.2). Nowadays due to the advancement in medical technology people live longer, thus the implants are now expected to serve for much longer period or until lifetime without failure or revision surgery. Unfortunately the materials available on the market for bone repair and replacement do not satisfy all clinical desires. Due to these reasons, development of appropriate material with high longevity and excellent biocompatibility is essential. Consequently, a very high uptrend in implant manufacturing (Figure 1.1.1) is expected in coming years.

1.1.2 Biomaterials

Biomaterials are artificial or natural materials, used in the productions of structures or implants, with the aim of replacing the lost or diseased biological fractions. They may also help in improving the quality of life and longevity of human beings, that's the reason why the field of biomaterials has grown rapidly to keep with the demands of a continuous aging population. Biomaterials are used in different parts of the human body as cardiovascular implants (heart valves, pacemaker cases, stents in blood vessels…), artificial bones and implants (screws or plates in shoulders, knees, hips, elbows…) as well as orthodontic structures [2].

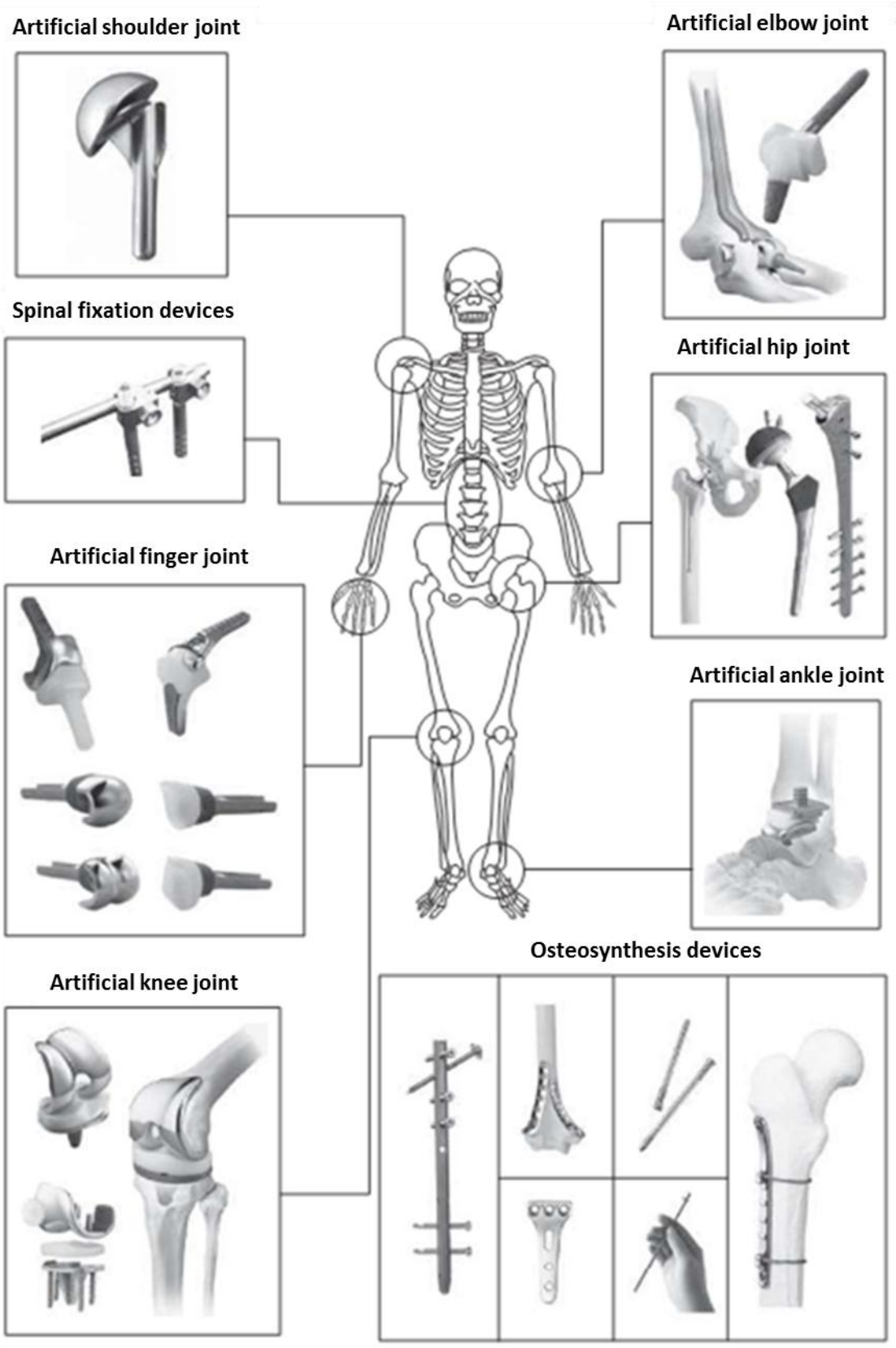

Figure 1.1.1 *Various bone-related implants used in vivo for orthopaedic surgery [2].*

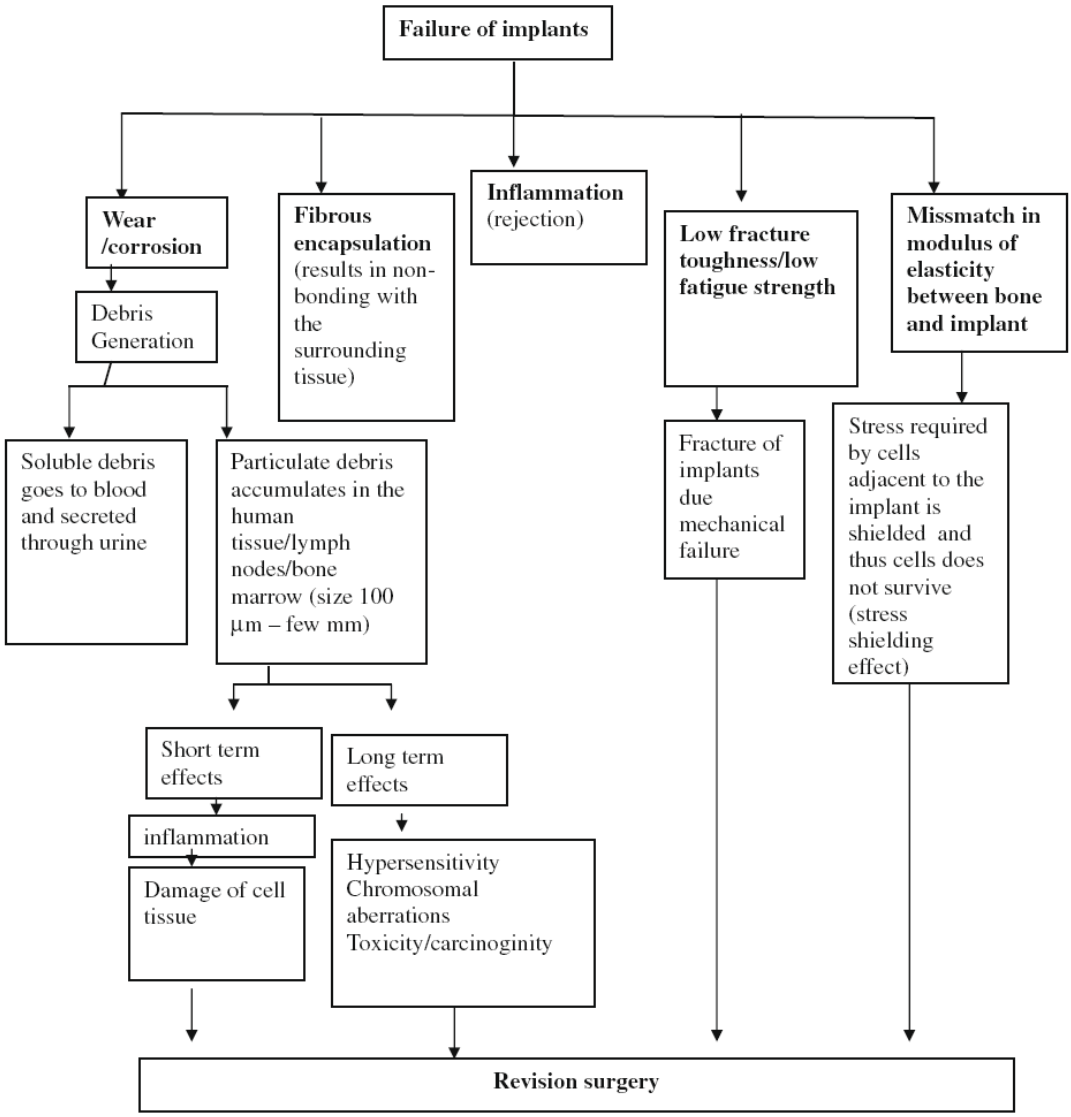

Figure 1.1.2 *Various causes for failure of implants that require revision surgery [3].*

Some of these applications are shown in Figure 1.1.1 [4-6]. The success of biomaterials in the body depends on factors such as the material properties, design, and biocompatibility, as well as other factors not under the control of the materials engineer, including the technique used by the surgeon, the health and condition of the patient, and the activities of the patient. The design and selection of biomaterials depend on the future application. Development of new biomaterials is an interdisciplinary effort between physicists, material scientists and engineers, biomedical engineers, pathologists and clinicians. Suitable materials for biomedical implants should possess excellent biocompatibility, corrosion resistance in body environment, along with combination of high strength, low modulus, high fatigue, wear resistance and high ductility Table (1.1.1) [7-9].

REQUIREMENTS OF IMPLANTS

COMPATIBILITY	MECHANICAL PROPERTIES	MANUFACTURING

• Tissue reactions
• Changes in properties
  • Mechanical
  • Physical
  • Chemical
• Degradation leads to
  • Local deleterious changes
  • Harmful systemic effects
	• Elasticity
	• Yield stress
	• Ductility
	• Toughness
	• Time dependent deformation
	• Creep
	• Ultimate strength
	• fatigue strength
	• Hardness
	• Wear resistance
		• Fabrication methods
		• Consistency and conformity to all requirements
		• Quality of raw materials
		• Superior techniques to obtain excellent surface finish or texture
		• Capability of material to get safe and efficient sterilization
		• Cost of product

Table 1.1.1 *Implant materials requirements for the desing of orthopaedical applications [10].*

1.1.3 Biocompatibility

The materials used as implants are expected to be non-toxic and should not cause any inflammatory or allergic reactions in the human body. The success of the biomaterials mainly depends on the reaction of the human body, like the host response induced by the material and its degradation in the body [11]. The ability of the implant's surface to integrate with the adjacent bone and other tissues is another important factor and the lack of this biointegration may cause different side effects like allergic reactions or stress shielding as shown on Figure 1.1.2. If the implant is not well integrated with the bone, a fibrous tissue is formed between the bone and the implant [12], which results in implant loosening. The biocompatibility of different pure metals is discussed on Table 1.1.2 and Figure 1.1.3. Consequently, bioactive materials are highly preferred as they give rise to high integration with surrounding bone. Nevertheless bio-tolerant implants are also accepted for implant manufacturing. Hence, materials with an appropriate surface are highly essential for the implant to integrate well with the adjacent bone. Surface chemistry, surface roughness and surface topography all play a major role in the development of good osseointegration.

1.1.4 Mechanical biocompatibility

Properties like hardness, tensile strength, modulus and elongation are of prime importance for biomedical applications.

Periodic position	Element	Biocompatible	Carcinogenic	Genotoxic	Mutagenic	Cytotoxic	Allergenic	Prone to corrosion	Other*
3d	Ti	Yes	No	No	No	Med	No	No	No
	V	No	Yes	Yes	Yes	High	Disputed	No	No
	Cr	No	Disputed	Yes	Yes	High	Yes	No	No
	Mn	No	No	Yes	No	High	No	Yes	No
	Fe	No	No	Yes	Disputed	Med	No	Yes	No
	Co	No	Yes	Yes	Yes	High	Yes	Yes	Yes
	Ni	No	Yes	Yes	Yes	High	Yes	Yes	Yes
	Cu	No	No	Yes	Yes	High	Yes	Yes	Yes
4d	Zr	Yes	No	No	No	Low	No	No	No
	Nb	Yes	No	No	No	Low	No	No	No
	Mo	No	Disputed	Yes	Yes	Low	Yes	Yes	Yes
	Tc	No	- Radioactive -						
	Ru	Yes	No	No	No	Med	No	No	Yes
	Rh	No	Yes	Yes	Yes	High	Unknown	No	No
	Pd	No	Yes	No	Disputed	Med	Yes	No	No
	Ag	No	No	No	No	High	Yes	No	Yes
5d	Hf	Unknown	Unknown	Unknown	Unknown	Med	No	No	Unknown
	Ta	Yes	No	No	No	Low	No	No	No
	W	No	Yes	Yes	No	Med	No	Yes	No
	Re	Unknown	Unknown	Unknown	Unknown	Unknown	No	No	Unknown
	Os	No	Unknown	Yes	Yes	High	No	Yes	No
	Ir	No	No	No	Yes	High	No	No	Yes
	Pt	No	Yes	Yes	Yes	High	Yes	No	No
	Au	Yes	No	No	No	High	No	No	No
Other	Al	No	No	Yes	No	Low	No	No	Yes
	Zn	No	No	No	No	High	No	No	Yes
	Sn	Yes	No	No	No	Low	No	No	Yes

Table 1.1.2 *Biological impact on the human body for various pure metals. Red indicates a serious concern, yellow a moderated concern and green a minimal or no concern [13].*

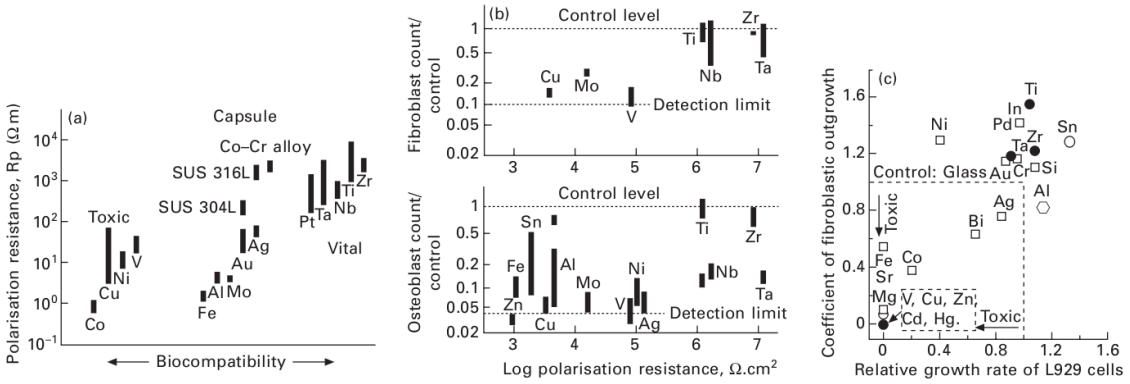

Figure 1.1.3 *Relationship between the polarization resistance and biocompatibility of various pure metals and alloys. Cytotoxicity of various pure metals [14].*

The metals currently used for bone implants are much stiffer than the bone, thus the implant carries a disproportionate amount of the loads while the bone is stress-shielded. This mechanical mismatch between the bone and implant can lead to bone resorption and implants loosening; thus the material for replacing bone is expected to have a

modulus equivalent to that of the bone. The bone modulus varies in the magnitude from 4GPa to 30GPa depending on the type of the bone [15, 16]. The current implant materials which have higher stiffness than the bone (Figure 1.1.4) cannot prevent the transferred stress to adjacent bone [17]. Any reduction in the stiffness of the implant is expected to enhance the stress redistribution to the adjacent bone tissues, therefore minimizing the stress shielding effect may result prolonging of the device's lifetime. Summarizing, deal biomaterials for a hard tissue are required not only to reveal excellent biocompatibility but also to combine high strength and low-Young's modulus (< 30GPa) in order to meet the demands for a long-service life and implantation.

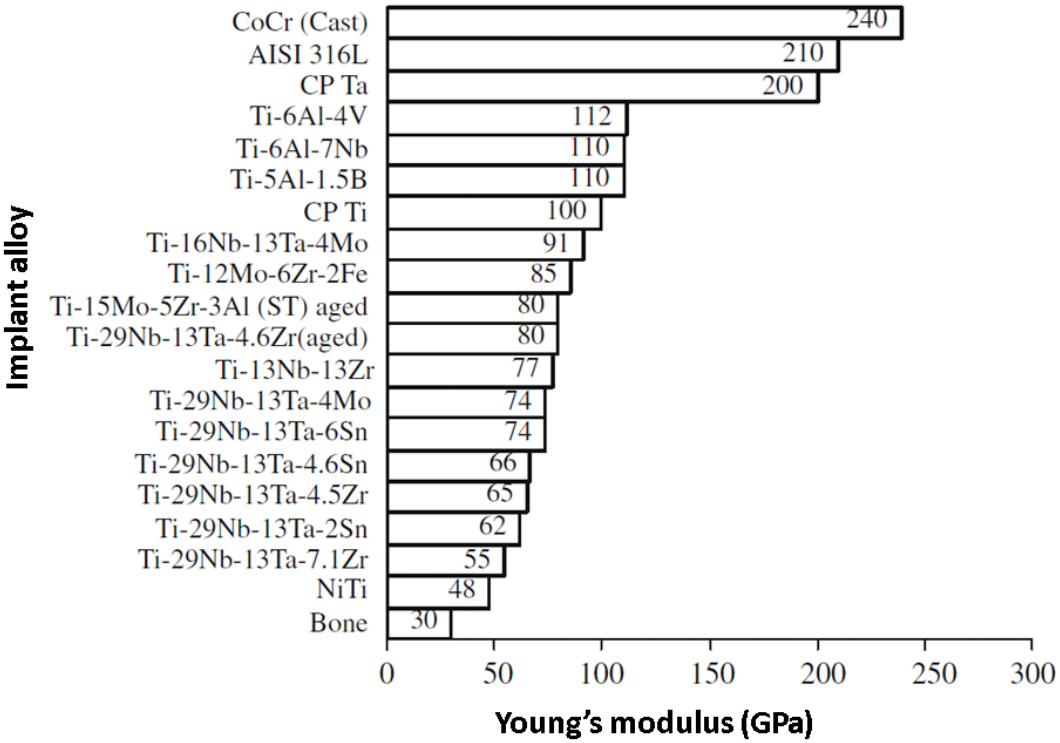

Figure 1.1.4 *Young's moduli values of various orthopedic alloys [3].*

1.2 Titanium and Titanium-based alloys for biomedical applications

1.2.1 Titanium and Ti-alloys as a biomaterial

For load-bearing orthopedic applications, several types of materials including polymers, metals, ceramics and composites are currently in use. Nevertheless, metals have so far shown the greatest potential and consequently they are used for the majority of the

applications due to their excellent mechanical strength and resilience when compared to alternative biomaterials, such as polymers and ceramics (table 1.2.1). In particular, titanium alloys are the first choice for the majority of applications such as artificial hip joints and dental roots because of their high biocompatibility, high strength, long fatigue life, formability, machinability and corrosion resistance [17].

Materials	Advantages	Disadvantages	Examples
Polymers (nylon, silicone rubber, polyester, polytetrafuoroethylene, etc.)	Resilient Easy to fabricate	Not strong Deforms with time, may degrade	Sutures, blood vessels, hip socket, ear, nose, other soft tissues, sutures
Metals (Ti and its alloys, Co-Cr alloys, stainless steels, Au, Ag, Pt, etc.)	Strong, tough, ductile	May corrode, dense, difficult to make	Joint replacements, bone plates and screws, dental root implants, pacer and suture wires
Ceramics (aluminum oxide, calcium phosphates including hydroxyapatite, carbon)	Very biocompatible, inert, strong in compression	Brittle, not resilient, difficult to make	Dental; femoral head of hip replacement, coating of dental and orthopedic implants
Composites (carbon-carbon, wire or fiber reinforced bone cement)	Strong, tailor-made	Difficult to make	Joint implants, heart valves

Table 1.2.1 *Biomaterials for use in the body [7].*

Titanium and its Ti-6Al-4V alloy are used since 1950s as implant biomaterials. Nevertheless, they are continuously a subject of various modifications concerning the alloy's composition (e.g. Ti–6Al–7Nb, Ti– 5Al–2.5Fe) [7, 9, 19] and their surface properties [20] due to their high mechanical strength and fracture toughness [3, 7, 9, 19-21]. That is in order to meet the needs for improved function and duration of an implant in the human body. Unfortunately, these materials have exhibited tendencies to fail after long-term use [3, 7, 9, 19, 21] due to various reasons such as high modulus (E_{Ti} = 110GPa and $E_{Ti\text{-}6Al\text{-}4V}$ = 120GPa) compared to that of a cortical bone (E < 30GPa) and lack of biocompatibility [3, 7]. The mechanical mismatch leads, as was described in the section 1.1.4 (Mechanical Biocompatibility), to bone resorption around the implant which will cause tissue loss and implant failure. In order to design novel materials suitable for biomedical applications, the research must be focused in the investigation of low-rigidity alloys that fulfill all the biocompatibility requirements.

1.2.2 β-Ti alloys

Ti alloys are grouped into α, (α + β), and β-type alloys. Young's moduli of α and (α + β)-type titanium alloys such as Ti and Ti-6Al-4V are higher than those of β-type titanium alloys (Figure 1.2.2). Therefore, β-type titanium alloys are advantageous for the development of titanium alloys with low Young's modulus for biomedical

applications [23]. For this reason, nowadays β-type titanium alloys which are composed by non-toxic and allergy-free elements are developed for biomedical applications due to their low Young's moduli, approximately below 80GPa, which is favorable for homogeneous stress transfer between implant and bone [24].

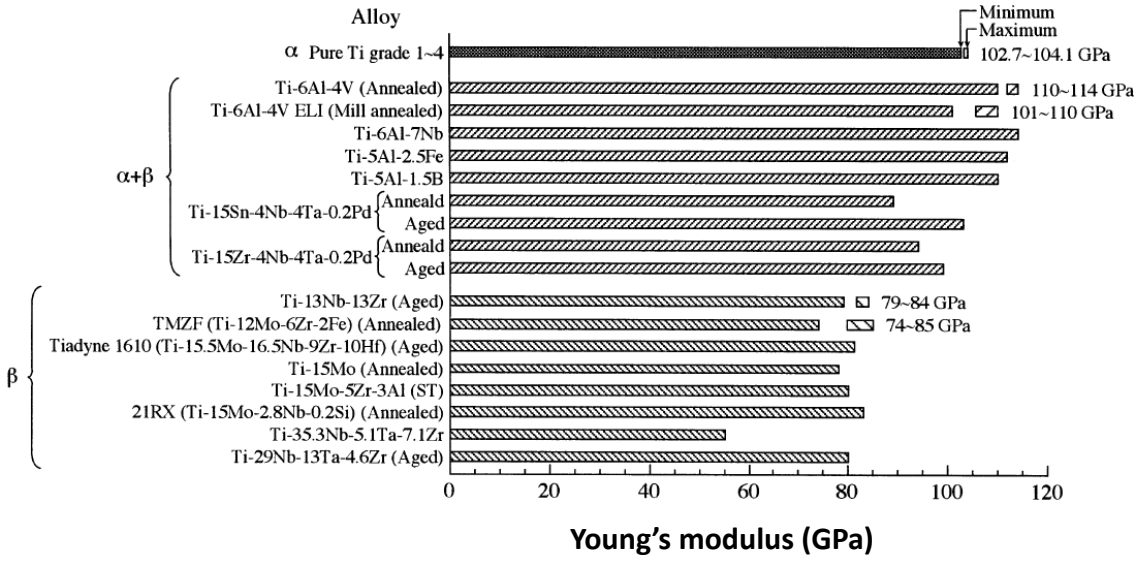

Figure 1.2.1 *Comparison of Young's moduli of various titanium alloy classified by crystalline structure and casting methodology [22].*

The lowest value of Young's modulus reported for the polycrystalline *β*-type titanium alloy, Ti-35Nb-4Sn [25], or Ti-24Nb-4Zr-7.9Sn [26], is around 40GPa. Young's modulus bellow 40GPa was never measured in polycrystalline biocompatible bulk Ti-based alloys. Nevetheless, in β-Ti alloys the Young's modulus exhibits a very anisotropic deformation behavior that is highly dependent on the crystal growth direction [27-30]. Therefore, although a single-crystal β-Ti alloy grown in a selected direction may exhibit enhanced elasticity, detailed studies related to these issues to our knownledge are lacking. In addition, the manufacture of porous alloys [31] is very effective for further reduction of the Young's moduli of titanium and its alloys. It is known that pores with appropriate sizes enhance the bone growth and remodeling, but on the other hand the strength decreases drastically with increasing porosity. Summarizing, among the mechanical biocompatibilities, Young's modulus has a significant importance in the final success of the materials for orthopaedics and its reduction has received considerable attention during the last years.

1.2.3 Shape Memory Alloys

Shape memory alloys (SMAs) are a unique class of metallic materials that can exhibit shape memory effect (SME) and superelasticity (SE). A shape memory material is initially deformed at low temperature and then recovers its original shape upon heating. Superelasticity represents elastic recovery of strains up to 10% during the loading-unloading cycle at appropriate temperatures [13]. Shape memory alloys (SMAs) are one of the most successful materials for the manufacturing of novel medical implants like coronary stents [32, 33]. In particular, nitinol (equiatomic TiNi alloy) SMA have been successfully applied as biomedical materials (Figure 1.2.2), due to their superior shape memory properties, strength, superelasticity, corrosion resistance and absence of magnetic properties. Unfortunately the toxic, allergenic and carcinogenic properties of nickel [34] have stimulated the development of SMA without the cited undesirable side effects.

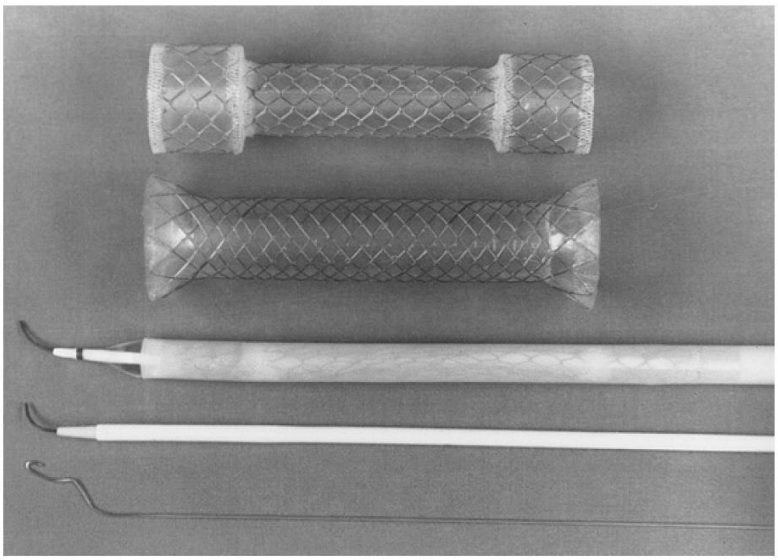

Figure 1.2.2 *Photograph shows, from top to bottom, a type A stent, type B stent, stent introducer set (guide wire, balloon catheter, compressed stent, sheath), stent retrieval set (guide wire, dilator, sheath),and hook wire [33].*

The β-type Ti alloys are known to exhibit a martensitic transformation from β to orthorhombic α″ martensite above a critical alloying content. In fact superelasticity has been observed in Ti–Nb binary alloys at room temperature and a number of authors have attempted the production of biocompatible Ti–Nb(-X) SMAs (X = Zr, Ta, Au, O) with superelastic strains up to 4.2% [35-37] However, while α″ orthorhombic Ti-based alloys are promising, their Young's modulus is significantly higher compared to human

bone [38] or to β-type Ti alloys [39]. The achievement of lower Young's moduli as well as the development of new SMA is a topic of increasing interest within the biomedical industry.

1.3 Structural and mechanical characteristics of Ti and Ti-Nb alloys

1.3.1 Pure Ti

Nowadays titanium is one of the most important metals in the industry. The element was first discovered in England by W. Gregor in 1790 [40]. Nevertheless, Ti received its denomination, by M.H. Klaproth five years later, in reference to the "Titans" who was the mythological first sons of the Earth. Chemically, titanium is one of the transition elements in group IV and period 4 of Mendeleev's periodic table. It has the atomic number 22 and its atomic weight is 47.9. Titanium is a transition element and has an incompletely filled d shell in its electronic structure [41].

This incomplete shell enables titanium to form solid solutions with many other substitutional elements. In the elemental form, titanium has a high melting point (1668 ºC) and possesses hexagonal closely packed crystal structure (hcp) up to the temperature of 882 ºC; above which titanium is transformed into the body centered cubic structure (bcc) structure [42].

At high pressure and room temperature, Titanium is transformed to the ω phase. About 25 years ago, Moffat et al. reported [43] that the presence of the ω phase in Ti-based alloys is a modification of the β phase of pure titanium. The P-T diagram of Ti (Figure 1.3.1) reveals that although ω is not a stable phase at room conditions, it can be more stable than the β phase at low temperature and high pressure conditions. Interestingly, the Ti's ω phase is retained even if the Ti is pressurized to ω at room temperature (P > 9GPa) and then returned to atmospheric pressure. In order to alter this behavior Ti must be annealed at higher temperatures ($T_{\omega\rightarrow\alpha} = 380$ ºC) [44].

1.3.2 Ti-Nb alloys

It is well known that only two stable solid phases exist in the Ti-Nb binary alloy system, α –phase hcp ($P6_3/mmc$) and β-phase bcc ($Im\bar{3}m$) (Figure 1.3.2). As we can see in (Figure 1.3.2) above 882 ºC, all Ti-Nb alloys are in solid phase and form single β-phase.

Quenching from this phase, the β- structure persists in the alloys which have Nb compositions greater than ~25% at [43, 45, 46].

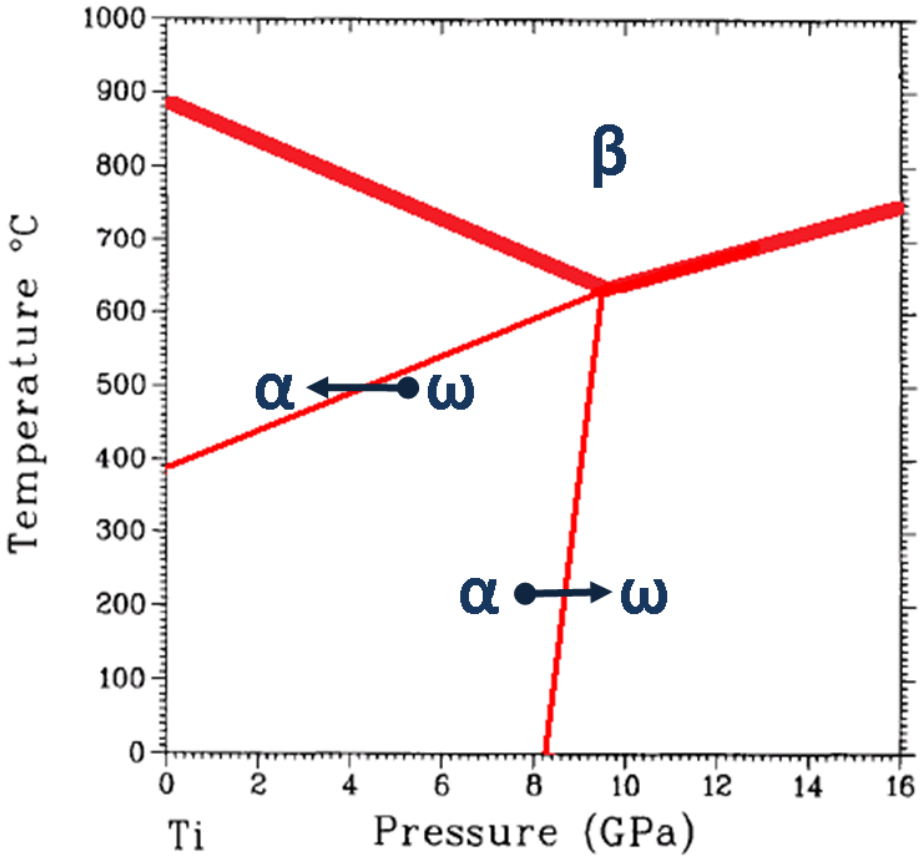

Figure 1.3.1 *The pressure-temperature phase diagram of pure titanium [43, 44].*

Burgers [48] originally proposed the orientational relationship between the bcc and hcp phase as: $[0001]_\alpha \parallel [110]_\beta$ and $[11\bar{2}0]_\alpha \parallel [111]_\beta$

A combination of shuffle, shear, and volume dilatation can lead to this transformation (Figure 1.3.3) [49, 50, 51] consisting in:

ii) A shuffle displacement of the $[011]_\beta$ planes in the $\langle 1\bar{1}0 \rangle$ directions. Displacement amplitude of $\sqrt{2}/12$ times of the bcc lattice leads to the exact hcp stacking sequence.

ii) A shear such as $[1\bar{1}2]\ \langle \bar{1}11 \rangle$ and $[\bar{1}12]\ \langle 1\bar{1}1 \rangle$ to squeeze the bcc octahedron into a regular hcp one. The angle of the hcp face in the basal plane changes from 70.53º to 60º.

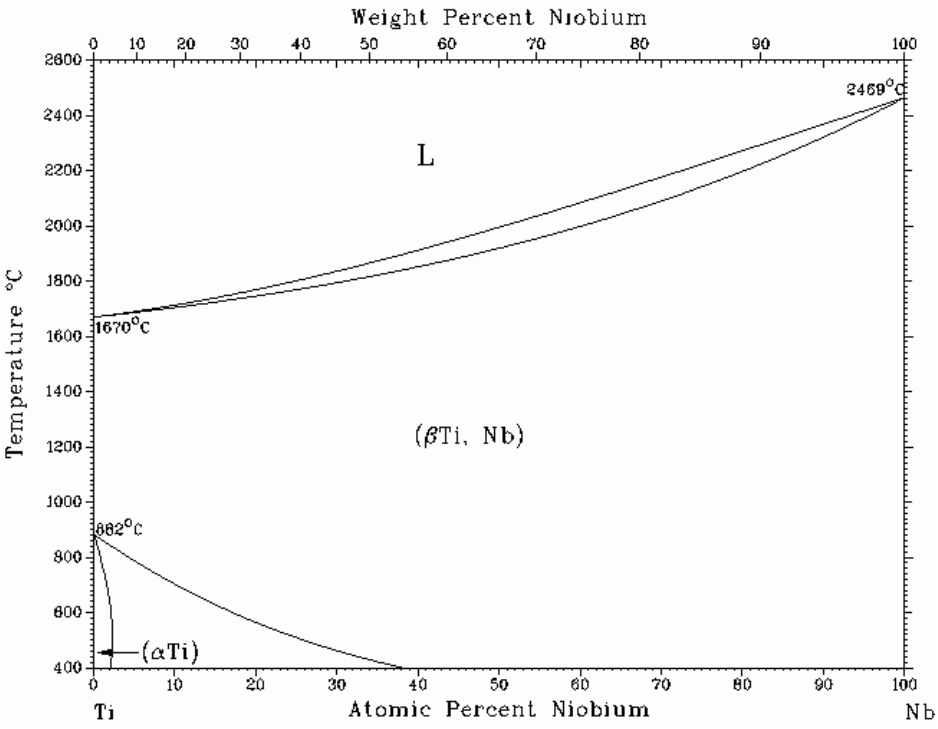

Figure 1.3.2 *Nb-Ti phase diagram [47].*

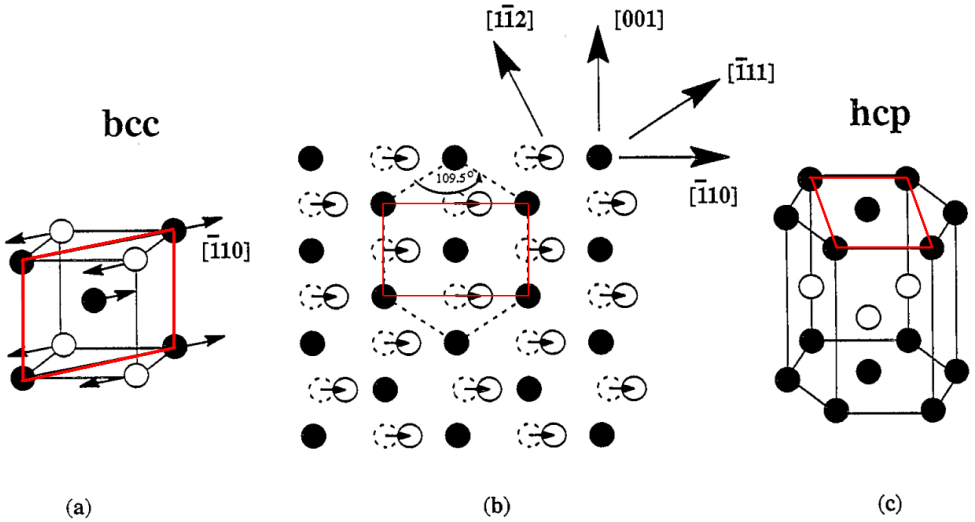

Figure 1.3.3 *Schematic representation of the bcc to hcp transformation [52].*

However the β→α transformation may allow the formation of martensites phases. The stabilization of α′ and α″ phases along with the presence of ω grains have been detected in these binary alloys *[37, 43, 53]*.

A T_0 curve (β→α, β→ω, α→ω) (Figure 1.3.4) gives the points at which the free energies of two phases are equal. The implication of this effect is that at temperatures

equal or below T_0, a single-phase alloy of one crystal structure may transform to another single-phase structure without a change in composition. Among other factors, if a diffusionless transformation produces strain in the matrix, additional driving force will be required to overcome this. As a result, the actual transformation temperature will be below T_0 [54] Thus, since α' and α" are martensitic forms of α, the martensite starting temperature (M_S) should be below $T_0^{\beta\to\alpha}$. Similarly, the $T_0^{\beta\to\omega}$ curve shows the region where ω precipitates could be formed during quenching.

It is important to clarify that the α-phase will correspond to the stable hcp ($P6_3/mmc$) structure, while the α′-phase is formed under martensitic transformation. In other words, although both exhibit identical structures and the same lattice parameters, they are experimentally formed after different procedures. Obviously this β to α′ transformation obeys the bcc/hcp Burger's orientation.

It is important to clarify that the α-phase will correspond to the stable hcp ($P6_3/mmc$) structure, while the α′-phase is formed under martensitic transformation. In other words, although both exhibit identical structures and the same lattice parameters, they are experimentally formed after different procedures. Obviously this β to α′ transformation obeys the bcc/hcp Burger's orientation.

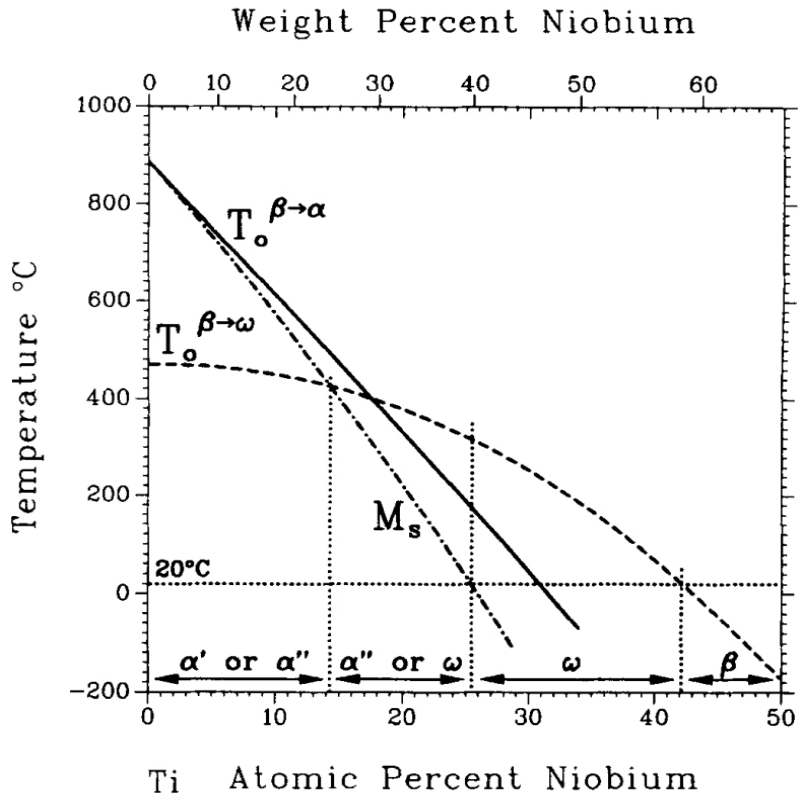

Figure 1.3.4 *Calculated T_0 and the experimental M_S curves [43].*

The transformation of β to α′ can be accomplished by [42]

i) a 10% contraction along $[100]_{\beta}$which corresponds to $[2\bar{1}\bar{1}0]_{\alpha}$

ii) a 10% expansion along $[01\bar{1}]_{\beta}$ which corresponds to $[01\bar{1}0]_{\alpha}$

iii) a 1% expansion along $[011]_{\beta}$ which corresponds to $[0001]_{\alpha}$

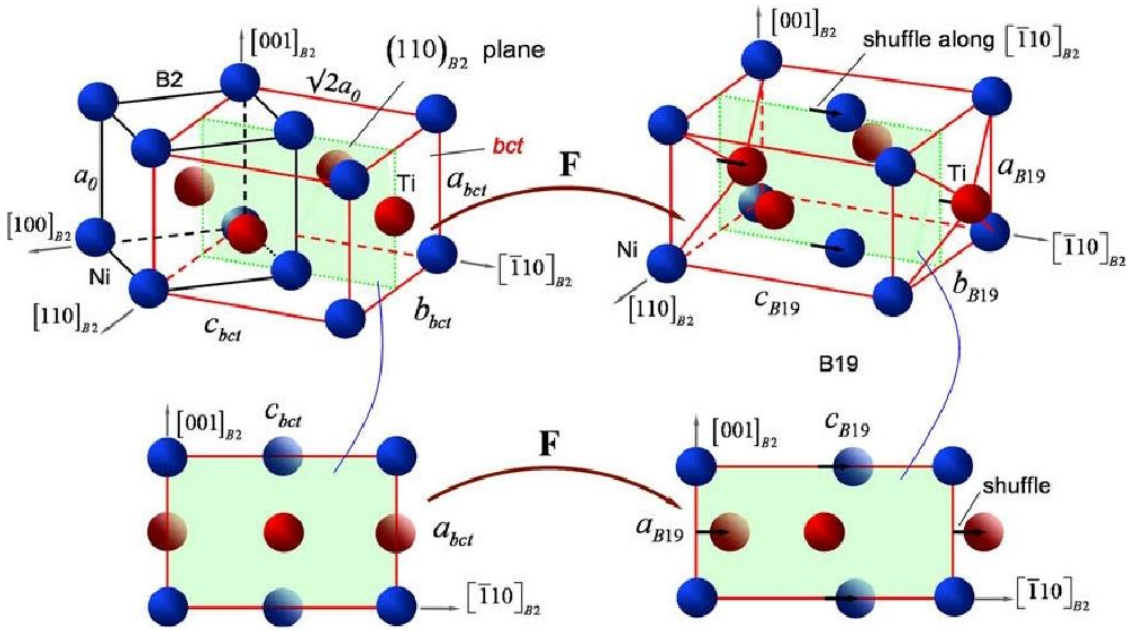

Figure 1.3.5 *Schematic B2 (bcc) to B19 (α″ orthorhombic phase) transformation in NiTi. Also shown are the* $[110]_{B2}$ *projections (equivalent to* $[100]_{B19}$ *projections) of two lattices to illustrate clearly the cell deformations and shuffles involved in the transformation [58].*

The α″ structure may be viewed as a transition between the hcp and bcc structures. By adjusting y, b and c, someone can produce all three structures [56]. For example, a hcp structure is obtained when y =1/6 and $b/a = \sqrt{3}$ (the ideal c/a for hcp is $c/a = \sqrt{8/3}$). A bcc structure (Figure 1.3.6) is obtained when y = 1/4 and $b/a = c/a = \sqrt{2}$.

The α″ is C-centered (space group Cmcm) orthorhombic [55] with atomic positions (0, 0, 0), (0,-2y, 1/2), (1/2, 1/2, 0), (1/2, 1/2-2y, 1/2) where y has been estimated to have a value around 0.2 for Ti-Nb alloys although it may vary with composition. The β→α″ transition in NiTi, which is analogous to the same transformation in TiNb alloys, is schematically shown in Figure 1.3.5.

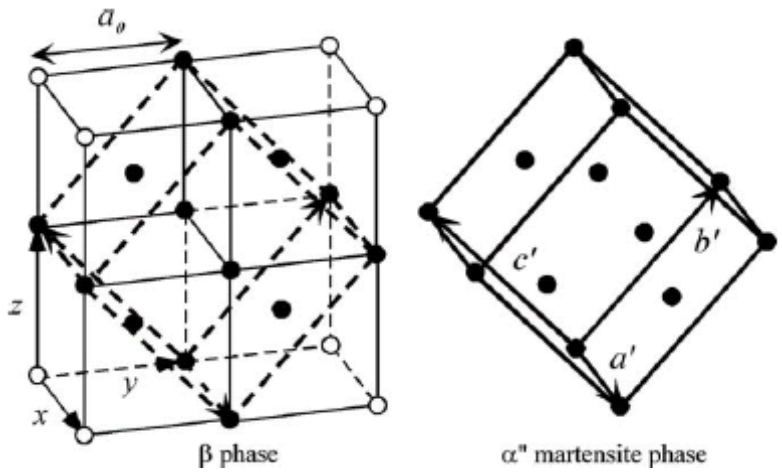

Figure 1.3.6 *Schematic illustration exhibiting the lattice correspondence between β and α″ phase [37].*

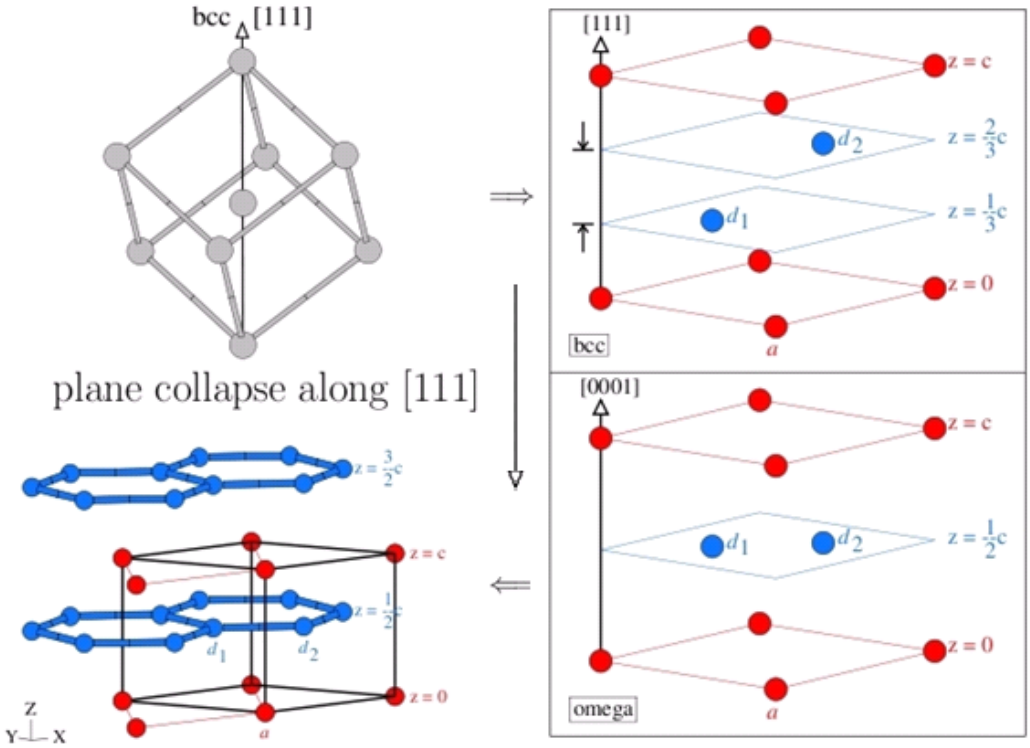

Figure 1.3.7 *Plane collapse of bcc along [111] to produce ω. The (111) planes are stacked in a pattern that repeats every three planes. Note that the distance between (111) planes is exaggerated by 100% to more clearly illustrate the individual planes. When the collapse is complete, the 3 atom ω unit cell is formed; the two collapsed planes form a honeycomb lattice and the remaining plane forms the hexagonal lattice [59].*

The orientation of α″ with respect to β is,

$[001]_{\alpha''} \parallel [110]_{\beta}$

$[100]_{\alpha''} \parallel 2/3 \text{ from } [11\bar{1}]_{\beta}$

$[010]_{\alpha''} \parallel 2/3 \text{ from } [\bar{1}10]_{\beta}$

The structure of the ω phase is hexagonal (space group P6/mmm) with atomic positions (0, 0, 0), (2/3, 1/3, 1/2), and (1/3, 2/3, 1/2). This is formed by a slight distortion of the bcc phase. In Figure 1.3.7, the β→ω transformation is schematically explained by the collapse of two among three bcc planes in the [111] direction into a plane at an intermediate position, retaining the third plane as a single layer [57].

The orientation relationships, which follow directly from the atomic displacements, are:

$[0001]_{\omega} \parallel [111]_{\beta}$

$[11\bar{2}0]_{\omega} \parallel [110]_{\beta}$

And the theoretical lattice parameters are: $a_{\omega} = \sqrt{2}a_{\beta}$, $c_{\omega} = \sqrt{3}a_{\beta}/2$.

1.3.3 Young's modulus of Ti-Nb alloys

Figure 1.3.8 shows the composition dependence of Young's modulus for alloys quenched from the β region. The rigidity is highly dependent on the crystalline structure, or the predominant phase in polycrystalline compounds, revealing the phase stability as a critical parameter for the final modulus. The Young's modulus of the hexagonal phases is the highest, while the bcc exhibits the lowest E, following the relationship: $E_{\omega} > E_{\alpha'} > E_{\alpha''} > E_{\beta}$ [39]. At low Nb concentrations, the high Young's modulus is due to the stability of the hcp phase in conjunction with a small percentage of ω. The rigidity decreases upon addition of Nb reaching a local minimum at around Ti-16wt%Nb (Ti-9at%Nb) due to the progressive stabilization of α″ orthorhombic phase against the two hexagonal structures. It is known that the β-phase at high temperatures is retained by quenching at Nb content higher than 36wt% (22.5at%Nb). Subsequently a minimum in Young's modulus is observed at Ti-40wt%Nb (Ti-24.5at%Nb), which is associated with the predominance of this phase. Age-hardening by ω precipitation is expected to occur pronouncedly approximately between 20 and 35wt%Nb (11 to 22at%Nb) increasing thereby Young's modulus remarkably, favouring the emergence of a local maximum between the two minima. In compositions above 42wt%Nb

(27at%Nb) the ω phase has been experimentally observed. Taken into consideration these data some can conclude that low Young's modulus in β-Ti alloys could be achieved when the athermal ω precipitation is suppressed at specific at alloying content. In line with this idea, and in order to further decrease the Young's modulus, non-toxic ternary additions in β-type Ti-25at%Nb alloys (e.g. Sn) have shown successful results avoiding the formation of the ω phase [60, 61] nevertheless the bone –like E values are still unreachable.

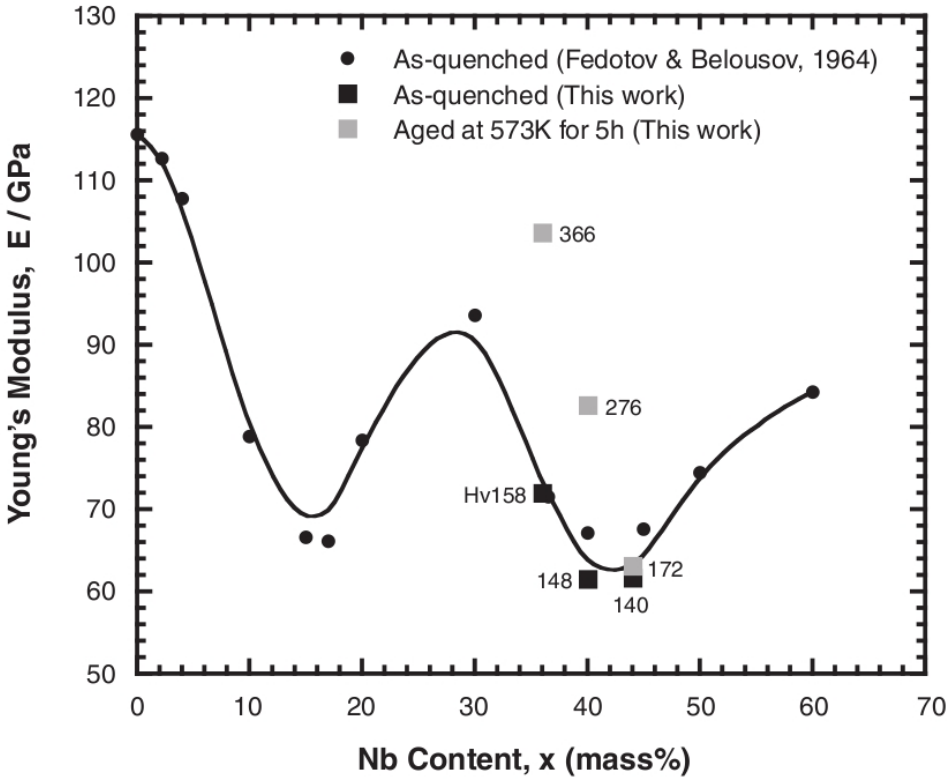

Figure 1.3.8 *Nb content of Young's modulus in quenched Ti-Nb binary alloys [39].*

1.4 References

1. Othopedic implants – A Global Market Overview. PRNewswire (2011).
2. Photos provided by Nakashima Medical Co. Ltd, Japan and Japan Medical Materials (JMM) Co. Ltd, Japan.
3. M. Geetha, A.K. Singh, R. Asokamani, A.K. Gogia. Ti based biomaterials, the ultimate choice for orthopaedic implants – A review. Progress in Materials Science 54 (2009) 397–425.
4. S. Ramakrishna, J. Mayer, E. Wintermantel E, K.W. Leong. Biomedical Applications of polymer- composite materials: A review, Composites Science and Technology, 61 (2001) 1189–224.
5. D.L. Wise DL. Biomaterials engineering and devices. Berlin: Humana Press (2000) 205–319.
6. J.B. Park, J.D. Bronzino. Biomaterials: principles and applications. Boca Raton, FL: CRC Press (2003) 1–241.
7. M. Niinomi. Metals for biomedical devices. Woodhead Publishing Limited (2010).
8. M. Niinomi. Mechanical biocompatibilities of titanium alloys for biomedical .applications. Journal of the mechanical behavior of medical materials 1 (2008) 30–42.
9. M. Long, H.J. Rack. Titanium alloys in total joint replacement--a materials science perspective. Biomaterials 19 (1998) 1621–1639.
10. D.W. Hoeppner, V. Chandrasekarn. Fretting in orthopaedic implants: a review. Wear 173 (1994) 189-97.
11. D.F. Williams. On the mechanisms of biocompatibility. Biomaterials 29 (2008) 2941–53.
12. M. Viceconti, R. Muccini, M. Bernakiewicz, M. Baleani, L. Cristofolini. Large-sliding contact elements accurately predict levels of bone– implant micromotion relevant to osseointegration. Journal of Biomechanics 33 (2000) 1611–1618.
13. A. Biesiekierski, J. Wang, M. Abdel-Hady Gepreel, C. Wen. A new look at biomedical Ti-based shape memory alloys. Acta Biomaterialia 8 (2012) 1661–1669.

14. D. Kuroda, M. Niinomi, M. Morinaga, Y. Kato, T. Yashiro. Design and mechanical properties of new beta type titanium alloy. Materials Science and Engineering A243 (1998) 244–249.
15. J. Lawrence Katz. Anisotropy of Young's modulus of bone. Nature 283 (1980) 106–107.
16. J. Black J, G.W. Hastings. Handbook of biomaterials properties. London UK: Eds. Chapman and Hall (1998).
17. D.R. Sumner, T.M. Turner, R. Igloria, R.M. Urban, J.O. Galante. Functional adaptation and ingrowth of bone vary as a function of hip implant stiffness. Journal of Biochemistry 31 (1998) 909–917.
18. M. Niinomi. Recent metallic materials for biomedical applications. Metallurgical and Materials Transactions A 32A (2001) 477–486.
19. B. Basu, D. Katti, A. Kumar. Advanced Biomaterials - Fundamentals, Processing, and Applications, Wiley (2009).
20. X. Liu, P.K. Chu, C. Ding. Surface modification of titanium, titanium alloys, and related materials for biomedical applications. Materials Science and Engineering R 47 (2004) 49–121.
21. C. Leyens, M. Peters (Eds.), Titanium and Titanium Alloys: Fundamentals and Applications, Wiley-VCH Verlag GmbH & Co. KGaA, Weinheim (2003).
22. M. Niinomi. Mechanical properties of biomedical titanium alloys. Materials Science and Engineering A243 (1998) 231–236.
23. M. Niinomi and M. Nakai Hindawi Publishing Corporation International Journal of Biomaterials (2011) Article ID 836587 doi:10.1155/2011/836587.
24. M. Niinomi, T. Hattori, T. Kasuga, H. Fukui. Titanium and Its Alloys, Encyclopedia of Biomaterials and Biomedical Engineering, Marcel Dekker (2006)
25. H. Matsumoto, S. Watanabe, S. Hanada, Strengthening of low Young's modulus beta Ti-Nb-Sn alloys by thermomechanical processing, Proceedings of the Materials and Processes for Medical Devices Conference ASM International (2006) 9–14.
26. Y.L. Hao, S.J. Li, S.Y. Sun, C.Y. Zheng, R. Yang. Elastic deformation behaviour of Ti-24Nb-4Zr-7.9Sn for biomedical applications, Acta Biomaterialia, vol. 3, no. 2 (2008) 277–286.
27. A. Migliori, H. Ledbetter, D. Thoma, T. Darling. Beryllium's monocrystal and polycrystal elastic constants. Journal of Applied Physics 95 (2004) 2436.

28. M. Friák, W.A. Counts, D. Ma, B. Sander, D. Holec, D. Raabe, J. Neugebauer. Theory-Guided Materials Design of Multi-Phase Ti-Nb Alloys with Bone-Matching Elastic Properties. Materials 5 (10) (2012) 1853-1872.
29. C. N. Reid, J. L. Routbort, R. A. Maynard. Elastic constants of Ti–40 at.% Nb at 298 °K. Journal of Applied Physics 44 (1973) 1398.
30. R. Hermann, H. Hermann, M. Calin, B. Buechner, J. Eckert. Elastic constants of single crystalline beta-Ti70Nb30, Scripta Materialia 66 (2012) 198-201.
31. M.Speirs, J.Van.Humbeeck, J.Schrootenb, J.Luytenb, J.P.Krutha. The effect of pore geometry on the mechanical properties of selectivelaser melted Ti-13Nb-13Zr scaffolds. Procedia CIRP 5 (2013) 79–82.
32. L. Machado, M. Savi. Medical applications of shape memory alloys. Brazilian Journal of Medical and Biological Research. 36(6) (2003) 683-691.
33. H.Y. Song, H.Y. Jung, S.I. Park, S.B. Kim, D.H. Lee, S.G. Kang. Covered retrievable expandable nitinol stents in patients with benign esophageal strictures: initial experience. Radiology 217 (2) (2000) 551–557.
34. J.J. Polmear. Titanium alloys in Light Alloys, Edward Arnold Publications, London, Chapter 6 (1981).
35. S. Miyazaki, H.Y. Kim, H. Hosoda. Development and characterization of Ni-free Ti-base shape memory and superelastic alloys. Materials Science and Engineering A 438– 440 (2006) 18–24.
36. H. Hosoda, Y. Fukui, T. Inamura, K. Wakashima, S. Miyazaki, K. Inoue. Mechanical properties of Ti-based shape memory alloys. Materials Science Forum 426– 432 (2003) 3121–3126.
37. H.Y. Kim, Y. Ikehara, J.I. Kim, H. Hosoda, S. Miyazaki. Martensitic transformation, shape memory effect and superelasticity of Ti–Nb binary alloys. Acta Materialia 54 (2006) 2419–2429.
38. J.Y. Rho, T. Tsui, G. Pharr. Elastic properties of human cortical and trabecular lamellar bone measured by nanoindentation. Biomaterials 18(20) (1997) 1325–30.
39. T. Ozaki, H. Matsumoto, S. Watanabe, S. Hanada. Beta Ti Alloys with Low Young's Modulus. Materials Transactions 45 (2004) 2776-2779.
40. W. Gregor, Beobachtungen und Versuche über den Menakanite, einen in Cornwall gefundenen magnetischen Sand, in Lorenz Crell's Chemische Annalen (1791) 40.
41. H.R. Ogden, in: A.H. Clifford (Ed.), Rare Metals Handbook, Rinhdd Publishing Corporation, Chapman & Hall Ltd., London (1961) 559–579.

42. E.W. Collings. The Physical Metallurgy of Titanium Alloys, ASM, Metals Park, OH (1984).
43. D.L. Moffat, U.R. Kattner. The pressure-temperature phase diagram of pure titanium. The Stable and Metastable Ti-Nb Phase Diagrams. Metallurgical Transactions A. Volume 19A (1998) 2389-2397.
44. K. Sikka, Y. K. Vohra, and R. Chidambaram. Omega phase in materials. Progress in Materials Science 27 (1982) 245.
45. D.L. Moffat, D.C. Larbalestier. The competition between martensite and omega in quenched Ti-Nb alloys. Metallurgical Transactions Volume 19, Issue 7 (1988) 1677-1686.
46. D. L. Moffat, D. C. Larbalestier. The competition between the alpha and omega phases in aged Ti-Nb alloys. Metallurgical Transactions Volume 19, Issue 7 (1988) 1687-1694.
47. J.L. Murray. Phase Diagram of Binary Titanium Alloys ASM, Materials Park, OH (I987) 188.
48. W.G. Burgers. On the process of transition of the cubic-body-centered modification into the hexagonal-close-packed modification of zirconium. Physica Volume 1, Issues 7–12 (1934) 561–586.
49. W. Petry, A. Heiming, J. Trampenau, M. Alba, C. Herzig, H. R. Schober, G. Vogl. Phonon dispersion of the bcc phase of group-IV metals. I. bcc titanium. Physical Review B 43 (1991) 10933.
50. W. Petry, A. Heiming, J. Trampenau, M. Alba, C. Herzig, H. R. Schober, G. Vogl. Phonon dispersion of the bcc phase of group-IV metals. II. bcc zirconium, a model case of dynamical precursors of martensitic transitions. Physical Review B 43 (1991) 10948.
51. W. Petry, A. Heiming, J. Trampenau, M. Alba, C. Herzig, H. R. Schober, G. Vogl. Phonon dispersion of the bcc phase of group-IV metals. III. bcc hafnium. Physical Review B 43 (1991) 10963.
52. M. Grujicic, P. Dang. Atomic-Scale Analysis of Martensitic Transformation in Titanium with Vanadium - Part I: Verification of the EAM Potential, Materials Science and. Engineering, A205 (1996) 139-152.
53. A.T. Balcerzak, S.L. Sass. The Formation of the ω phase in Ti-Nb Alloys Metallurgical and Materials Transactions B. 3(6) (1972).

54. Z. Nishiyama. Martensitic Transformation, Academic Press, New York, NY, (1978) 211-62.
55. Y.A. Bagariatskii, G.I. Nosova, T.V. Tagunova. Factors in the Formation of Metastable Phases in Titanium-Base Alloys. Soviet physics Doklady 3 (1958) 1014-1018.
56. J.P. Morniroli, M. Gantois. Investigation of the conditions for omega phase formation in Ti-Nb and Ti-Mb alloys. Memoires et etudes scientifiques de la revue de metallurgie. 70 (1973) 831-842.
57. J.M. Sanchez, D. de Fontaine. Anomalous diffusion in omega forming systems. Acta Metallurgica, Volume 26, Issue 7 (1978) 1083-1095.
58. S. Kibey, H. Sehitoglu, D.D. Johnson. Energy landscape for martensitic phase transformation in shape memory NiTi. Acta Materialia Volume 57, Issue 5 (2009) 1624-1629.
59. D. Trinkle. A theoretical study of the hcp to omega martensitic phase transition in titanium. (2003) Electronic Thesis or Dissertation. Retrieved from https://etd.ohiolink.edu/.
60. J. C. Williams, B. S. Hickman, D.H. Leslie: Metall. Trans. 2 (1971) 477–484.
61. S. Hanada, O. Izumi. Correlation of tensile properties, deformation modes, and phase stability in commercial β-phase titanium alloys. Metallurgical and Materials Transactions A, 18 (1987) 265-271.

CHAPTER 2: Theoretical background

2.1 Density Functional Theory

2.1.1 Quantum many-body problem

When considering a system of N nuclei, the problem of N+ZN electromagnetically interacting particles has to be addressed. Assuming only the pair interactions, the exact many-particle Hamiltonian is

$$H = -\frac{\hbar^2}{2}\sum_i \frac{\nabla_{R_i}^2}{M_i} - \frac{\hbar^2}{2}\sum_i \frac{\nabla_{r_i}^2}{m_e} - \frac{1}{4\pi}\left(\sum_{i,j}\frac{e^2 Z_i}{\left|\vec{R}_i - \vec{r}_j\right|} + \frac{1}{2}\sum_{\substack{i,j \\ i\neq j}}\frac{e^2}{\left|\vec{r}_i - \vec{r}_j\right|} + \frac{1}{2}\sum_{\substack{i,j \\ i\neq j}}\frac{e^2 Z_i Z_j}{\left|\vec{R}_i - \vec{R}_j\right|}\right) \quad (2.1.1)$$

where M_i is the mass of the nucleus located at the position $\vec{R}_i$, m_e is the mass of the electrons at $\vec{r}_i$ and Z_i is the atomic number of nucleus i. The first two terms are the kinetic energies for nuclei and the electrons respectively. The third, fourth and fifth terms describe the nuclei-electron, electron-electron and nuclei-nuclei Coulomb interactions. The time-independent Schrödinger equation for this system reads

$$\hat{H}\psi\left(\{\vec{R}_i\},\{\vec{r}_i\}\right) = E\psi\left(\{\vec{R}_i\},\{\vec{r}_i\}\right) \quad (2.2)$$

where Ψ is the total wave function of the system. Although all parameters in the system are known, this equation is impossible to be solved analytically and it has to be treated appropriately applying several theories and approximations to simplify the problem.

2.1.2 The Born-Oppenheimer approximation

The first step towards a reduction of its complexity is the Born-Oppenheimer approximation [1]. Since the dynamics of the electrons occurs at a time-scale that is much shorter than that of the much heavier ions, it is legitimate to assume that irrespectively of the instantaneous configuration of the ions, the electrons are at every moment in their ground state. Assuming that the ions are being "frozen" the nuclei may

keep fixed positions during the movements of the electrons and can thus be considered as positive charges independently of the electrons. With these assumptions we end up with NZ interacting negative particles, moving in an effective potential field. Accordingly, the kinetic energy of the nuclei will be zero and the Coulombic potential will be constant; thus the new Hamiltonian is

$$\widehat{H} = T_{e^-} + V_{e^- - e^-} + V_{external} \tag{2.1.3}$$

where the first term is the kinetic energy of the electron gas, the second corresponds to the potential energy due to electron-electron interactions and the third is the potential energy of the electrons in the potential of the nuclei. Thus a decoupled Hamiltonian is produced, where the contribution of the electrons and the nuclei is separated in two different Hamiltonians.

2.1.3. Density Functional Theory

The principal goal of any many-body theory is to reduce the number of parameters needed to describe the many-body system. Therefore in the quantum many-body theory within the density functional theory (DFT) treats the particle density as the fundamental variable. The goal is to derive the energy of the system in terms of the charge density. It is imperative to note that, by definition, density-functional theory is only able to predict the ground-state energy and properties; furthermore, since the ground-state energy is a function of a number of parameters of the system, DFT can be also used in order to find other ground-state properties – such as equilibrium bond-lengths – by minimizing the ground-state energy with respect to these parameters.

In principle, the theory is able to provide these quantities exactly, but in practice it is necessary to introduce some approximations. Fortunately, even the simplest conceivable approximation (the local density approximation, LDA) gives accurate results. One of the main reasons for this success is that the large kinetic energy is treated exactly, unlike in the Thomas–Fermi model [2, 3]. This accuracy, along with the fact that DFT transforms the many-body problem into an equivalent single particle problem, is the major appealing feature of the theory.

In 1964 P. Hohenberg and W. Kohn [4] showed that the exact ground-state energy of a non-degenerated many-electron system in an external potential, is a unique functional of the electron density and that this functional has its minimum at the ground-state density.

The two theorems of Hohenberg and Kohn formulated are as follows:

First theorem: *There is a one-to-one correspondence between the ground-state density* $n(\vec{r})$ *of a many-electron system (atom, molecule, solid) and the external potential* V_{ext}. *An immediate consequence is that the ground-state expectation value of any observable* Ô *is a unique functional of the exact ground-state electron density.*

$$\langle \Psi | \hat{O} | \Psi \rangle = O[n(\vec{r})] \tag{2.1.4}$$

Second theorem: *For* Ô *being the Hamiltonian* H, *the ground-state total energy functional* $H[n(\vec{r})] = E_{Vext}[n(\vec{r})]$ *is of the form*

$$E_{V_{ext}}[n(\vec{r})] = \langle \Psi | \hat{T} + \hat{V} | \Psi \rangle + \langle \Psi | \hat{V}_{ext} | \Psi \rangle =$$

$$= F_{HK}[n(\vec{r})] + \int n(\vec{r})\, V_{ext}(\vec{r}) d\vec{r} \tag{2.1.5}$$

where the Hohenberg-Kohn density functional $F_{HK}[n(\vec{r})]$ *is universal for any many-electron system.* $E_{Vext}[n(\vec{r})]$ *reaches its minimal value (equal to the ground-state total energy) for the ground-state density corresponding to* V_{ext}.

Although the proof of these theorems is out of this text's scope, and can be found in many publications among the mentioned before, it is important to remark their main consequences

i) The ground state particle density determines the full Hamiltonian, except for a constant shift of the energy. Hence all properties of the system are completely described by this ground state density.

ii) Although there is an explicit expression for the Hohenberg-Kohn functional (F_{HK}), this is unknown. Since F_{HK} does not contain information on the nuclei and their position, it is a universal functional for any many-electron system. This means that in principle an expression for $F_{HK}[n(\vec{r})]$ exists and can be used for every atom, molecule or solid which can be imagined.

iii) The ground-state density that corresponds to the external potential $V_{ext}(\vec{r})$ will be the density that minimizes $V_{ext}(n(\vec{r}))$. Of course, this can be done only if $F_{HK}[n(\vec{r})]$ is known, but once the density is known a description of the whole system can be achieved.

Although HK theorems use particle density $n(\vec{r})$ as the basic variable, it is still impossible to calculate any property of a system because $F[n(\vec{r})]$ is still unknown. The real breakthrough then came the year after, when W. Kohn and L. Sham [5, 6] proposed their ansastz in 1965 (theory that supposed to Walter Kohn the Nobel Prize in chemistry in 1998) and showed how the variational problem could be solved via an effective one-particle scheme, rendering the DFT a usable method for calculations.

Kohn and Sham (KS) formulated several suggestions in order to simplify the problem. They suggested to work with a system of non-interacting electrons, which in general, will has a wavefunction (density) different from that of the interacting ones. However in the KS approach, a fictitious non-interacting system is constructed, in such a way, that its density is the same as that of the interacting electrons. The challenge is then shifted from finding the universal HK functional to finding the fictitious system of non-interacting electrons that has the same density as the "real" one with the interacting electrons. This allows setting up more accurate calculations as the expression for the kinetic energy of non-interacting electrons.

Fifteen years later, M. Levy [7] was able to define the necessary functionals without the restrictions of the original Hohenberg–Kohn scheme. Since then until nowadays many researchers have been working on DFT, which became one of the most spread and successful methods on computational physics and materials simulations. For further information, there are many publications that describe in more details this theory [8-15].

2.1.4 Total energy in terms of density

Solving the many-particle Schrödinger equation for the ground state wavefunction and energy is an impossible task even for a system with few atoms. An alternative way to solve the Schrödinger equation is shifting the focus of the problem from $\Psi(\vec{r})$ to a fundamental observable, namely charge density $n(\vec{r})$. For a many-particle system the density, $n(\vec{r})$ is found by calculating the expectation value of the single-particle density operator for the many-body wavefunction

$$\hat{n}(\vec{r}) = \sum_{i=1,N} \delta(\vec{r} - \vec{r_i}) \tag{2.1.6}$$

$$n(\vec{r}) = \langle \Psi | \hat{n}(\vec{r}) | \Psi \rangle = N \int_V |\Psi(\vec{r}, \dots, \vec{r}_N)|^2 d\vec{r}_2 \dots d\vec{r}_N \tag{2.1.7}$$

where $\{\vec{r}_i\}$ are the variables associated with each one of the electrons. When assuming that the wavefunction is normalized to unity, integrating the electron density over all space will give us the total number of electrons in the system

$$\int_V n(\vec{r}) d\vec{r} = N \tag{2.1.8}$$

The goal in DFT is to eliminate the wavefunction by writing all terms, making up the total ground state energy of the electronic system in terms of density. This is because the desirable is to minimize the electronic energy with respect to the density in order to obtain the ground state energy and the corresponding electronic density, as commented in the previous section when the HK theorem was formulated. It is well known that once the wavefunction is obtained by solving the Hamiltonian the observable corresponding to a given operator by calculating the expectation value of that operator can be determined. This allows to separately calculate the energy terms corresponding to the potential operators given in the Hamiltonian (for the electrons).

Suppose now that the many-body Schrödinger equation and the wavefunction have be obtained. The expectation value of the nuclei-electron interaction operator is given by

$$\begin{aligned} \mathrm{E_{ne}} &= \langle \Psi(\vec{\mathrm{r}}_1, \dots, \vec{\mathrm{r}}_\mathrm{N}) \left| \hat{\mathrm{V}}_{\mathbf{ne}} \right| \Psi(\vec{\mathrm{r}}_1, \dots, \vec{\mathrm{r}}_\mathrm{N}) \rangle \\ &= -\sum_{\mathrm{i}}^{\mathrm{N_e}} \sum_{\mathrm{I}}^{\mathrm{N_n}} \int_\mathrm{V} \Psi^*(\vec{\mathrm{r}}_1, \dots, \vec{\mathrm{r}}_\mathrm{N}) \frac{\mathrm{Z_I}}{\left| \vec{\mathrm{r}}_\mathrm{i} - \vec{\mathrm{R}}_\mathrm{I} \right|} \Psi^*(\vec{\mathrm{r}}_1, \dots, \vec{\mathrm{r}}_\mathrm{N}) \mathrm{d}\vec{\mathrm{r}}_1 \dots \mathrm{d}\vec{\mathrm{r}}_\mathrm{N} \end{aligned} \tag{2.1.9}$$

after some algebraic operations, the previous expression (2.1.9) can be written as a function of $n(\vec{r})$ as it follows

$$\begin{aligned} E_{\boldsymbol{ne}} &= \langle \Psi(\vec{r}_1, \dots, \vec{r}_N) \left| \hat{V}_{\boldsymbol{ne}} \right| \Psi(\vec{r}_1, \dots, \vec{r}_N) \rangle \\ &= -\sum_{I}^{N_n} \int_V n(\vec{r}) \frac{Z_I}{\left| \vec{r}_i - \vec{R}_I \right|} d\vec{r} = \int_V n(\vec{r}) V_{\boldsymbol{ne}}(\vec{r}) d\vec{r} \end{aligned} \tag{2.1.10}$$

This simple linear functional form attained by the electron-nucleus interaction energy is in fact common to all single-body external potential terms such as an applied electric field.

After some more complicated calculations it can be proved that the equivalent derivation for the electron-electron term cannot be written in terms of the single-particle density but instead only in terms of the two-particle density:

$$E_{ee} = \frac{1}{2}\iint_V \frac{n^{(2)}(\vec{r},\vec{r}')}{|\vec{r}-\vec{r}'|}\,d\vec{r}d\vec{r}' \tag{2.1.11}$$

where $n^{(2)}$ may be interpreted as the probability that an electron exists at point $\vec{r}$ given that a second electron exists at $\vec{r}'$.

However this method does not allow the existence of such a two-particle density but instead only the one-particle density, thus another approximation has to be considered. In case that the two electrons were completely uncorrelated the two-particle density in equation 2.1.11 would just be the product of one-particle densities. This assumption will be also applied for the probabilities. Thus the $n^{(2)}$ is written in terms of this product plus a correction:

$$n^{(2)}(\vec{r},\vec{r}') = n(\vec{r})n(\vec{r}') + \Delta n^{(2)}(\vec{r},\vec{r}') \tag{2.1.12}$$

The electron-electron energy of equation 2.1.11 may then be written as

$$E_{ee} = \frac{1}{2}\iint_V d\vec{r}d\vec{r}'\frac{n(\vec{r})n(\vec{r}')}{|\vec{r}-\vec{r}'|} + \Delta E_{ee} \tag{2.1.12}$$

where the second term comes from the correction in equation 2.1.12

The kinetic energy implies an even more complicated obstacle. Since the kinetic energy operator contains a derivative term, there is no way to write it in terms of the density since it is impossible to collect the wavefunction and its conjugate as a single norm square. So in order to solve the kinetic energy, the density has to be assumed that it can be written as the sum of norm squares of a collection of single-particle orbitals, which is one of the key assumptions in DFT

$$n(\vec{r}) = \sum_{n}^{N_e} |\varphi_n(\vec{r})|^2 \tag{2.1.13}$$

These orbitals are the so called Kohn-Sham orbitals and they are initially completely unspecified on the same way as in the orbitals in the Slater determinant in the Hartree-Fock formalism. In other words, instead of the full many-particle system, a single-particle orbitals system is considered, which has the same ground state density as the real system, thus the treatment remains exactly the same.

Although the expression of the density as formulated in equation 2.1.13 suggests that the kinetic energy is written as the sum of the kinetic energies of the Kohn-Sham orbitals, this is not actually equal to the kinetic energy of the real many-particle system. Thus the kinetic energy is expressed as the single-particle kinetic energy plus a correction extra term:

$$T = -\frac{1}{2}\sum_{n}^{N_e} \int_V d\vec{r}\varphi_n^*(\vec{r})\nabla^2\varphi_n(\vec{r})d\vec{r} + \Delta T \tag{2.1.14}$$

Adding all the terms together in the same expression the total ground state energy may be written as:

$$\begin{aligned} E = -\frac{1}{2}\sum_{n}^{N_e} \int_V d\vec{r}\varphi_n^*(\vec{r})\nabla^2\varphi_n(\vec{r})d\vec{r} + \int_V n(\vec{r})V_{\boldsymbol{ne}}(\vec{r})d\vec{r} \\ + \frac{1}{2}\iint_V d\vec{r}d\vec{r}' \frac{n(\vec{r})n(\vec{r}')}{|\vec{r}-\vec{r}'|} + \Delta T + \Delta E_{\boldsymbol{ee}} \end{aligned} \tag{2.1.15}$$

The kinetic energy cannot be differentiated directly with respect to $n(\vec{r})$ but it can be equivalently minimized with respect to the orbitals. Now the only thing that remains to be done is to write ΔT and $\Delta E_{\mathbf{ee}}$ in terms of the density. It is important to note that so far, our conversion of the energy from the wavefunction description to the density representation has been exact. The accuracy of certain approximations is relied to the so called exchange-correlation energy, which is the sum of these two terms

$$E_{xc} = \Delta T + \Delta E_{\boldsymbol{ee}} \tag{2.1.16}$$

The origin of this term is the difference between a system of N interacting and non-interacting particles. More specifically, the origin of the exchange energy is the Pauli repulsion, omitted in the Hartree term, and the correlation energy corresponding to the repulsion between electrons. Thus the total energy may be written as

$$E = -\frac{1}{2}\sum_{n}^{N_e}\int_V \varphi_n^*(\vec{r})\nabla^2\varphi_n\,(\vec{r})d\vec{r} + \int_V n(\vec{r})V_{\boldsymbol{ne}}(\vec{r})d\vec{r}$$

$$+\frac{1}{2}\iint_V d\vec{r}d\vec{r}'\frac{n(\vec{r})n(\vec{r}')}{|\vec{r}-\vec{r}'|} + E_{xc} \qquad (2.1.17)$$

Eventually, the extremely complicated many-body problem that we faced before has been reduced to

i) solving an equivalent one-particle (i.e. non-interacting) system, and

ii) determining $\varepsilon_{\mathbf{xc}}(\mathrm{n})$.

thus rendering DFT calculation feasible in practice.

2.1.5 The exchange-correlation functional

Despite all the assumptions taken, the ground-state energy is still under evaluation. Since it is the interaction between the electrons which complicates the things, the exchange-correlation functional is an artificial way to gradually "turn on" the interaction between them. The exchange and correlation energies are defined as the difference between the exact total energy of a system and of the classical Hartree energy [16, 17].

2.1.6 Approximations to exchange and correlation

a) Local Density Approximation (LDA)

The first well known exchange-correlation functional, the Local Density Approximation (LDA) [4, 5] assumes a simple form in which the functional is linearly dependent on the density. This approximation considers the whole inhomogeneous and interacting system as consisting of a large number of boxes, each containing a homogeneous but interacting electron gas. Then the total exchange-correlation energy is approximated as the sum of the contributions of all such boxes:

$$E_{XC}^{LDA}[n] = \int_V n(\vec{r})\varepsilon_{XC}(n(\vec{r}))d^3r \tag{2.1.18}$$

where $\varepsilon_{XC}(n)$ is the exchange correlation energy density of an interacting homogeneous electron gas of density $n(\vec{r})$.

This approximation is valid because solids, and specially metals, can be often considered as close to the limit of homogeneous electron gas within a uniformly positive charge background. Accordingly, the exchange part is calculated exactly with the Hartree-Fock method, whereas the correlation part is calculated from Quantum Monte Carlo computations. Although LDA is a very crude approximation for systems that are not as homogeneous as an electron gas, it has proven to be a huge success even for non-metallic systems. This is in part due to the cancellation of errors, where LDA typically overestimates E_X whereas it underestimates E_C.

b) Generalized Gradient Approximation (GGA)

As previously discussed, LDA treats all systems as homogeneous; however, real systems are inhomogeneous. Attributing the limitations of the local description in the elimination of the dependence of the exchange-correlation functional on the local variations of the electron density, the General Gradient Approximation (GGA) has been introduced. In the GGA, unlike in LDA, there is an explicit dependence of the exchange-correlation functional on the gradient of the electron density

$$E_{XC}^{GGA}[n] = \int_V \varepsilon_X^{LDA}\big(n(\vec{r})\big)F_{XC}(n(\vec{r}), \nabla n(\vec{r}))d^3r \tag{2.1.19}$$

Despite the numerous GGA functionals that have been developed, there is as no consensus on the best one. For solid-state applications, the GGAs proposed by Perdew et al. [18-21] have been widely used and have proved to be quite successful in correcting some of the deficiencies of the LDA. Calculations on prediction of bond length and binding energy of molecules, crystal lattice constants, etc. especially in systems where the charge density is rapidly varying have been successfully calculated by the hand of this functional. However GGA sometimes overcorrects the LDA results in ionic crystals where the lattice constants from LDA calculations fit well with experimental data but GGA overestimate them [22, 23].

2.1.7 Augmented Plane Wave Method (APW)

For educational reason, the Augmented Plane Wave Method (APW) [24] will be described in this section as an introduction before going to its successors, the linearized augmented plane wave (LAPW) and the linearized augmented plane wave with local orbitals (APW+lo), which are the methods that will be used in our calculations.

The basic idea that leads to the APW basis consists of the division of a solid in two regions. Close to the nuclei, the electrons behave quite as if they were a free atom, and they could be described more efficiently by atomic like functions

$$\Phi_{\vec{k}_n} = \sum_{lm} A_{lm,\vec{k}_n} u_l(r, E_l) Y_{lm}(\hat{r}) \tag{2.1.20}$$

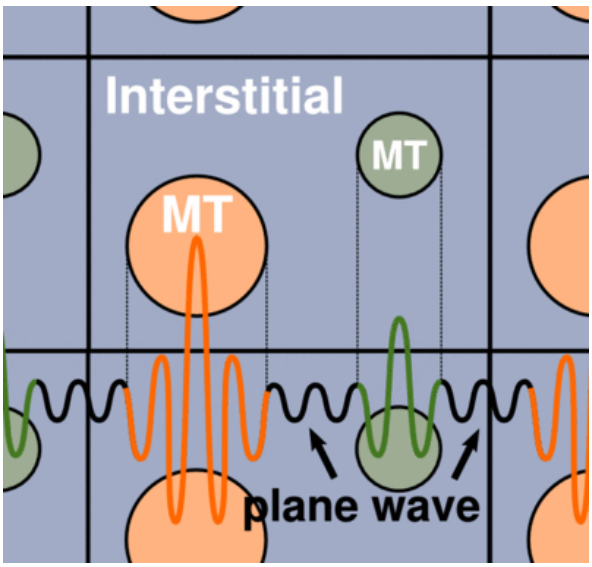

Figure 2.1.1 *Partitioning of the unit cell into atomic spheres, called "muffin tins" (MT) and interstitial region (plane waves) [25].*

It should be notted that the APW basis set is $\vec{k}$ dependent. The $u_l(r, E_l)$ correspond to the regular solutions of the radial part of the Schrödinger equation for a free atom at energy E_l, while $Y_{lm}(\hat{r})$ are spherical harmonics. The coefficients A_{lm} are functions of $\vec{k}_n$ (reciprocal lattice vectors) determined by requiring that the plane wave outside the sphere should match (in value) with the function inside the sphere over the complete surface of the sphere. The position inside the muffin tin (MT) is given with respect to the center of each sphere. On the other side, for the region far away from the nuclei, the electrons are "free", so these will be described by plane waves

$$\Phi_{\vec{k}_n} = \frac{1}{\sqrt{\Omega}} e^{i\vec{k}_n \vec{r}} \tag{2.1.21}$$

Space is therefore divided now in two regions, as is shown in Figure 2.1.1. Around each atom a sphere is drawn. Such a sphere is often called "muffin tin" sphere (MT); its radius (RMT) is a crucial parameter for DFT calculations. The second area, corresponding to the remaining space outside the spheres and which is described by a plane wave, is called the interstitial region.

2.1.8 Linearized Augmented Plane Wave Method (LAPW)

The main inconvenient with the APW method is that $u_l(r, E_l)$ has to be constructed at the initially unknown eigenvalues $E_l = \varepsilon_{\vec{k}_n}$ of the searched eigenstate. It would be helpful if someone is able to recover u_l on the fly from known quantities. That is exactly what the LAPW method enables us to do. The development and demonstration of the new equations is out of the scope of this text, this can be found in related text books [10, 26].

The linearized augmented plane wave (LAPW) method [27] is among the most accurate methods based on DFT for performing electronic structure calculations for crystals. The LAPW method is a procedure for solving the Kohn-Sham equations for the ground state density, total energy, and (Kohn-Sham) eigenvalues (energy bands) of a many-electron system by introducing a basis set adapted to the problem.

This adaptation is achieved, like in APW, by dividing the unit cell into non-overlapping atomic spheres and their interstitial region. A linear combination of radial functions times spherical harmonics $Y_{lm}(r)$ is used inside the atomic sphere

$$\Phi_{\vec{k}_n} = \sum_{lm} [A_{lm,\vec{k}_n} u_l(r, E_l) + B_{lm,\vec{k}_n} \dot{u}_l(r, E_l)] Y_{lm}(\hat{r}) \tag{2.1.22}$$

where $u_l(r, E_l)$ is the regular solution of the radial Schrödinger equation for a fixed energy E_l and the spherical part of the potential inside sphere, while $\dot{u}_l(r, E_l)$ is the energy derivative of u_l evaluated at the same energy E_l. The linear combinations of these two functions constitute the linearization of the radial function. The coefficients A_{lm} and B_{lm} are functions of $\vec{k}_n$ (reciprocal lattice vectors) determined by requiring that this basis function matches (in value and also slope) each plane wave (PW) expansion at the sphere boundaries. Finally u_l and $\dot{u}_l$ are obtained by numerical integration of the

radial Schrödinger equation on a radial mesh inside the sphere. The coefficients of the atomic-like expansion within the spheres and its energy derivative are chosen so that they match the plane-wave both in value and slope.

In the interstitial region, like in APW method, a plane wave expansion is used

$$\Phi_{\vec{k}_n} = \frac{1}{\sqrt{\Omega}} e^{i\vec{k}_n\vec{r}} \tag{2.1.23}$$

where $\vec{k}_n = \vec{k} + \vec{K}_n$; being $\vec{k}_n$ the reciprocal lattice vectors and $\vec{k}$ the wave vector inside the first Brillouin zone.

Each plane wave is augmented by an atomic-like function in every atomic sphere. The solutions to the Kohn-Sham equations are expanded in this combined basis set of LAPW's

$$\psi_{\vec{k}} = \sum_n c_n \Phi_{\vec{k}_n} \tag{2.1.24}$$

and the coefficients c_n are determined by the Rayleigh-Ritz variational principle. The convergence of this basis set is controlled by a cut-off parameter $R_{mt}K_{max} = 6 - 9$, where R_{mt} is the smallest atomic sphere radius in the unit cell and K_{max} is the magnitude of the largest k-vector in equation.

2.1.9 Linearized Augmented Plane Wave + Local Orbitals Method (LAPW+LO)

It was not explicitly stated so far which electron states are calculated with the (L)APW method. Since the low states are well bound to the nucleus (core state), it is obvious that they will not participate in chemical bonding with other atoms. For this reason core states will be contained entirely in the muffin tin sphere. States that leak out of the muffin tin sphere, and may participate in chemical bonds, are called valence states. When applying this definition, there are usually valence states with the same *l* but different *n*, called semi-core states. In order to be improved upon the linearization and to make possible a consistent treatment of semi-core and valence states in one energy window, additional (k_n independent) basis functions, called local orbitals (LO) [28] can be added. A local orbital is defined for a particular *l* and *m*, and for a particular atom *α*; while it has no effect in the interstitial region and in the muffin tin spheres of other atoms, therefore it is called local. Subsequently the formulation of the "lo" consist of a

linear combination of two radial functions at two different energies and one energy derivative (at one of these energies):

$$\Phi_{lm}^{LO} = [A_{lm}u_l\left(r, E_{1,l}^{\alpha}\right) + B_{lm}\dot{u}_l\left(r, E_{1,l}^{\alpha}\right) + C_{lm}u_l\left(r, E_{2,l}^{\alpha}\right)]Y_{lm}(\hat{r}) \quad (2.1.25)$$

The coefficients *A*, *B* and *C* are determined by the requirements that Φ^{LO} should be normalized and should have zero value and slope at the sphere boundary. Note that the addition of local orbitals increases the LAPW basis set size. Although the slightly increased computational time is a small price to be paid for a much better accuracy that local orbitals offer, and therefore they are always used.

2.1.10 The APW+lo method

Despite all the advantages within the development of LAPW method, it has been proved that the additional constraint on the PWs to match in value and slope with the solution inside the sphere is not the most efficient way to linearize Slater's APW method [29]. In addition, the problem with the APW method was the energy dependence of the basis set. The solution of the problem can be made much more efficient when one uses the standard APW basis, but with $u_l\ (r, E_l)$ at a fixed energy E_l in order to keep the linear eigenvalue problem. But we know that with fixed energies this basis set does not give a good description of the eigenfunctions.

In the APW+lo method, the basis set will be energy independent and still have the same size as in the APW method. In this sense, APW+lo combines the good features of APW and LAPW+LO, by adding a second type of function "local orbital" (equation 2.1.27) to have enough variational flexibility in the radial basis functions:

$$\Phi_{\vec{k}_n} = \sum_{lm} A_{lm,\vec{k}_n} u_l\left(r, E_{1,l}\right)Y_{lm}(\hat{r}) \quad (2.1.26)$$

$$\Phi_{lm}^{lo} = [A_{lm}u_l\left(r, E_{1,l}\right) + B_{lm}\dot{u}_l\left(r, E_{1,l}\right)]Y_{lm}(\hat{r}) \quad (2.1.27)$$

This new *lo* looks almost like the old "LAPW"-basis set, but here the A_{lm} and B_{lm} do not depend on k_n and are determined by the requirement that the *lo* is zero at the sphere boundary (not zero slope) and normalized. Hence, both the APW and the local orbital are continuous at the sphere boundary, but each of their first derivatives are discontinuous. Although is not strictly needed, the same set of energies $E_{1,l}^{\alpha}$ is used as the corresponding APW's.

This new scheme results in identical results compared to the LAPW method, allowing us to reduce "$R_{mt}K_{max}$". This leads to significantly smaller basis sets and thus the corresponding computational time is drastically reduced [30]. Within the same calculation a "LAPW and APW+lo" mixed basis can be used for different atoms and even different *l*-values of the same atom [31].

2.2 Molecular Dynamics

2.2.1 Molecular Dynamics

Molecular Dynamics (MD) is used to simulate many-body problems that are hard or impossible to be solved analytically. MD allows for the study and evaluation of physical processes in complex systems. In addition, it can verify theoretical computations and predict different phenomena [32, 33]. The simulations require initial data such as the system interatomic potential, structure, velocities, etc. MD is a deterministic method, therefore the system evolves in time. The evolution of the system is gained from its Hamiltonian (H) and the equations of motion are given by the derivatives:

$$\frac{dp_i}{dt} = -\frac{\partial H}{\partial q_i} \tag{2.2.1}$$

$$\frac{dq_i}{dt} = \frac{\partial H}{\partial p_i} \tag{2.2.2}$$

The integration of these equations over a time step gives the particles new positions and velocities $\{q_i\}$ and $\{p_i\}$ respectively. In classical systems the Hamiltonian takes the form:

$$H = K(\{\partial p_i\}) + V(\{\partial q_i\}) = \sum_i \frac{p_i^2}{2m} + V(\{\partial q_i\}) \tag{2.2.3}$$

where $K(\{\partial p_i\})$ is the kinetic energy and $V(\{\partial q_i\})$ is the potential energy which depends only on the coordinates. The (interatomic semi-empirical) potential is a crucial parameter in MD calculations, and the accuracy of the final results is highly dependent on this. The main parameters and characteristics of the potential will be discussed in the following section.

The integration method is also an important parameter that must be taken into account. The integration method is usually a finite difference scheme that evolves the particles' coordinates and velocities discretely in time. The chosen integrator needs to be accurate enough for the simulated system so that the numerical results will be close enough to the real ones and needs to be stable without losses in the total energy. In molecular dynamics, the most commonly used time integration algorithm is the Verlet's algorithm [34, 35]. The basic idea is to write two third order Taylor expansions for the positions $\vec{r}(t)$, one forward and one backward in time as follow

$$\vec{r}(t+\Delta t) = \vec{r}(t) + \vec{v}(t)\Delta t + \frac{1}{2}\vec{a}(t)\Delta t^2 + \frac{1}{6}\vec{b}(t)\Delta t^3 + \cdots \tag{2.2.4}$$

$$\vec{r}(t-\Delta t) = \vec{r}(t) - \vec{v}(t)\Delta t + \frac{1}{2}\vec{a}(t)\Delta t^2 - \frac{1}{6}\vec{b}(t)\Delta t^3 + \cdots \tag{2.2.5}$$

being $\vec{v}$ the velocities, $\vec{a}$ the accelerations, and $\vec{b}$ the third derivatives of $\vec{r}$ with respect to t. Adding the two expressions we get

$$\vec{r}(t+\Delta t) = 2\vec{r}(t) - \vec{r}(t-\Delta t) + \vec{a}(t)\Delta t^2 + \cdots \tag{2.2.6}$$

Nevertheless, although this algorithm is stable, relatively accurate and simple to implement, the velocities are not directly generated. In order to compute the kinetic energy *K*, whose evaluation is necessary to test the conservation of the energy *E*, the velocities are required. For this reason the calculation of the velocities is a crucial parameter in final accuracy of the algorithm. By using the Verlet's method, one could compute the velocities from the positions by using

$$\vec{v}(t) = \frac{\vec{r}(t+\Delta t) - \vec{r}(t-\Delta t)}{2\Delta t} \tag{2.2.7}$$

The main inconvenient of this algorithm is that, as in the previous expression (2.2.6) the error associated is of order Δt^2. To overcome this difficulty, a better implementation of the same basic algorithm is the velocity Verlet algorithm, where positions, velocities and accelerations are calculated at the same value of the time variable $t+\Delta t$. This method uses a similar approach than the basic Verlet, but incorporating explicitly the velocity as an input, instead of calculating $\vec{v}(t)$ this from the positions over time evolution. The implementation of the algorithm will be as follows:

1) The position at $(t + \Delta t)$, being Δt the time-step used in the algorithm, is calculated by

$$\vec{r}(t + \Delta t) = \vec{r}(t) + \vec{v}(t)\Delta t + \frac{1}{2}\vec{a}(t)\Delta t^2) \quad (2.2.8)$$

where $\vec{r}(t)$, $\vec{v}(t)$ and $\vec{a}(t)$ are respectively the position, the velocity and the acceleration at *t.*

2) Then the acceleration at $(t + \Delta t)$ is derived from the interatomic potential at the same time

$$\vec{a}(t + \Delta t) = -\frac{1}{m}\nabla V(\vec{r}(t + \Delta t)) \quad (2.2.9)$$

3) Finally the velocity at $(t + \Delta t)$ is calculated with the following expression

$$\vec{v}(t + \Delta t) = \vec{v}(t) + \frac{1}{2}(\vec{a}(t) + \vec{a}(t + \Delta t))\Delta t \quad (2.2.8)$$

Note that this integrator assumes that the acceleration depends only on the position, and not on the velocities.

Then another crucial parameter is the choice of the statistical ensemble of the system through which the temperature, pressure and other thermodynamic quantities are controlled. In these simulations the isothermal-isobaric (constant number of atoms, pressure and temperature - NPT) ensemble was selected and implemented with the Nose-Hoover algorithm [35, 36]. The constant parameters are achieved by introducing a time-dependent frictional term, whose time evolution is driven by the imbalance between the instantaneous kinetic energy and the average kinetic energy. This updates the position and velocity for atoms in the group each time-step, keeping a constant external temperature.

Making use of large scale MD simulations several parameters can be controlled that cannot be reproduced in DFT-LAPW simulations, like effects affected by the temperature and the performance of time dependent recreations. In addition, the system size simulated with MD is several orders of magnitude larger than in DFT, although is still limited by the CPU speed and the available memory. A good MD simulation is one

which finds the right system size that will not affect the results by itself and also the right time step that will not skip over the desired physical effect.

2.2.2 Interatomic potential

As was commented before, the interatomic potential is the most crucial parameter for the success of any MD simulation. The TB-SMA method [38] takes into account the essential band character of the metallic bond: the total energy of the system consists of a band-structure term, proportional to the effective width of the electronic band [39, 40] and a repulsive pair-potential term, which incorporates the non-band-structure parts of the total energy, including electrostatic interactions. The expression for the total energy

$$E_{total} = \sum_{i=1}^{N} \left(\sum_{j \neq i} A_{\alpha\beta}\, e^{-p_{\alpha\beta}\left(\frac{r_{ij}}{r_0^{\alpha\beta}}-1\right)} - \sqrt{\sum_{J \neq i} \xi_{\alpha\beta}^2 e^{-q_{\alpha\beta}\left(\frac{r_{ij}}{r_0^{\alpha\beta}}-1\right)}} \right) \tag{2.2.11}$$

contains a set of adjustable parameters ($A_{\alpha\beta}$, $p_{\alpha\beta}$, $q_{\alpha\beta}$, and $\xi_{\alpha\beta}$) that are usually determined by matching to experimental data of cohesive energy, lattice constant, bulk modulus, and elastic constants of the system [39 - 42], while α and β stand for the two different elements.

2.3 Theory of Elasticity

2.3.1 Hooke's law

When a force acts on a cross-sectional area, the Hooke's law is expressed as

$$\vec{\sigma} = E\, \vec{\varepsilon} \tag{2.3.1}$$

where $\vec{\sigma}$ is the stress, E is the proportionality constant (Young's modulus of elasticity) and $\vec{\varepsilon}$ is the strain.

When dealing with three dimensional mono-crystalline structures, which are highly anisotropic, the Hooke's law has to be expressed in tensorial form, as follows

$$\sigma_{ij} = C_{ijkl}\, \varepsilon_{kl} \tag{2.3.2}$$

where σ_{ij} and ε_{kl} are the strain and stress tensors and C_{ijkl} is the elastic stiffness tensor.

Inversely this expression can be written as

$$\varepsilon_{ij} = S_{ijkl}\,\sigma_{kl} \tag{2.3.3}$$

being S_{ijkl} the compliance tensor, which correspond to the inverse of the stiffness tensor ($S_{ijkl} = C_{ijkl}^{-1}$).

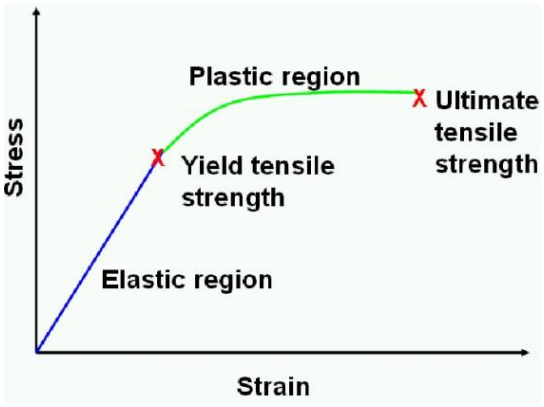

Figure 2.3.1 *Typical stress-strain curve*

2.3.2 Voigt's notation

By expressing the Hooke's law using the complete tensorial notation, writing the whole stress and strain tensor in matrix form, someone may end up with the following expression :

$$\begin{pmatrix} \varepsilon_{11} \\ \varepsilon_{22} \\ \varepsilon_{33} \\ \varepsilon_{23} \\ \varepsilon_{31} \\ \varepsilon_{12} \\ \varepsilon_{32} \\ \varepsilon_{13} \\ \varepsilon_{21} \end{pmatrix} \equiv \begin{pmatrix} s_{1111} & s_{1122} & s_{1133} & s_{1123} & s_{1131} & s_{1112} & s_{1132} & s_{1113} & s_{1121} \\ s_{2211} & s_{2222} & s_{2233} & s_{2223} & s_{2231} & s_{2212} & s_{2232} & s_{2213} & s_{2221} \\ s_{3311} & s_{3322} & s_{3333} & s_{3323} & s_{3331} & s_{3312} & s_{3332} & s_{3313} & s_{3321} \\ s_{2311} & s_{2322} & s_{2333} & s_{2323} & s_{2331} & s_{2312} & s_{2332} & s_{2313} & s_{2321} \\ s_{3111} & s_{3122} & s_{3133} & s_{3123} & s_{3131} & s_{3112} & s_{3132} & s_{3113} & s_{3121} \\ s_{1211} & s_{1222} & s_{1233} & s_{1223} & s_{1231} & s_{1212} & s_{1232} & s_{1213} & s_{1221} \\ s_{3211} & s_{3222} & s_{3233} & s_{3223} & s_{3231} & s_{3212} & s_{3232} & s_{3213} & s_{3221} \\ s_{3111} & s_{3122} & s_{3133} & s_{3123} & s_{3131} & s_{3112} & s_{3132} & s_{3113} & s_{3121} \\ s_{2111} & s_{2122} & s_{2133} & s_{2123} & s_{2131} & s_{2112} & s_{2132} & s_{2113} & s_{2121} \end{pmatrix} \begin{pmatrix} \sigma_{11} \\ \sigma_{22} \\ \sigma_{33} \\ \sigma_{23} \\ \sigma_{31} \\ \sigma_{12} \\ \sigma_{32} \\ \sigma_{13} \\ \sigma_{21} \end{pmatrix} \tag{2.3.4}$$

while taking into account the symmetry of σ, ε and S matrices, the equivalent formulation can be extracted:

$$\begin{pmatrix} \varepsilon_{11} \\ \varepsilon_{22} \\ \varepsilon_{33} \\ 2\varepsilon_{23} \\ 2\varepsilon_{31} \\ 2\varepsilon_{12} \end{pmatrix} \equiv \begin{pmatrix} s_{1111} & s_{1122} & s_{1133} & s_{1123} & 2s_{1131} & 2s_{1112} \\ s_{2211} & s_{2222} & s_{2233} & s_{2223} & 2s_{2231} & 2s_{2212} \\ s_{3311} & s_{3322} & s_{3333} & s_{3323} & 2s_{3331} & 2s_{3312} \\ 2s_{2311} & 2s_{2322} & 2s_{2333} & 4s_{2323} & 4s_{2331} & 4s_{2312} \\ 2s_{3111} & 2s_{3122} & 2s_{3133} & 4s_{3123} & 4s_{3131} & 4s_{3112} \\ 2s_{1211} & 2s_{1222} & 2s_{1233} & 4s_{1223} & 4s_{1231} & 4s_{1212} \end{pmatrix} \begin{pmatrix} \sigma_{11} \\ \sigma_{22} \\ \sigma_{33} \\ \sigma_{23} \\ \sigma_{31} \\ \sigma_{12} \end{pmatrix} \tag{2.3.5}$$

Although more compact than before this is still a tedious formulation. For this reason the Voigt's notation will be used, in which each pair of Cartesian indices *ij* are replaced by a single index α, according to:

$$\begin{matrix} ij & 11 & 22 & 33 & 23 & 13 & 12 \\ \alpha & 1 & 2 & 3 & 4 & 5 & 6 \end{matrix} \tag{2.3.6}$$

resulting in a more simplified expression

$$\begin{pmatrix} \varepsilon_1 \\ \varepsilon_2 \\ \varepsilon_3 \\ \varepsilon_4 \\ \varepsilon_5 \\ \varepsilon_6 \end{pmatrix} \equiv \begin{pmatrix} s_{11} & s_{12} & s_{13} & s_{14} & s_{15} & s_{16} \\ s_{12} & s_{22} & s_{23} & s_{24} & s_{25} & s_{26} \\ s_{13} & s_{32} & s_{33} & s_{34} & s_{35} & s_{36} \\ s_{14} & s_{24} & s_{34} & s_{44} & s_{54} & s_{64} \\ s_{15} & s_{25} & s_{35} & s_{45} & s_{55} & s_{56} \\ s_{16} & s_{26} & s_{36} & s_{46} & s_{56} & s_{66} \end{pmatrix} \begin{pmatrix} \sigma_{11} \\ \sigma_{22} \\ \sigma_{33} \\ \sigma_{23} \\ \sigma_{31} \\ \sigma_{12} \end{pmatrix} \tag{2.3.7}$$

which is much easier to handle in comparison to the expression 2.3.4.

2.3.3 Strain and Energy

In order to calculate the compliance (or the elastic stiffness) tensor by DFT calculations a well-known approach will be used that consists of the calculation of the second order elastic constants based on the computation of the total energy. This is obtained by expressing the total energy of a crystal in terms of a power series of the strain (in this case until the second order)

$$E = E(V_0) + \frac{\partial E(V_0, \varepsilon)}{\partial \varepsilon_{ij}} d\varepsilon + \frac{1}{2!} \frac{\partial^2 E(V_0, \varepsilon)}{\partial \varepsilon_{ij} \partial \varepsilon_{kl}} (d\varepsilon)^2 \tag{2.3.8}$$

where $E(V_0)$ and V_0 are the energy and volume of the reference structure, which in our case is the equilibrium one. By making use of the second order adiabatic elastic constants

$$\sigma_{ij} = \frac{1}{V_0} \left[\frac{\partial E}{\partial \varepsilon_{ij}} \right]_{\varepsilon=0} \tag{2.3.9}$$

$$C_{ijkl} = \frac{1}{V_0} \left[\frac{\partial^2 E}{\partial \varepsilon_{ij} \partial \varepsilon_{kl}} \right]_{\varepsilon=0} \tag{2.3.10}$$

and substituting 2.3.9 and 2.3.10 in 2.3.8, the following expression is obtained

$$E = E(V_0) + V_0 \sum_{i,j=1}^{3} \sigma_{ij}^{(0)} \varepsilon_{ij} + \frac{V_0}{2!} \sum_{i,j,k,l=1}^{3} C_{ijkl} \varepsilon_{ij} \varepsilon_{kl} \tag{2.3.11}$$

In order to simplify the formulation, is convenient to use the Voigt's notation as it follows

$$E(V, \varepsilon) = E_0 + V_0 \sum_{\alpha=1}^{6} \sigma_{\alpha}^{(0)} \varepsilon_{\alpha} + \frac{V_0}{2!} \sum_{\alpha,\beta=1}^{6} C_{\alpha\beta} \varepsilon_{\alpha} \varepsilon_{\beta} \tag{2.3.12}$$

It is important to note that $\sigma_{ij}^{(0)}$ is the stress of the equilibrium structure which is stress free (zero pressure) by definition. Consequently, the second term of the expression 2.3.12 (and 2.3.11), which corresponds to the first derivative of the energy with respect to the strain for the equilibrium volume vanishes. Thus the elastic stiffness tensor is expressed as a function of the strain and energy as :

$$C_{\alpha\beta} = \frac{1}{V_0} \left[\frac{\partial^2 E}{\partial \varepsilon_{\beta} \partial \varepsilon_{\beta}} \right]_{\varepsilon=0} \tag{2.3.13}$$

Making use of this expression, one just has to choose a deformation type given by the appropriate strain vector $\varepsilon = (\varepsilon_1, \varepsilon_2, \varepsilon_3, \varepsilon_4, \varepsilon_5, \varepsilon_6)$ with values taken around the origin. Then, from the total energy curves, the numerical derivatives are taken. That yields to a linear combination of the second order elastic constants. The elastic stiffness (or compliance) tensor can be simplified by applying the symmetry conditions related with the symmetry of the lattice. Due to this reason, the number of deformations which have to be applied in order to solve the system is equal to the independent C_{ij} (or S_{ij}) parameters in the matrix. Once this procedure is repeated for a properly chosen set of deformation types, the values of single second order elastic constants can be achieved solving the resulting equations. The optimum strain tensors for the different crystallographic space groups and a deeper description of this method can be found in the *ElaStic* code manuscript [47].

2.3.4 Elastic Stability

The stiffness matrix calculation is important in order to determine the response of the system under different deformations, as well as useful to predict the stability of the

different structures and stoichiometries through the elastic stability conditions [48]. The mechanical stability conditions for the cubic, hexagonal and orthorhombic lattices are given by:

Cubic lattice:

$$C_{11} > 0, C_{44} > 0, C_{11} > |C_{12}|, (C_{11} + 2C_{12}) > 0 \tag{2.3.14}$$

Hexagonal lattice:

$$C_{44} > 0, C_{11} > |C_{12}|, (C_{11} + 2C_{12})C_{33} > 2C_{13}^2 \tag{2.3.15}$$

Orthorhombic lattice:

$$\begin{gathered} C_{11} > 0, C_{22} > 0, C_{33} > 0, C_{44} > 0, C_{55} > 0, C_{66} > 0 \\ (C_{11} + C_{22} + C_{33} + 2(C_{12} + C_{13} + C_{23}) > 0 \\ (C_{11} + C_{22} - 2C_{12}) > 0 \\ (C_{11} + C_{33} - 2C_{13}) > 0 \\ (C_{22} + C_{33} - 2C_{23}) > 0 \end{gathered} \tag{2.3.16}$$

2.3.5 Voigt-Reuss-Hill approximation

Since real materials are never perfectly isotropic, the discussion of the Hooke's law for anisotropic cases is needed. Although the individual grains may exhibit the crystalline anisotropy and symmetry, when they form a polycrystalline aggregate with randomly oriented crystallites, the material is considered as microscopically isotropic. Moreover if the grains forming the poly-crystalline aggregate have preferred orientation, the material can be considered as microscopically anisotropic. Nevertheless, is important to note that grain boundaries could also influence in the mechanical characteristics of the materials.

Since DFT simulations are commonly performed on single-phase monocrystalline structures, a method to apply these calculations to more realistic polycrystalline materials comparable with experimental results (e.g. tensile or compression test) is needed. The application of an appropriate averaging procedure, can determine this properties accurately. In particular the Voigt-Reuss-Hill (VHR) approximation [49] provides a simple way to estimate the elastic constants of a textured polycrystalline matrix having grains in different orientations in terms of its crystallographic texture and elastic constants of the constituting grains. While in the Voigt's [50] approach a

uniform strain is assumed, the Reuss' [51] procedure is valid for the case of uniform stress. The resulting Voigt's and Reuss' moduli are expressed in terms of the stiffness constants *(C_{ij})* and compliances *(S_{ij})* respectively.

In the Voigt approach the bulk and shear modulus are

$$B_V = \frac{1}{9}[(C_{11} + C_{22} + C_{33}) + 2(C_{12} + C_{13} + C_{23})] \tag{2.3.17}$$

$$G_V = \frac{1}{15}[(C_{11} + C_{22} + C_{33}) - (C_{12} + C_{13} + C_{23}) + 3(C_{44} + C_{55} + C_{66})] \tag{2.3.18}$$

while the corresponding expressions for the Reuss procedure are

$$B_R = [(S_{11} + S_{22} + S_{33}) + 2(S_{12} + S_{13} + S_{23})]^{-1} \tag{2.3.19}$$

$$G_R = 15[4(S_{11} + S_{22} + S_{33}) - (S_{12} + S_{13} + S_{23}) + 3(S_{44} + S_{55} + S_{66})]^{-1} \tag{2.3.20}$$

R. Hill has shown that the Voigt and Reuss Young's moduli are the strict upper and lower bound, respectively [52, 53]. Thus, the Hill-averaged bulk and shear moduli can be determined from these upper and lower limits as

$$B_H = \frac{1}{2}(B_V + B_R) \tag{2.3.21}$$

$$G_H = \frac{1}{2}(G_V + G_R) \tag{2.3.22}$$

For all the averaged procedures presented here, the Young's modulus (E) and the Poisson's ratio (ν) can be obtained in connection with the bulk modulus, B, and the shear modulus, G, as

$$E = \frac{9BG}{3B + G} \tag{2.3.23}$$

$$\nu = \frac{3B - 2G}{2(3B + G)} \tag{2.3.24}$$

2.3.6 Young's modulus surface

With the aim of measuring the anisotropic behaviour of the elasticity modulus, the Young's modulus surface [54] may be utilized. This is given, in general form, by the following expression

$$\frac{1}{E} = l_1^4 S_{11} + l_2^4 S_{22} + l_3^4 S_{33} + 2l_1^2 l_2^2 S_{12} + 2l_1^2 l_3^2 S_{13} + 2l_2^2 l_3^2 S_{23} + l_1^2 l_2^2 S_{66} + l_1^2 l_3^2 S_{55} + l_2^2 l_3^2 S_{44} \quad (2.3.25)$$

where S_{ij} are elastic compliance constants ($S_{ij} = C_{ij}^{-1}$) and l_1, l_2 and l_3 are the direction cosines.

2.4 Computational details

2.4.1 Ab initio simulations

By using first principles (*ab initio*) calculations, ideally someone could build crystals atom by atom and describe their electronic structure in detail. Due to this reason DFT is a very powerful tool for describing the electronic configuration of metals at nanoscale, which is related to the mechanical properties. Linearized augmented plane-wave (LAPW) ab initio calculations have higher accuracy compared to other computational methods because they describe the interactions using all electrons and plane waves that may be valuable for multicomponent alloys [31]. However, this method is computationally very expensive and the calculations may be performed in small cells with limited number of atoms, whose projection in the reciprocal space are periodically reproduced by the use of k-points. Despite these features, ab initio calculations are able to describe accurately experimental measurements regarding structural, electronic and mechanical properties of materials.

In this thesis linearized augmented plane-wave method in the framework of density functional theory within the WIEN2k software were performed [31]. The exchange correlation functional within the generalized gradient approximation (GGA) in the form given by Perdew, Burke, and Ernzerhof (PBE96) was employed for the exchange correlation functional [31].

For the construction of the different cells various lattices with different symmetries and number of atoms were designed. The α′ structure (*space group $P6_3/mmc$, No. 194*) is composed by 2 basis atoms at Wyckoff positions (1/3, 2/3, 1/4) and (2/3, 1/3, 1/4); for the ω structure (*space group P6/mmm, No. 191*) the basis atoms were at (0, 0, 0), (1/3, 2/3, 1/2) and (2/3, 1/3, 1/2); the α″ structure (*space group Cmcm, No. 63*) is constructed with 4 atoms situated at (0, 0, 0), (0, y, 0), (1/2, 1/2, 0) and (0, 1/2+y, 1/2) [55]; and the β structure (space group $Im\bar{3}m$, No. 229) using one atom at the origin. It is important to comment that the α″-phase atomic positions depend on an extra degree of freedom named "y" [56] that is reported to be around 0.1 for Ti-Nb alloys [57] and whose shuffle is related with the α ↔ β phase transition [58, 59].

Several unit cells were used with respect to Nb substitutions and sampling of the Brillouin zone. In reference to Ti-Nb-Hf alloys the Nb was kept contant at 18.75at%Nb and Ti was substituted by Hf from 5.55at% up to 25at% following the experimental compositions. For the Ti-Nb-In/Sn calculations Nb concentration was kept constant at 25at%, while Ti was progressively substituted by Sn/In in concentrations starting from 2.08at% up to 25at%. For the simulation of our systems 48 basis atoms were used along with a 6x4x3 (38) k-point meshes.

As a first step, the self-consistent iteration was performed for a total energy and charge convergence of 10^{-6} Ry and 10^{-2}, respectively, keeping the atomic position constant. Afterwards, the ionic relaxation along with the electronic relaxation begins with a force convergence criterion of $5{\cdot}10^{-3}$ Ry/Bohr retaining the total energy and the charge convergence limits. Due to the large number of electrons and the atomic volume of Hf atoms, the convergence of this basis, which is controlled by a cut-off parameter, was set up to $R_{mt}K_{max} = 8$, where R_{mt} is the smallest atomic sphere radius in the unit cell and K_{max} is the magnitude of the largest k-vector in equation. For the other compositions, due to the smaller atomic radii of Ti, Nb, Sn or In compared to Hf, $R_{mt}K_{max} = 7$ was set up.

It is important to note that although the relative positions of the different type of atoms within the unit cell have a minor impact on the equilibrium lattice constants, they influence critically the system's electronic and mechanical properties. Despite the small unit cell's restrictions, several atomic rearrangements were systematically tested. Consequently, several different atomic configurations were used, in which the distributions of the Nb atoms and their short range third element's (X = In, Sn, Hf) first

neighbourhood (FN) environments were systematically tested. In particular, three main categories were considered related to the type of first neighbour atoms: a) pure Ti, b) pure Nb, and c) mixed Ti-Nb; named Ti-FN, Nb-FN and (Ti-Nb)-FN hereafter, respectively. In order to evaluate the X's energetically favoured FN, the total energy difference (ΔE) were calculated using the expression:

$$\Delta E = E_{TiNbX} - (N_{Ti}E_{Ti} + N_{Nb}E_{Nb} + N_X E_X) \quad (3.3.1)$$

where E_{TiNbX} is the total energy of the alloys for all atomic environments, N_{Ti}, $N_{Nb}$and N_X correspond to the number of Ti, Nb and In atoms in the alloy, while, E_{Ti}, E_{Nb} and E_X stand for the total energies of the corresponding pure elements in the bcc phase. From all atomic configurations, the energetically favoured FN were chosen for further studies (e.g. total energy curves, EDOSs, mechanical properties, etc.).

The band energy (E_b) is essentially able to describe the preference of a particular structure against another one taking into account the shape and the electron-filling of the corresponding EDOS. The band energy was calculated using the expression [60]

$$E_b = \int_{E_0}^{E_F} \varepsilon N(\varepsilon) d\varepsilon \quad (3.3.2)$$

where N(ε) is the occupation in the electronic density of states (EDOS), E_0 is set to -20eV where the valence and semi-core electrons mainly contribute, while E_F stands for the Fermi level.

The initial structures were treated under hydrostatic pressure and the total energy versus volume of the primitive unit cell curve was fitted by the Birch-Murnaghan equation of state determining the optimum lattice parameters and the bulk moduli. In addition the full second order elastic stiffness tensors were calculated from total-energy calculations within the framework of the *ElaStic* package [47]. The deformations performed were as many as the independent parameters presented in the stiffness tensor. The bulk, shear and Young's moduli as well as the Poisson's ratio were averaged by the Voigt-Reuss-Hill approximation [52] in order to simulate more accurately the behavior of a polycrystalline system. For the applied deformations, several strains were applied (from 1% to 15%) within the different intervals (with 11 or 23 deformations). The smallest strain value was used to determine the equilibrium lattice constant more accurately, which is especially useful in the orthorhombic case that has three independent lattice constants. Then the larger strains, which can be fitted more accurately [47], were

considered in order to obtain the Energy vs. Strain curves. Finally the fit interval and the order of the polynomial were determined following the convergence criteria suggested for the ElaStic package authors [47]. It is important to notice that in general terms, when a large deformation (10-15%) is performed, the calculated C_{ij} values will be more accurate, due to the better convergence in the analysis performed by the ElaStiC code. Nevertheless when we deal with metastable phases, very large deformations along certain directions may lead to abrupt changes in the energy caused perhaps by phase transitions. On the other hand, when the deformation is too small, the accuracy of the code is not enough to distinguish the energy difference between two points. Therefore, tuning the interval and the range of the polynomium used for the fitting is one of the most challenging parameters to determine and is crucial for the final accuracy of the calculations.

The powder diffraction pattern simulations were performed within the VESTA software [61] taking as input the energetically favoured unit cell calculated by the WIEN2k code.

2.4.2 Molecular Dynamics simulations

For the last part of this work, the size of the simulations was scaled-up from DFT to classical molecular dynamics, allowing us to create larger systems and to perform time and temperature dependent simulations. To this aim, a semi-empirical interatomic potential in analogy to the tight binding scheme in the second moment approximation was developed in our group by Assoc. Prof. D.G. Papageorgiou. The aforementioned potential allows us to describe the interactions of Ti-Zr-Hf metals and their alloys. The adjustment of the necessary parameters has been done considering the basic energetic, structural and elastic experimental data for the elemental cases, while the heats of mixing in the dilute limit have been taken into account in the cases of the cross interactions, as we can see in Table 2.4.1. The fitting parameters of the potentials are listed in Table 2.4.1 and described in more detail in the theoretical background section (chapter 2.2).

The potential models were subsequently validated by a series of Molecular Dynamics simulations from which several thermodynamic quantities, as well as the lattice and elastic constants, were compared with available experimental data in the pure elements, while solubility and heat of mixing at various concentrations were used in the alloy cases [42-46]. In addition the radial distribution function of the pure elements, selective

binary systems (Ti-20at%Zr, Ti-20at%Hf and Zr-20at%Hf) and some ternaries have been plotted (Figure 2.4.1).

		Fitting values at Zero temperature										MD at 300K results			
		a (Å)	c/a	Ω (Å^3)	E_C (ev)	C11 (ev/Å^3)	C12 (ev/Å^3)	C13 (ev/Å^3)	C33 (ev/Å^3)	C55 (ev/Å^3)	E_{VF} (ev)	*a (Å)*	*E_C (ev)*	*T_m (K)*	*ΔH_m (kJ/mol)*
Hf	Calc:	3,163	1,628	22,319	-6,437	1,238	0,498	0,406	1,350	0,277	2,630	3,175	-6,398	2636	26,05
	Exp:	3,195	1,581	22,321	-6,440	1,187	0,465	0,409	1,276	0,374	2,150	3,195	-6,440	2506	25,50
	%	*0,98*	*2,98*	*0,01*	*0,04*	*4,30*	*7,10*	*0,73*	*5,80*	*25,94*	*22,33*	*0,61*	*0,66*	*5,19*	*2,16*
Ti	Calc:	2,924	1,630	17,637	-4,847	1,189	0,528	0,438	1,288	0,239	1,770	2,937	-4,807	1970	19,30
	Exp:	2,951	1,586	17,638	-4,850	1,099	0,542	0,426	1,189	0,317	1,550	2,951	-4,850	1941	18,70
	%	*0,92*	*2,79*	*0,01*	*0,06*	*8,19*	*2,58*	*2,82*	*8,33*	*24,61*	*14,19*	*0,47*	*0,89*	*1,49*	*3,21*
Zr	Calc:	3,207	1,629	23,269	-6,247	0,990	0,471	0,397	1,069	0,185	2,070	3,218	-6,207	2240	21,23
	Exp:	3,231	1,593	23,272	-6,250	0,970	0,419	0,403	1,077	0,227	1,750	3,231	-6,250	2128	21,00
	%	*0,75*	*2,28*	*0,01*	*0,05*	*2,06*	*12,41*	*1,49*	*0,74*	*18,50*	*18,29*	*0,41*	*0,68*	*5,26*	*1,10*

Table 2.4.1 *Adjustment of the parameters for the construction of the potential and comparison of several simulations (300K) with available experimental data in the pure elements.*

As expected, lower and wider peaks correspond to polycrystalline cases, in contrast with the shaper peaks which stand for the monocrystalline systems. The values of the lattice constants a and c are respectively given by the first and the third peaks. In addition, it is interesting to mention that all the RDFs exhibit identical features with the only difference of a shift, which depends on the lattice parameters. This fact suggests the same crystallographic structure (hcp) for all these alloys. Summarizing, the obtained models can describe satisfactorily the solid solution cases of Ti-based binary and ternary alloys.

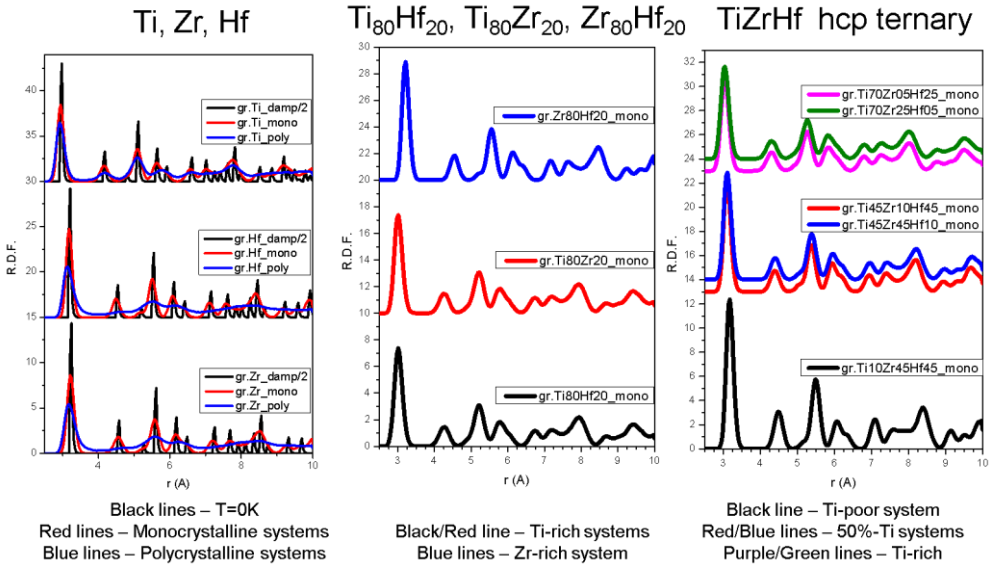

Figure 2.4.1 *Radial distribution function for the elements and its alloy.*

Using this interatomic potential, classical molecular dynamics simulations were performed by means of the LAMMPS code [62]. The structural and mechanical properties of the pure Ti, Zr and Hf metals as well as their Ti-based binaries (Ti-25at%Zr, Ti-25at%Hf) and ternaries (Ti-12.5at%Zr-12.5at%Hf) were studied. The radial distribution function was evaluated for a crystal with up to 104832 atoms that was melted to 3000K and quenched at 0.1K/ps, 1K/ps and 10K/ps to room temperature. Finally, tensile deformation was applied with a strain rate of of $10^{-5}s^{-1}$ while imposing a Poisson's ratio of 0.3.

2.5 References

1. M. Born, J.R. Oppenheimer. Zur Quantentheorie der Molekeln (On the Quantum Theory of Molecules). Annalen der Physik 389, 20 (1927) 457-484.
2. H.L. Thomas. The calculation of atomic fields. Proceedings of the Cambridge Philosophical Society 23 (5) (1927) 542- 548.
3. E. Fermi. Un Metodo Statistico per la Determinazione di alcune Prioprieta dell'Atomo. Rendiconti della Accademia Nazionale dei Lincei 6 (1927) 602-607.
4. P. Hohenberg, W. Kohn. Inhomogeneous Electron Gas. Physical Review, 136:B864, (1964).
5. W. Kohn, L.J. Sham. Self-Consistent Equations Including Exchange and Correlation. Effects. Physical Review 140 (1965) A1133.
6. L.J. Sham, W. Kohn. One-Particle Properties of an Inhomogeneous Interacting Electron Gas. Physical Review 145 (1966) 561.
7. M. Levy. Universal variational functionals of electron densities, first-order density matrices, and natural spin-orbitals and solution of the v-representability problem. Proceeding of the National Academy of Sciences of the United States of America 12 76 (1979) 6062 – 6065.
8. A. Blom. Density-functional theory for beginners. Solid State Theory, Department of Physics, Lund University, Sweden.
9. N. Argaman, G. Makovar. Density Functional Theory an introduction Xiv:physics/9806013v2 (physics.ed-ph) 19 Jul 1999.
10. S. Cottenier. Density Functional Theory and the Family of (L)APW-methods: a step-by-step introduction. (2013) ISBN 978-90-807215-1-7.
11. J. Hafner. Atomic-Scale Computational Materials Sciences. Acta materialia 48 (2000) 71-92.
12. G. Bozzolo, R.D. Noebe, P.B. Abel. Applied Computational Materials Modeling: Theory, Simulation and Experiment. (2007) Springer Science & Business Media.
13. E. Kaxiras. Atomic and Electronic Structure of Solids. Cambridge University Press (2003).
14. D.S Sholl. J.A. Steckel. Density Functional Theory. A Practical Introduction. Editorial Wiley (2009).
15. E. Canadell, M.L. Doublet, C. Iung. Orbital Approach to the Electronic Structure of Solids. Oxford University Press (2012).

16. D.R. Hartree, Proceedings of the Cambridge Philosophical Society 24 (1928) 89.
17. V. Fock. "Näherungsmethode zur Losung des quanten-mechanischen Mehrkörperprobleme" Zeitschrift für Physik 61 (1930) 126.
18. J.P. Perdew, W. Yue. Accurate and simple density functional for the electronic exchange energy: Generalized gradient approximation. Physical Review B 33 (1986) 8800.
19. A.D. Becke. Density-functional exchange-energy approximation with correct asymptotic behavior. Physical Review A 38 (1988) 3098.
20. J.P. Perdew, J.A. Chevary, S.H. Vosko, K.A. Jackson, M.R. Pederson, C. Fiolhais. Atoms, molecules, solids, and surfaces: Applications of the generalized gradient approximation for exchange and correlation. Physical Review B 46 (1992) 6671.
21. J. P. Perdew, K. Burke, M. Ernzerhof. Generalized Gradient Approximation Made Simple. Physical Review Letters 77 (1996) 3865.
22. G. Kresse, J. Furthmueller, J. Hafner. Physical Review B50 (1994) 13181.
23. K. Seifert, J. Hafner, J. Furthmüller, G. Kresse. The influence of generalized gradient corrections to the LDA on predictions of structural phase stability: The Peierls distortion in As and Sb. Journal of Physics: Condensed Matter 7 (1995) 3683.
24. J. C. Slater. Wave Functions in a Periodic Potential. Physical Review 51 (1937) 846.
25. J.K. Dewhurst, S. Sharma. Development of the Elk LAPW Code, Max Planck Institute of Microstructure Physics. Theory Department.
26. D. Singh. Plane waves, pseudopotentials and the LAPW method, Kluwer Academic (1994).
27. O.K.Andersen, Linear methods in band theory. Physical Review B 12 (1975) 3060.
28. Planewaves, pseudopotentials and the LAPW-method, D. Singh, Kluwer Academic publishing (1994) ISBN 0-7923-9421-7.
29. E. Sjostedt, L. Nordstrom and D.J. Singh, Solid State Communications 114 (2000) 15.
30. K.Schwarz, P.Blaha, G.K.H.Madsen, Comp.Phys.Commun.147 (2002) 71-76.
31. P. Blaha, K. Schwarz, G.K.H. Madsen, D. Kvasnicka, J. Luitz. WIEN2k. An Augmented Plane Wave Plus Local Orbitals Program for Calculating Crystal Properties, Vienna University of Technology, Vienna, Austria (2001).

32. D.C. Rapaport. The Art of Molecular Dynamics Simulation Second Edition. Cambridge Univeristy Press (2004).
33. F. Ercolessi. A molecular dynamics primer. Interntional School for Advanced Studies (SISSA-ISAS) Trieste, Italy.
34. L Verlet. Computer "Experiments" on Classical Fluids. I. Thermodynamical properties of Lennard-Jones Molecules. Physical Review 159 (1967) 98.
35. L Verlet. Computer "Experiments" on Classical Fluids. II. Equilibrium Correlation Functions. Physical Review 165 (1968) 201.
36. S. Nose. A Molecular Dynamics Method for Simulations in the Canonical Ensemble. Molecular Physics 52 (1984) 255-268.
37. W.G. Hoover. Canonical Dynamics: Equilibrium Phase-Space Distributions, Physical Review A 31 (1985) 1695-1697.
38. G.C. Kallinteris, N.I. Papanicolaou, G.A. Evangelakis, D. A. Papaconstantopoulos. Thigh-Binding Interatomic Potentials Based. Physical Review B 55 4 (1997) 2150-2156.
39. D. Tomanek, A.A. Aligia, C.A. Balseiro. Physical Review B 32 (1985) 5051.
40. W. Zhong, Y.S. Li, D. Tomanek. Physical Review B 44 (1991) 13 053.
41. V. Rosato, M. Guillope, B. Legrand. Philosophical Magazine A 59 (1989) 321.
42. C. Kittel. Introduction to Solid State Physics, Willey (1976).
43. C.S. Barrett, T.B. Massalsky. Structure of Metals, Pergamon (1980).
44. G. Simmon, H. Wang. Single Crystal Elastic Constants and Calculated Aggregate Properties, MIT Press (1971).
45. G.M. Hood. Journal of Nuclear Materials 139 (1986) 17912-16.
46. V.O. Shestopal. Soviet Physics Solid State 7 (1966) 2798.
47. R. Golesorkhtabar, P. Pavone, J. Spitaler, P. Puschnig, C. Draxl. ElaStic: A tool for calculating second-order elastic constants from first principles. Computer Physics Communications 184 (2013) 1861–1873.
48. J.F. Nye. Physical Properties of Crystals. Oxford University Press, Oxford (1985)
49. C.S. Man, M. Huang. A Simple Explicit Formula for the Voigt-Reuss-Hill Average of Elastic Polycrystals with Arbitrary Crystal and Texture Symmetries. Journal of Elasticity 105 (2011) 29–48.
50. W. Voigt. Lehrbuch der Kristallphysik. B.G. Teubner (1928).
51. A. Reuss, Z. Angew. Berchung der Fließgrenze von Mischkristallen auf Grund der Plastizitätsbedingung für Einkristalle, Mathematik und Mechanik 9 (1929) 49–58.

52. R. Hill. The elastic behavior of a crystalline aggregate. Proceedings of the Physical Society A 65 (1952) 349.
53. R. Hill. Elastic properties of reinforced solids: some theoretical principles. Journal of the Mechanics and Physics of Solids 11 (1963) 357.
54. G. Duffing, Die Schmiermittelreibung bei Gleitflächen von endlicher Breite; in Handbuch der Physikalischen und Technischen Mechanik, Bd. 3. Ed. F. Auerbach, W. Hort, Barth, Leipzig (1931) page 249.
55. C. Li, H. Luo, Q. Hu, R. Yang, F. Yin, O. Umezawa, L. Vitos. Lattice parameters and relative stability of α″ phase in binary titanium alloys by first-principles calculations. Solid State Communications 159 (2013) 70-75.
56. Y.A. Bagariatskii, G.I. Nosova, T.V. Tagunova. Factors in the Formation of Metastable Phases in Titanium-Base Alloys. Soviet physics Doklady 3 (1958) 1014-1018.
57. T. Ahmed, H.J. Rack. Martensitic transformations in Ti-(16-26 at %) Nb alloys. Journal of Materials Science 31 (1996) 4267-4276.
58. A. Pathak, S. Banumathy, R. Sankarasubramanian, A.K. Singh. Orthorhombic martensitic phase in Ti–Nb alloys: A first principles study. Computational Materials Science 83 (2014) 222–228.
59. J.P. Morniroli, M. Gantois. Investigation of the conditions for omega phase formation in Ti-Nb and Ti-Mb alloys. Memoires et etudes scientifiques de la revue de metallurgie. 70 (1973) 831-842.
60. P. Soederlind, O. Eriksson, J.M. Wills, A.M. Boring. Theory of elastic constants of cubic transition metals and alloys. Physical Review B 48 (1993) 5844.
61. K. Momma and F. Izumi, VESTA 3 for three-dimensional visualization of crystal, volumetric and morphology data, Journal of Applied Crystallography 44 (2011) 1272-1276.
62. S. Plimpton. Fast Parallel Algorithms for Short-Range Molecular Dynamics. Journal of Computational Physics 117 (1995) 1-19.

CHAPTER 3: Results

3.1 Ti-Nb alloys

3.1.1 Introduction

As has been commented in the introduction chapter, upon the Ti-Nb alloy's preparation several phases (including α′, β, α″ and ω) may coexist depending on the Nb concentration [1-3]. Therefore, although Nb is a β-stabilizer element, the β-phase becomes stable mainly for Nb compositions above 23at%. This behavior is directly related with the instability of pure Ti β-phase at ambient conditions, that is correlated to its elastic instability due to the negative values of the tetragonal shear constant C'. For cubic *d* transition metals and alloys, the C' is associated with the energy difference between the fcc and bcc, while the stability of these close-packed structures (fcc, hcp, bcc) is linked to the electronic band filling and the *d*-electrons' number and shape in the electronic density of states [4]. These methodologies tried to correlate the electronic properties of the Ti-based alloy with the experimentally observed low Young's modulus and shape memory characteristic and were used as guides for the design of new alloys. Nevertheless, although the last years the attention was indeed concentrated on the Ti-Nb alloys, most of the studies, especially the theoretical ones were focused mainly on the β-phase and on specific Nb concentrations. Therefore investigations concerning the interpretation on the existence of the experimentally observed phases and their influence on the alloy's properties to our knowledge are lacking.

In this chapter, we report a systematic study of Ti-Nb alloys with increasing Nb concentration by first principles calculations and a comparison with experimental data. The α′, β, α″ and ω phases were studied by ab initio calculations trying to understand the relationship between the structural, electronic and mechanical properties of Ti-Nb alloys while in the next chapters the β-Ti based ternary alloys properties (Ti-Nb-X, X=Sn, In, Hf (wt%)) will be presented.

3.1.2 Results and discussion

a) Structural properties

The main scope of this chapter is to identify the links between the mechanical properties, the structure and the chemistry of pure Ti and its Ti-Nb alloys for various crystalline phases: e.g. α′, ω, β and orthorhombic α″. It came out that the predominant crystalline structure depends on the Nb concentration while all phases contribute in the experimentally observed mechanical properties (e.g. Young's moduli).

In Figure 3.1.1 the Total Energy for the α′, ω, β and orthorhombic α″ phases are represented as a function of the unit cell volume. In this figure, the hexagonal phases are found to be more stable for the smallest Nb concentrations while for the highest Nb compositions the β-phase becomes the energetically fauvored. In particular, the total energy (figure 3.1.1) shows, as expected, the α′ and ω phases of Ti-($0 \leq x \leq 6.25$)at%Nb as energetically favoured structures compared to α" and β phases. The bcc structure is especially unfavoured for low Nb compositions, Ti-($0 \leq x \leq 12.5$)at%Nb, with energy differences above 0.1 eV compared to the α' phase. In particular, for Ti-($0 \leq x \leq 6.25$)at%Nb the α' and ω phases are the energetically favoured structures, while at the low Nb compositions Ti-($0 \leq x \leq 12.5$)at%Nb the β-phase is really unfavoured, with energy differences above 0.1 eV compared to the α′-phase, Figure 3.1.1. On the contrary, for higher Nb content Ti-($x \geq 18.75$)at%Nb, the β-phase becomes energetically favoured.

It should be noted that although the ab initio data reveal the orthorhombic α"-phase unfavoured for all Ti-xNb compositions, the total energy difference at Nb12.5at% is small compared to the α' and β phases, denoting that these structures could in fact coexist with others, in line with the experimental observations.

The metastable character of the orthorhombic α"-phase that is related with the martensitic formation could be associated with the experimental rapidly quenched casting methods, as arc melting or mould suction, which allows the formation of several Ti-Nb phases [3, 5, 6]. An increasing trend of the volume's unit cell as a function of the Nb addition is observed in the Total Energy vs. Volume curves (Figure 3.1.1), in agreement with the experimental results [7].

Furthermore, the system's lattice constants along with the bulk moduli were calculated by fitting the Total Energy vs. Volume curves to the Birch Murnaghan equation of state. Figure 3.1.2 depicts the α′, ω, α″ and β lattice constants of Ti-Nb binary alloys.

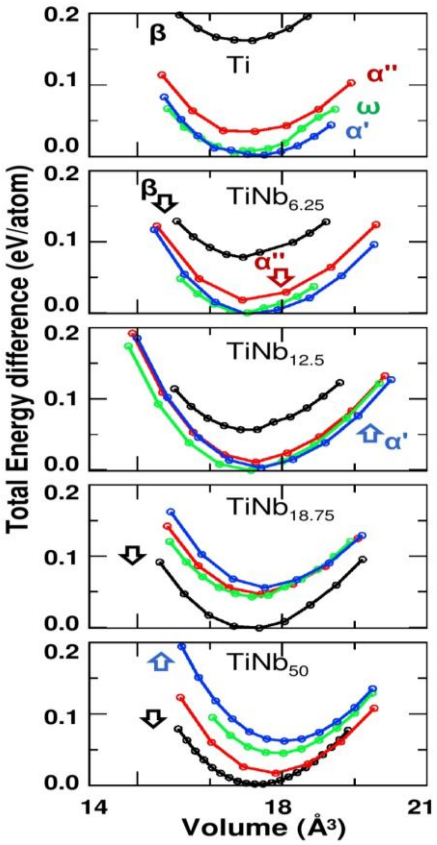

Figure 3.1.1 *Total energy versus volume of the experimentally observed Ti-xNb (x = 0, 6.25, 12.5, 18,75 and 25 (at%)) crystalline structures. Where the α′, ω, α″ and β phases are respectively represented by blue, green, red and black traces.*

In the α′ and ω phases, due to the hexagonal symmetry pattern of the lattice, two different lattice constants *a* and *c* (or *a* and *c/a*) have to be optimized. In Figure 3.1.2(a) the α′-phase lattice constants follow a linear trend: *a* slightly decreases upon addition of Nb, while *c* increases with a much more pronounced slope compared to *a*. On the contrary, in ω Ti-Nb (Figure 3.1.2(b)), the lattice constants evolution follow the opposite trend, *a* increases more than 0.1 Å compared to the pure Ti and Ti-33.33atNb, while *c* slightly decreases with the addition of Nb. It should be noted, that the presence of ω-Ti-Nb grains that were experimentally observed in the binary system is very crucial, because although only small volume percentages have been experimentally measured, they play an important role since they increase the Young´s modulus [8]. Therefore, a theoretical study of the structural (including also mechanical) properties of the ω-phase is crucial for the physical insight of Ti-Nb alloys. It is worth to be noted that although the hexagonal phases of pure Ti have been largely studied, to our knowledge, studies regarding the structural properties of α′ and ω-phase Ti-Nb alloys

are rather scarce. Experimentally, the presence of ω grains is especially difficult to be detected in Ti-Nb alloys due to their small volume percentage. Moreover ω precipitates could appear after mechanical deformation, which is critical for orthopaedical applications. This lack renders the theoretical and experimental results of this chapter regarding the Ti-Nb ω-phase very interesting and innovative. The present DFT calculations are in good agreement with available experimental results for pure Ti and Ti-Nb carried out by our colleagues at IFW Dresden.

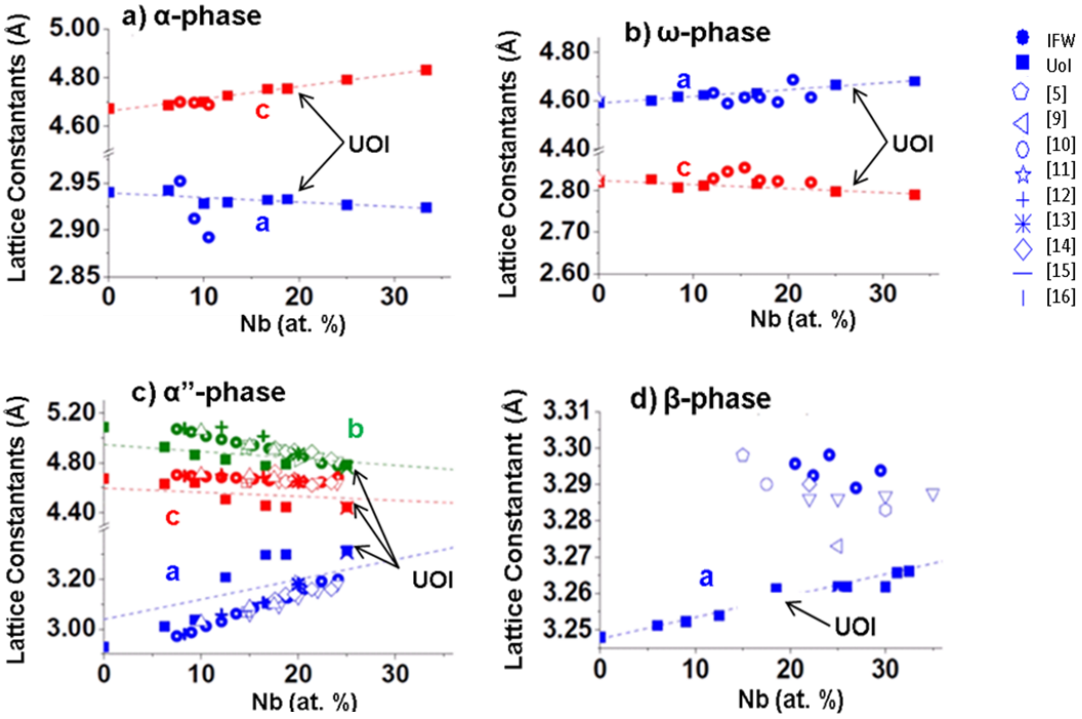

Figure 3.1.2 *Lattice constants of* **a)** *α,* **b)** *ω,* **c)** *α″ and* **d)** *β phases for the binary Ti-Nb alloys. The solid squares stand for this work, the bold circles for IFW measurements while the other data are referred to previous works [5, 9-16] for comparison.*

Turning to the α″-phase, due to its orthorhombic symmetry three independent lattice parameters along with the *y*-parameter (defined in 3.1.2) can be distinguished, which makes in total four degrees of freedom to be evaluated. In order to simplify the calculations, *y* was kept constant ($y = 0.2$) and the lattice constants (*a*, *b* and *c*) were calculated after several strains of the unit cell along the three axes. The *a* lattice constant is found the only lattice constant which increases as a result of the progressive addition of Nb while the *b* and *c* lattice constants are progressively reduced (Figure 3.1.2(c)). Moreover in the orthorhombic case, a relatively large difference between the ab initio calculations and the experimental values compared to the α′, ω or β structures can be

observed. These calculations can be assumed to exhibit the largest error due to the presence of the four degrees of freedom along with the constant *y* value ($y = 0.2$) during the lattice parameters optimization. Nevertheless although the absolute values may differ from the experimental lattice constant, they follow the experimental trend upon Nb substitution.

Due to its cubic β-phase's symmetry, the lattice constant is obtained from the optimum volume under hydrostatic pressure. In particular Figure 3.1.2(d) shows the linear increase of the lattice constant as a result of Niobium addition.

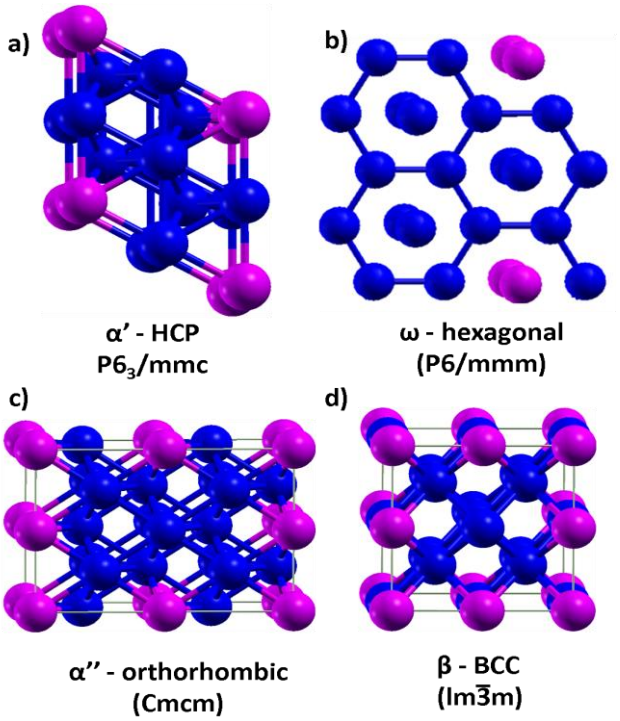

Figure 3.1.3 *Energetically favoured atomic conformation of a) α'-Ti-12.50at%Nb, b) ω-Ti-16.67at%Nb, c) α"-Ti-18.75at%Nb and d) β-Ti-18.75at%Nb. The Ti and Nb atoms are represented by blue and magenta spheres.*

Although our ab initio calculations underestimate the experimental results, probably due to:

i) the approximations in Density Functional Theory

ii) small mono-crystalline unit cells

iii) the absence of temperature and pressure

they follow the same trend in comparison with the available XRD measurements.

Summarizing, the equilibrium Ti-Nb supercell volume increases upon Nb substitution for all phases in line with the available XRD patterns [7].

The atomic rearrangement inside the supercell is a critical parameter in the present ab initio calculations. Due to this reason, for the design of the unit cell, several atomic configurations have been considered revealing the Nb preference for a pure Ti first neighbourhood (FN). Consequently, the Ti-FN was chosen for further study, trying to simulate a solid solution in which the Nb atoms had a majority of Ti nearest neighbour atoms. In Figure 3.1.3 the energetically favoured unit cell for selective stoichiometries are shown as examples for the different phases. It is clearly visible that the preferred atomic conformation is the one where the Nb atoms are homogeneously distributed in the crystalline matrix. Interestingly, in both α″ and ω-phases the Nb atoms are found to lay in the (0001) plane, which in the ω case stands for the non-dense plane.

b) Electronic properties

For the energetically favoured atomic conformation and the optimum equilibrium lattice, the Electronic Density of States' (EDOS) have been calculated for several Ti-Nb stoichiometries. The analysis of the EDOS aims in understanding [4]

i) the electronic origin of the phase transitions,

ii) the coexistence of several phases,

iii) the influence of different Nb compositions

In particular the role of Nb additions in the stabilization or destabilization of the different structures and consequently in the mechanical properties may be determined from its electronic structure by analyzing the shape and the filling of the EDOS at the Fermi level [4]. Figure 3.1.4 – 3.1.8 and Figures SM 1-4 depict respectively the total and partials EDOS of α′, ω, α″ and β phases of Ti-xNb for different Nb additions. It is clearly visible that the α′ and ω phases present a deep local EDOS minimum located at the Fermi level (E_F) and a high occupation of states bellow E_F denoting the stability of these lattices at low Nb concentrations, Ti-($x \leq 9.375$)at%Nb. Nb *d*-electrons are mainly responsible for the states between -3.5eV and $E_{F,}$ while their hybridizations with the Ti *d*-electrons along with a small contribution from the *p*-electrons, approximately 10 times smaller compared to the *d*-contribution, enhance the electron occupation at the Fermi level. This phenomenon induces the destabilization of both hexagonal lattices

subsequent to the substitutional addition of Nb. The Ti-Nb hybridizations are also visible in the *p*-electrons, where a broad band appears from approximately -6eV to E_F. These p-electron hybridizations introduce a high peak around -0.5eV that decreases progressively upon Nb addition. This effect, which is more pronounced in the pure ω-Ti EDOS, is depleted up to 50% in the Nb rich compositions (Ti-50at%Nb). This is due to the smaller contribution of *p*-Ti electrons compared to *p*-Nb at 0.5eV. In analogy with the *p*-electrons, the *s* contribution is smaller than the *d*-electrons occupation in the total EDOS. The *s*-states are located below E_F occupying energies between -1eV and -6eV, with a maximum occupation between 0.15 and 0.20states/eV/atom at around -3eV.

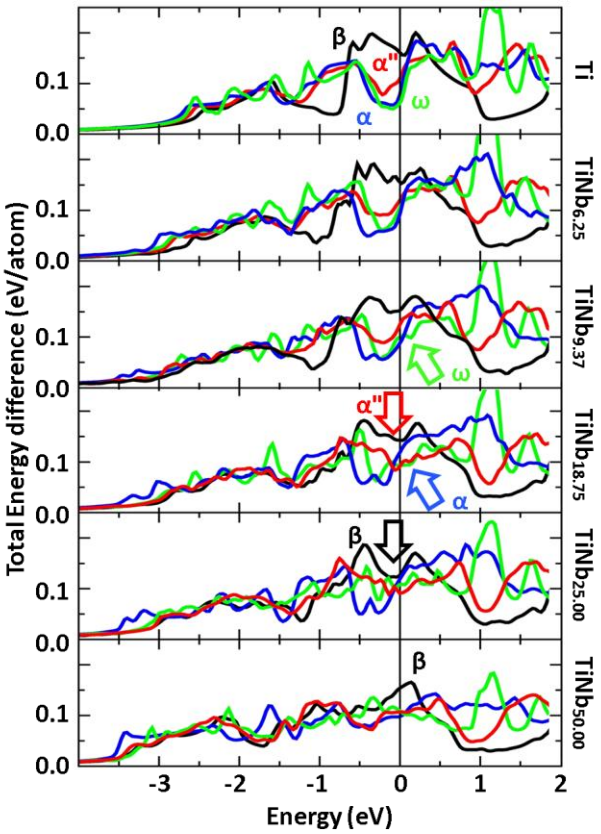

Figure 3.1.4 *Electronic density of states of the experimentally observed Ti-xNb (x = 0, 6.25, 9.37, 18.75, 25 and 50 (at%)) crystalline structures. Where the α′, ω, α″ and β phases are respectively represented by blue, green, red and black traces.*

Concerning the martensite orthorhombic α″-phase, we observe that small Nb additions (≤18.75at%Nb) reduce the occupation at E_F rendering the α″ structure more stable than the α′ or ω phases, Figure 3.1.4. In particular, for the lowest Nb contents the α′ and ω phases present a minimum at the Fermi level that is filled up upon Nb addition, denoting the stability of these phases. On the other hand, although pure α″-Ti has a

minimum located bellow E_F, denoting instability, for Ti-(12.5 ≤ x ≤ 25)at%Nb this minimum is shifted exactly at E_F revealing stability of the orthorhombic lattice, in agreement with previous experimental studies [7, 17].

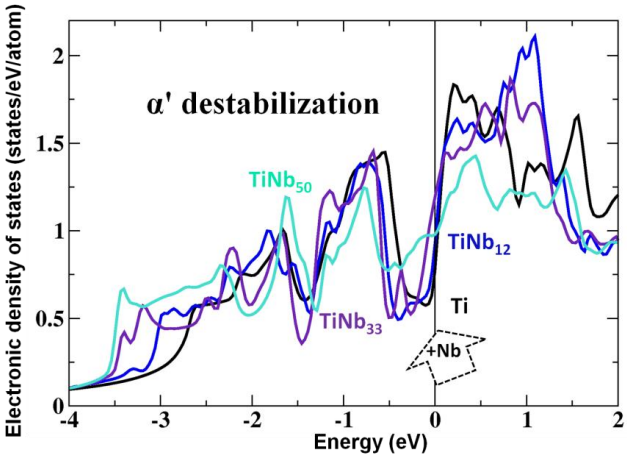

Figure 3.1.5 *Electronic density of states of α′-phase pure Ti (black), Ti-12.5at%Nb (blue), Ti-33.33at%Nb (purple) and Ti-50at%Nb (turquoise).*

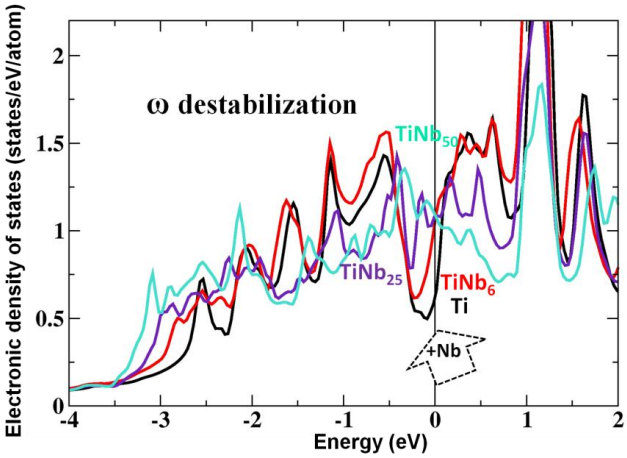

Figure 3.1.6 *Electronic density of states of ω-phase pure Ti (black), Ti-6.25at%Nb (red), Ti-25at%Nb (purple) and Ti-50at%Nb (turquoise).*

For Nb additions higher than 25at%, the occupation at the Fermi level is equivalent for the orthorhombic as well as the bcc phase. It is worth to be noted that the presence of local minima (pseudogap) at E_F, presented for the α″-Ti-(12.5 ≤ x ≤ 25)at%Nb compositions, may reveal the metastable character of the orthorhombic phase and could be related with its coexistence with other phases, in line with experimental observations [7]. The α″ metastable features could be explained by the absence of a wide and deep

minimum at $E_{F,}$ similar to the ones of the α′ and ω-phase of Ti-($0 \leq x \leq 6.25$)at%Nb or β-Ti-25at%Nb.

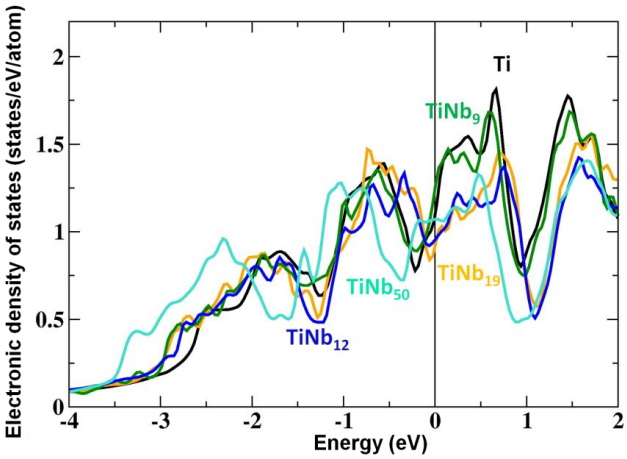

Figure 3.1.7 *Electronic density of states of α″-phase pure Ti (black), Ti-9.375at%Nb (green), Ti-12.5at%Nb (blue), Ti-18.75at%Nb (orange) and Ti-50at%Nb (turquoise).*

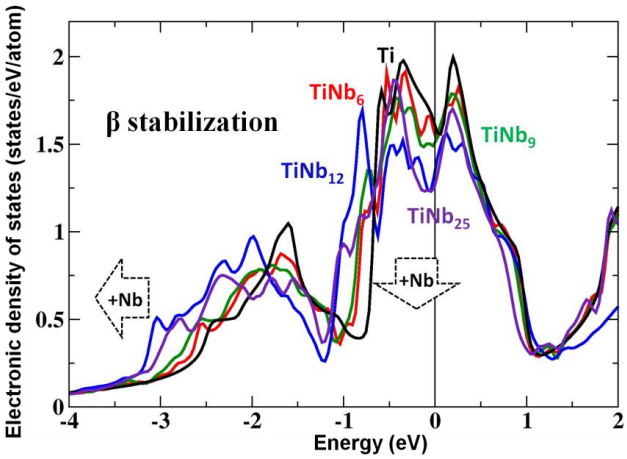

Figure 3.1.8 *Electronic density of states of β-phase pure Ti (black), Ti-6.25at%Nb (red), Ti-9.375at%Nb (green), Ti-12.5at%Nb (blue) and Ti-25at%Nb (purple).*

Regarding the α″ partial EDOS contributions (Figure SM 3), the Nb *d*-electrons are distributed between -3.5eV and E_F exhibiting two main peaks at -1eV and -3eV. The Nb-Ti hybridizations are mainly responsible for the states at the Fermi level and subsequently for the stabilization or destabilization of the orthorhombic structure. In addition the partial *p*-electrons, although with smaller contributions compared with the *d*-electrons, are also responsible for the minimum at $E_{F.}$ In line with the other cases, the *p*-electrons are located within a broad band located approximately between -6eV and E_F, with a higher occupation between --1eV and E_F. Finally the *s* electrons occupy the

states between -1eV and -6eV, with a maximum occupation of around 0.15-0.20states/eV/atom at -3eV, exhibiting an analogous distribution with the one described previously.

The stabilization of the bcc lattice is crucial since the cubic structures are expected to have lower Young's moduli than the hexagonal structures. The physical insight of the emergence of the β-phase upon Nb substitution and the interrelated destabilization of α′ and ω can be explained by the new electronic configuration caused by the Nb-Ti hybridizations. In particular we found that Nb enrichment results in the enhancement of the number of β-Ti-Nb *d*-electrons, while the main Nb contribution in the EDOS is located around -1eV (Figure SM 4). These *d*-electrons are located between -3.5eV and E_F and are mainly responsible for the pseudogap at the Fermi level. Interestingly, and in contrast to the α and ω cases, this Nb-Ti hybridization is responsible for the depletion of the occupied electronic states at the Fermi level, which characterize the β-phase of Ti, thus leading in a stable bcc structure.

Moreover, the presence of a local maximum around -2eV in the *d*-electrons partial EDOS for low Nb compositions is shifted to lower energy states as a result of Nb addition. The combination of the electronic states: a) depletion at E_F and b) shift towards lower energies, denote the stability of the bcc phase upon Nb substitution. The depletion of the states at the Fermi level can be also observed in the *p*-electrons EDOS. The main Nb *p*-electron (*p*-Nb) EDOS peak, located on E_F is depleted from 0.20 states/eV/atom of pure Ti to 0.15eV/states/atom for the highest Nb compositions. In addition the Ti p-electron (*p*-Ti) and *p*-Nb peaks around -0.75eV or at the E_F (p-Ti EDOS) are shifted to lower energy values upon Nb addition. In line with the previously described cases, the *s*-electrons occupy a broad band between -1eV and -6eV with a maximum occupation of 0.20states/eV/atom. This peak is initially located around -2eV for pure β-Ti and at -4eV for α-Ti, while in the alloy case is situated around –3eV.

Summarizing, from the study of the electronic properties we are able to conclude that the minimum electron occupancy at the Fermi level (E_F) indicates the stability of α′ and ω structures at low Nb concentrations, Ti-($x \leq 9.375$)at%Nb. Regarding the martensite orthorhombic α″-phase, small Nb additions ($\leq$ 18.75at%Nb) render this structure more stable than a' or ω, whereas for Nb compositions above 25at%Nb the orthorhombic structure is unfavoured compared to β.

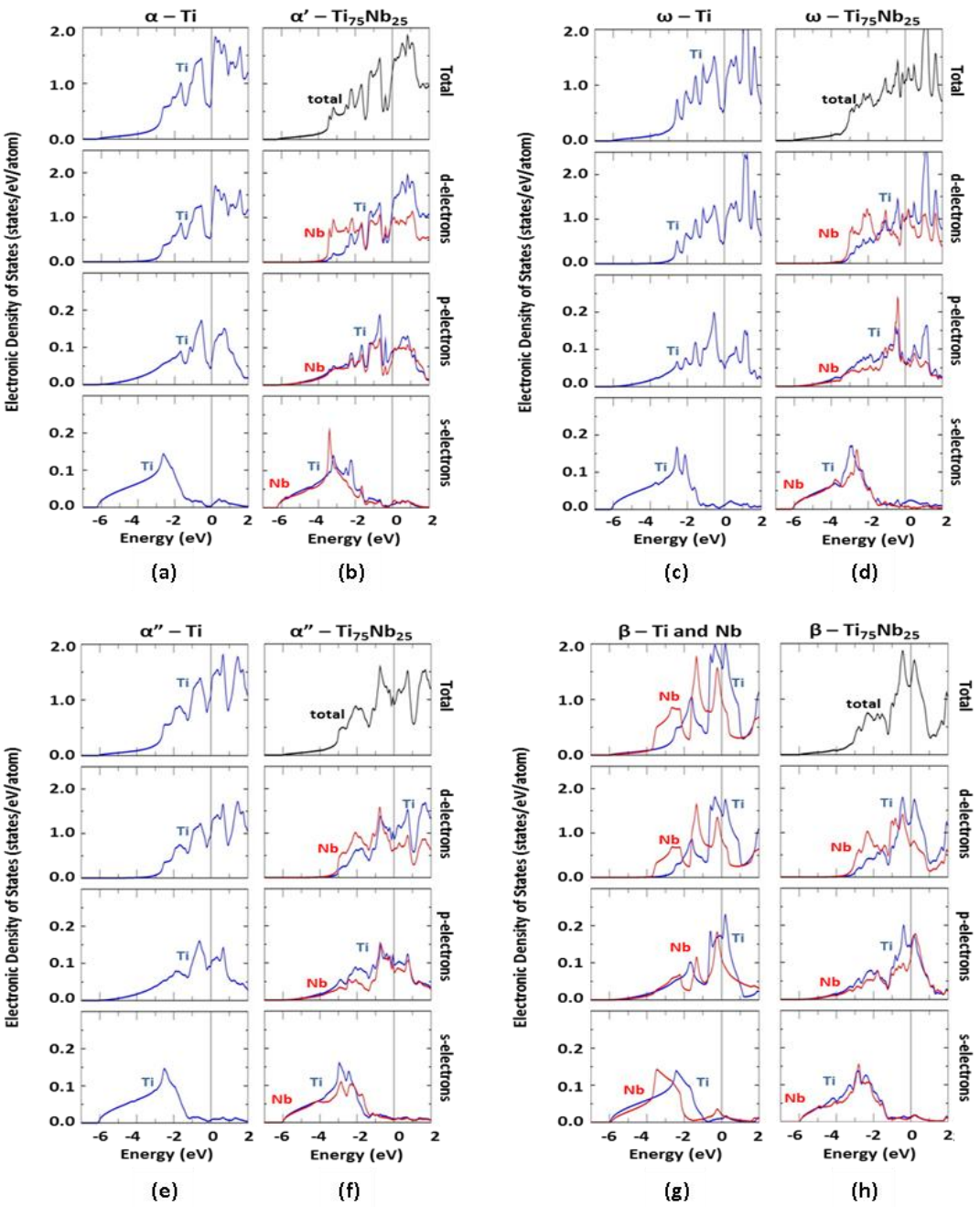

Figure 3.1.8 *Partial electronic density of states of:* **a)** *α-Ti,* **b)** *α'-Ti-25at%Nb,* **c)** *ω-Ti,* **d)** *ω-Ti-25at%Nb,* **e)** *α"-Ti,* **f)** *α"-Ti-25at%Nb,* **g)** *β-Ti , β-Nb and* **h)** *β-Ti-25at%Nb; for the total, d, p and s contributions (first up to fourth row, respectively).Blue lines stand for the Ti-partial contribution, red for the Nb-partial contribution and black for the total average.*

For the highest Nb contents, the Nb-Ti hybridizations are responsible for the depletion of the occupied electronic states at the Fermi level of the binary system, which characterize the pure β-Ti, thus leading in a stable bcc structure. The partial EDOSs show an analogous behavior for the α′, ω, α″ and β phases and demonstrate that the

maximum contribution is due to the *d*-electrons. These *d*-electrons are located between -3.5eV and E_F and are mainly responsible for the states at the Fermi level. In addition the *p*-electrons are also responsible for the broad band that goes from -6 eV to E_F although with significantly smaller contributions in the total EDOS compared to the *d*-electrons. The *s* electrons occupy the states between -1eV and -6eV, with a maximum occupation of 0.20states/eV/atom at -3eV. Concluding, these quantum mechanical calculations predict the presence and coexistence of α′, ω, α″ and β Ti-Nb phases as a function of Nb substitution due to the shape and the filling of the EDOS, especially at E_F. The results of this work are in line with available experimental data [3, 6, 7, 17].

c) Mechanical properties

i) Elastic stiffness and mechanical stability

The ab initio WIEN2k total energy results and the ElaStic package [18] were used in order to calculate the elastic constants of the Ti-Nb alloys. In Figure 3.1.9 the values of the elastic stiffness matrix (C_{ij}) and selective mechanical stability conditions for α′, ω, α″ and β phases (equations 3.1.1-3) are presented [19]. The behavior of the mechanical stability conditions upon Nb substitution, crucial for the stabilization or destabilization of these phases, is denoted by arrows. In particular the linear decreasing of C_{44} (light-blue turned squares) for the two hexagonal phases (α′ and ω) suggests the progressive destabilization of these structures as a result of the Nb addition (positive C_{44} values denote phase stability). In addition, although the condition $C_{11} > |C_{12}|$ is fulfilled for the Nb $\leq$ 33.33at% cases, this difference presents a downward trend upon Nb substitution suggesting progressive destabilization of the hexagonal lattices. In particular, C_{12} elastic constant (represented by red circles) increases whereas C_{11} (represented by black squares) remains constant for the α′-phase and decreases linearly for the ω-phase. The ω-phase C_{11} and C_{12} equivalent values for Ti-33.33at%Nb, (Figure 3.1.9(b)), suggest the initiation of its mechanical destabilization. Concerning the orthorhombic case, all the mechanical stability conditions (equations 3.1.3) are fulfilled. In order to conclude about the stability of this structure other criteria had to be consedered, like the total energy preference and the electronic density of states behavior. In any case, the C_{ij} values can be used for the calculation of the mechanical properties (e.g. Young's moduli) by means of the VRH average method. On the other hand, for the β phase the negative value of C' ($C' = (C_{11} - C_{12})/2$), where C_{11} and C_{12}

are respectively represented by black squares and red circles, becomes positive around 10at%Nb denoting the initiation of β-phase stabilization. Furthermore the C_{11} increasing trend that converges around 15at%Nb shows the mechanical stability of the bcc phase for Nb-rich compositions. The positive value of C_{44} is related with the mechanical stability, being approximately 40GPa for all compositions. The results concerning the mechanical stability of α′, β and ω phases are in agreement with previous studies [20-24], while to our knowledge studies concerning the elastic stiffness matrix for the orthorhombic α″-phase do not exist. It has to be noted that the results concerning the orthorhombic phase are very interesting because they could be related with its superelasticity and shape memory features [5, 25, 26].

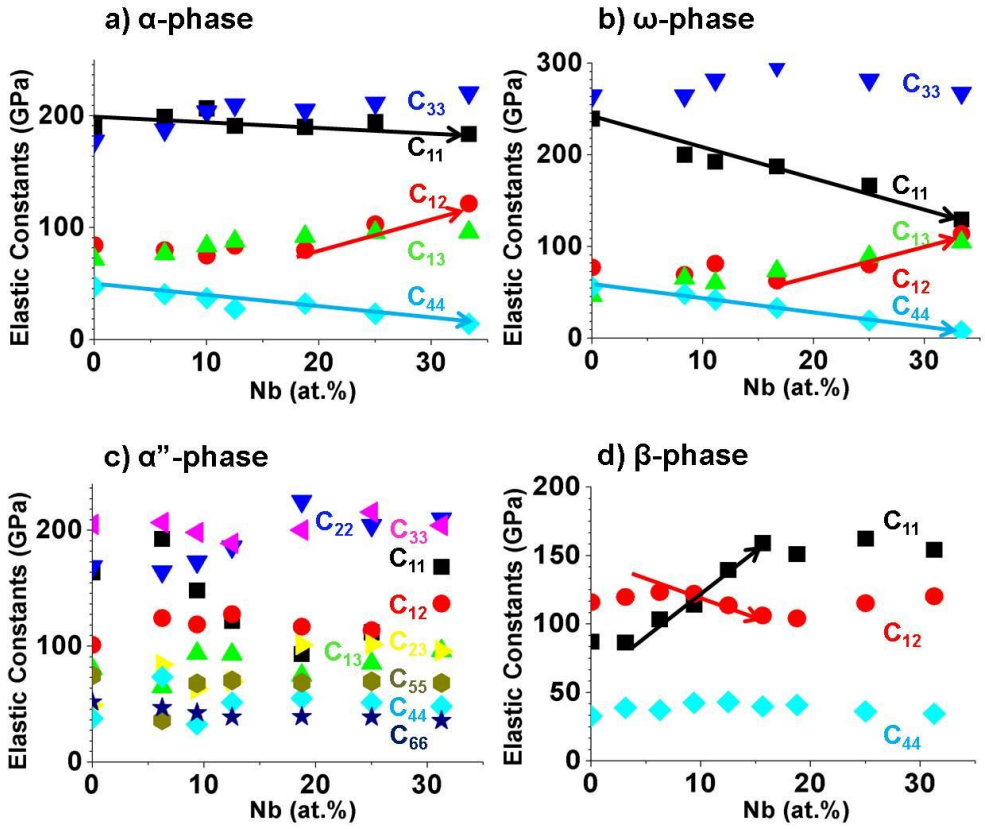

Figure 3.1.9 *Elastic stiffness tensor and Mechanical stability conditions of the Ti-Nb* **a)** *α,* **b)** *ω,* **c)** *α″ and* **d)** *β phases versus Nb composition. The blue arrows denote the destabilization of α and ω phases while the cross between C_{11} and C_{12} shows the initiation of the β-phase stabilization.*

Concluding, the analysis of the mechanical stability conditions shows the destabilization of the α′ and ω structures upon Nb addition, while in Nb-rich compositions (> 15at%Nb) the β-phase stabilization features emerge. The elastic stiffness matrix's

components can be used in order to predict the system's mechanical properties like bulk, shear and Young's moduli as well as the Poisson's ratio, for every phase and for the different Nb stoichiometries.

ii) Elastic properties

The elastic properties of the Ti-xNb ($x \leq 35$at%) alloys were systematically studied for every single-crystal structure using the corresponding elastic stiffness matrix (C_{ij}). Figure 3.1.10 illustrates the evolution of the bulk modulus (B), shear modulus (G), Poisson's ratio (ν) and Young's modulus (E); as a function of Nb concentration. These parameters were carefully averaged by means of the Voigt-Reuss-Hill (VRH) approximation [27, 28]. More details and basic notions about the VRH average are explained in the section 2.3.4 of the theoretical background chapter.

The hexagonal α′ and ω structures reveal similar behavior concerning K, G, ν and E upon Nb addition. In particular, the E and G values decrease almost linearly with the presence of Nb. The Young's moduli values are $134\text{GPa} < E_{\alpha'} < 75\text{GPa}$ for the α′-phase and $185\text{GPa} < E_{\omega} < 39\text{GPa}$ for the ω-phase, indicating a drastically reduction of the Young's moduli for rich-Nb compositions. Nevertheless, these low Young's moduli values could be related with the destabilization of the α′ and ω phases at the high Nb substitutions that are difficult to be found in the experimentally casted alloys. In addition, the shear moduli values are within $51\text{GPa} < G_{\alpha'} < 26\text{GPa}$ and $75\text{GPa} < G_{\omega} < 13\text{GPa}$ for the α′ and ω phases respectively, for Nb substitutions between 0 and 35at%. Generally, the Young's and shear moduli vary linearly between the lowest (pure Ti) and the highest (Ti-33.33at%Nb) Nb composition. On the other hand, the B and ν values follow the opposite trend. The bulk modulus increases from 112GPa to 135GPa for the α′-phase whereas in the ω-phase B maintains a constant average value around 120GPa. Referring to the ω-phase Poisson's ratio a pronounced increase is visible upon Nb addition being almost 0.4 for Ti-33.33at%Nb compared to 0.2 for the pure β-Ti.

Regarding the α″-phase, most of the calculated values remain constant upon Nb addition. This behavior is more visible for Ti-xNb ($9\text{at\%Nb} < x < 25\text{at\%Nb}$) with average values of $B_{\alpha''} = 116\text{GPa}$, $G_{\alpha''} = 39\text{GPa}$, $\nu_{\alpha''} = 0.34$ and $E_{\alpha''} = 105\text{GPa}$. On the other hand, the higher E values where found for the lower Nb compositions, (less than 9at%), while a non-linear behavior was predicted for the bulk moduli. These results

could be related with the instability of the orthorhombic structure for the lowest Nb concentrations.

For Ti-xNb (x > 15at%Nb) the β-phase is expected to exist since all the mechanical stability conditions are fulfilled whereas the G, ν and E reveal almost constant values for Nb compositions above 12.5at%. In particular, for Ti-xNb (Nb > 12.5at%) the values for the Poisson's ratio ν varies from 0.37 up to 0.41, G from 30GPa to 34GPa, while the E data oscillate between 84GPa and 93GPa; values that can be considered as constants. For Ti-xNb (x < 12.5at%) compositions, the calculated ν exhibit extremely high values (above 0.5), while E and G acquire very low moduli, which may acquire even negative values, revealing the instability of the β-phase Ti-xNb (x < 12.5at%). Meanwhile the β-phase bulk modulus shows a linear increasing trend from 106GPa for pure Ti up to 132GPa for the Ti-31.25at%Nb. Ductility is another important parameter to take into account in the design of materials for biomedical applications. In brittle materials failure will occur within or just after the elastic region of the stress-strain curve, whereas ductile materials exhibit a long phase of plastic deformation prior to ultimate failure. In biomedical implants the toughness and ductility may prevent the catastrophic failure as a result of accidental overload or localized strain. The ductility can be estimated from the ratio between the bulk (B) and the shear (G) moduli. Materials with low B/G ratio are considered as fragile materials, while for high B/G the materials are ductile [29]. For all cases, we found that B increases (Figure 3.1.10(a)) upon Nb addition. Similarly, the G values (Figure 3.1.10(b)) remains almost constant or increase, depending on the structure and the stoichiometry. Therefore we could suggest according to the Pugh's law that the addition of Nb to Ti results in an overall ductility improvement.

In Figure 3.1.10(d) the β-phase presents the lowest Young's moduli for the Ti-(x ≤ 32.5at%)Nb alloys, compared to α′, ω and α″ phases while the ω-phase exhibits the highest Young's moduli values for the low Nb compositions, in agreement with the previous studies. The Young's moduli of the β–phase (E_β) presents a constant modulus (approximately 87GPa) for Nb compositions higher than 12.5at% while for the lower Nb concentrations, i.e. β-Ti-9.375at%Nb, the modulus is closer to the desired E_{bone} ~ 30GPa revealing the importance of β–Ti(x ≤ 12at%)Nb stabilization. Similar behavior is found for the $E_{\alpha''}$, although with higher values compared to the β-phase. The VRH Young's modulus of α′ and ω achieve maximum values for the pure Ti cases, while they

decrease linearly upon Nb additions. Interestingly, although the E_{ω} decreases down to 39GPa for Ti-33.33at%Nb, this phase is unfavoured for the Nb-rich compositions.

Finally, the Young's moduli reveals higher values for the hexagonal phases than orthorhombic and β phases ($E_{\omega} > E_{\alpha'} > E_{\alpha''} > E_{\beta}$), while a weighted average on these structures as a function of Nb is expected to lead to the experimentally observed w-shaped curve [8]. Therefore, the absolute and the relative Young's moduli values between the experimentally observed structures could be a crucial parameter for the final Young's modulus of the polycrystalline compound. It is important to note that although the grain boundaries may influence the experimental Young's moduli, they cannot be considered within the DFT approach.

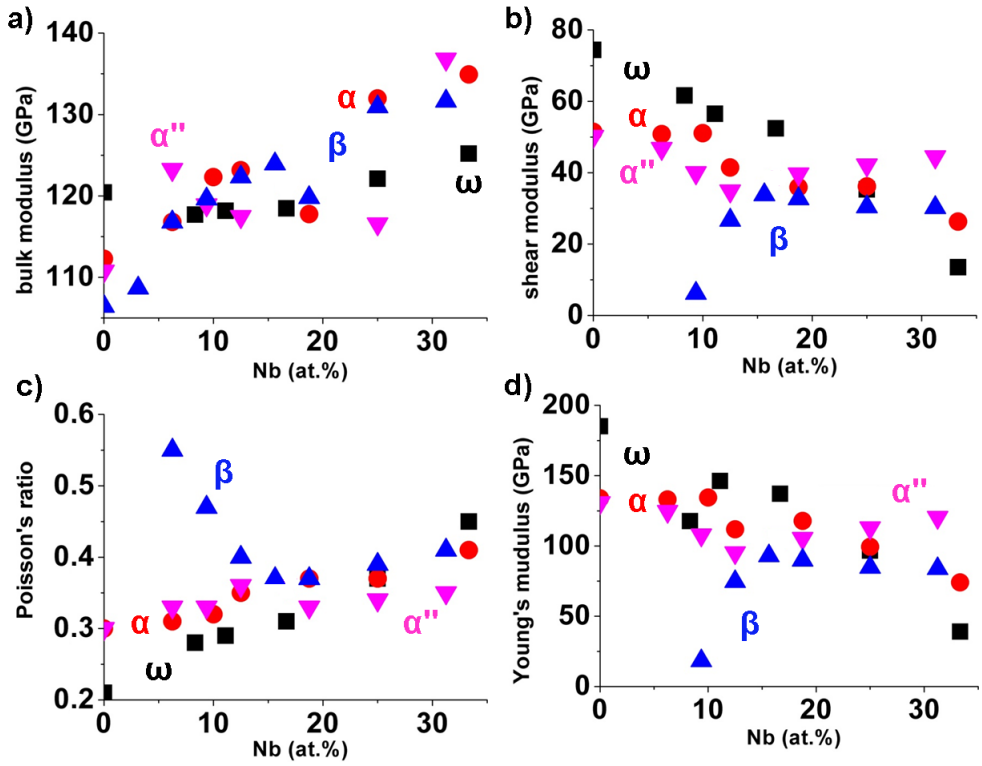

Figure 3.1.10 *Ab initio calculations for single-crystal Ti-xNb of* **a)** *bulk modulus,* **b)** *shear modulus,* **c)** *Poisson's ratio and* **d)** *Young's modulus; averaged by the Voigt-Reuss-Hill approximation. The α', ω, α" and β phases are respectively represented by blue, green, red and black marks.*

As already mentioned, the achievement of low Young's moduli values is closely related with the stabilization of the β-phase. Indeed this phase exhibits the higher stability and the mechanical isotropy keeping the lowest Young's moduli for Nb compositions above

15at% compared to the other phases. Although with a slight overestimation, these calculations are in agreement with available experimental and theoretical studies.

Finally the Young's modulus surface [30] was calculated allowing a very illustrative way to describe the elasticity as a function of the crystallographic direction. In particular, the directional elasticity modulus is defined in spherical coordinates: the directions are given by the angles θ ($0 \leq \theta \leq 2\pi$) and φ ($-\pi/2 \leq \varphi \leq \pi/2$), while the Young's moduli is represented by the modulus r, which is the distance from the origin to the surface. The graphical representation of the directional Young's moduli for selective stoichiometries and for all phases is given in Figures 3.1.11-12. For the two hexagonal phases, the Young's modulus surface depicts an anisotropic teetotum-like shape. For the α′-phase, E reveals values up to 140GPa and 150GPa respectively for the pure Ti and Ti-25at%Nb concentrations, as depicted in the Figure 3.1.11, along the [001] direction ([0001] direction for the hexagonal Miller indices). The ω-phase exhibits a rather higher maximum modulus compared to the E calculated by the VRH approximation (polycrystalline form). In the single-crystal case the ω structure shows the greatest anisotropy, compared even to α′, with the highest $E_{[001]}$ value, always above 200GPa for Ti-xNb ($x \leq 33.33$at%) and reaching up to 250GPa for pure Ti. These results are in line with previous experimental studies on single-crystal ω-Ti [24]. Another striking result is the exceptionally local low moduli values observed in certain directions. Clear examples of this phenomenon are the unusually low minima for high Nb concentration in α′ and ω phases, reaching $E < 40$GPa for α′ and ω Ti-25at%Nb. For these two hexagonal structures the absolute minimum E is located at 45° with respect to the [0001] plane, which correspond to the [111] direction in a cubic or a tetragonal lattice. This minimum E calculated for certain directions seems to be the reason that causes the low VRH Young's modulus for the highest Nb compositions (Ti-33at%Nb). It should be notted that the study of the elastic properties of the orthorhombic structure (Figure 3.1.12) is especially interesting, since to our knowledge there are not available data.

The a" structure shows a very high dependence of the elastic modulus with the crystallographic direction as it is visible in the Young's modulus surface. The α″-phase presents the lowest Young's moduli values, around 30GPa along the [010] and the [100] directions (the unit cell orientations are shown in the inset of Figure 3.1.12). On the other hand the maximum modulus (~160GPa) is located along $\theta = \pm 30°$ or equivalent $\theta \pm 150°$ ($y = 0$ plane) directions for the experimentally observed compositions.

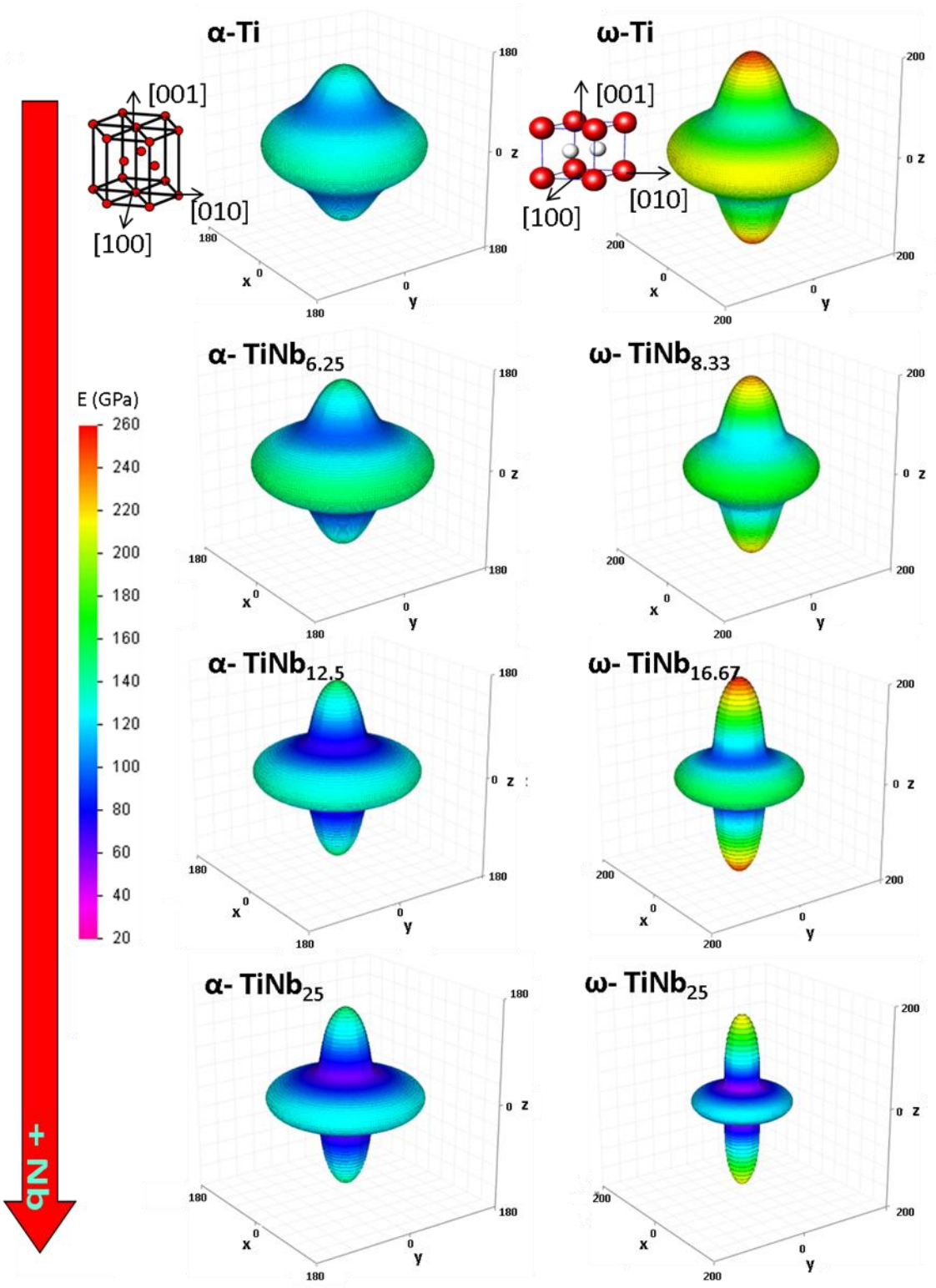

Figure 3.1.11 *Young's modulus surface of* **a)** *α and* **b)** *ω Ti-xNb upon Nb addition. The insets illustrate the crystallographic direction where X ~ [100], Y ~ [010] and Z ~ [001].*

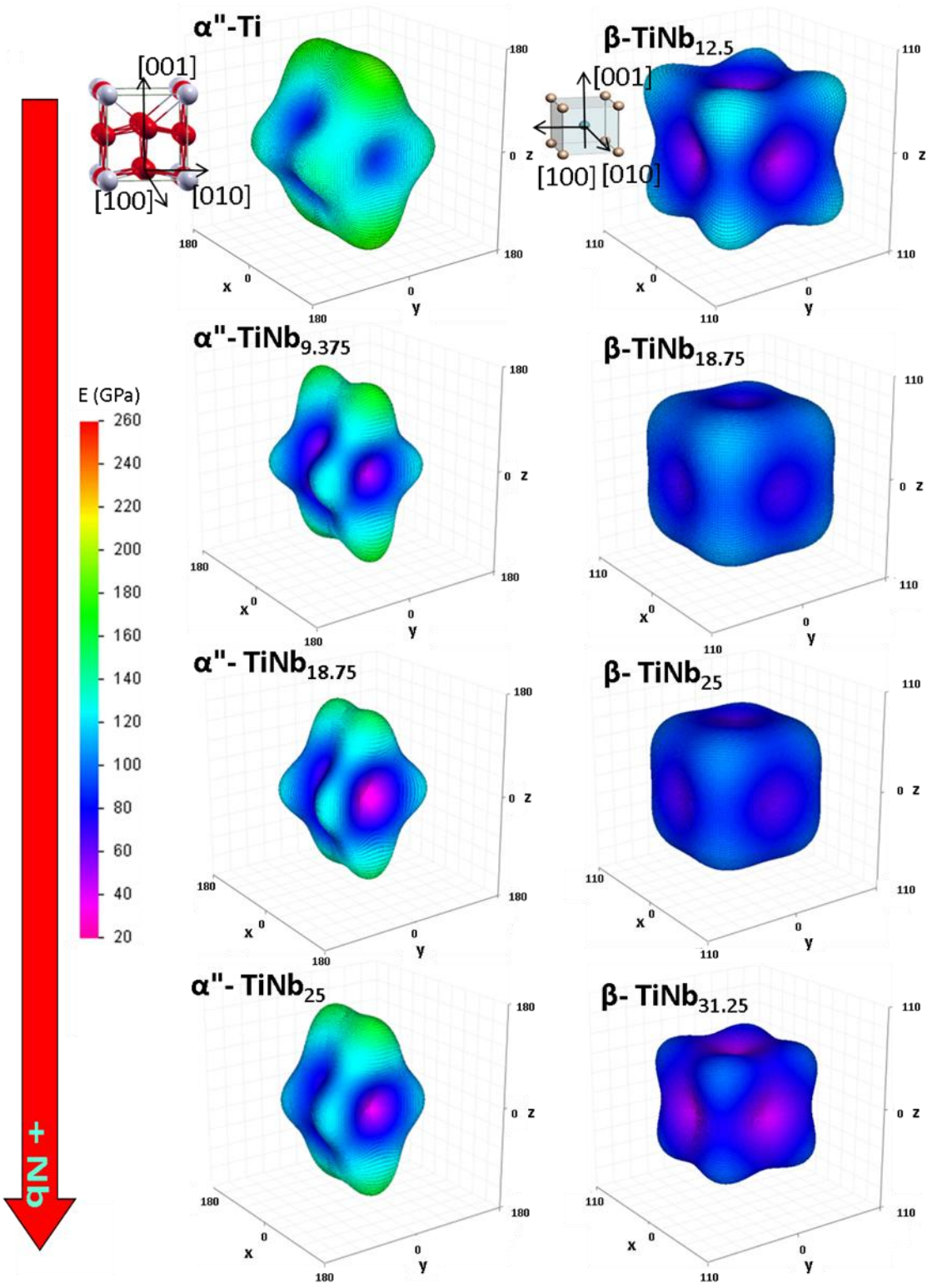

Figure 3.1.12 *Young's modulus surface of* **a)** *α and* **b)** *ω Ti-xNb upon Nb addition. The insets illustrate the crystallographic direction where X ~ [100], Y ~ [010] and Z ~ [001].*

The β-phase exhibits a much more homogeneous and isotropic behaviour, compared to the hexagonal cases. The β phase presents the lowest Young's moduli values (20-40GPa) along the [100] and equivalent [010]-[001] directions, while the maximum modulus is positioned towards the [111] axes, in agreement with previous theoretical [31] and experimental studies [32-35] where the sequence $E_\beta[100] < E_\beta[110] < E_\beta[111]$ have been empirically proved for Ti-Nb-based alloys.

From the analysis of the mechanical properties we can conclude in several main outcomes

i) Taking into account only stoichiometries of stable different phases we can state that the sequence of the Young's moduli follows the $E_\omega > E_{\alpha'} > E_{\alpha''} > E_\beta$ trend.

ii) Extremely low (even negative) or high values of E, B, G or ν may be used as indicators for the instability of the different structures

iii) According to the Pugh's law, the addition of Nb to Ti metal results, in general, in an improvement of the ductility

iv) The E dependence with Nb composition (w-shaped curve) could be a result of several Ti-Nb phases' coexisting in a polycrystalline system where the grain boundaries could also contribute

v) The α′ and ω phases' maximum directional Young's modulus values ($E_{\alpha'}$ = 140-150GPa and E_ω = 200-250GPa) are located along the [001] direction, while secondary a local maximum contained in the in-plane. In addition, the hexagonal phases lowest moduli (E < 40GPa) is found for the Ti-25at%Nb along the [111] direction.

vi) The α″-phase presents the lowest Young's moduli values, around 30GPa along the [010] and [100] directions while a high modulus (~160GPa) is found at θ = ±30° or equivalent θ ±150° (y = 0 plane) directions.

vii) The β phase presents the lowest Young's moduli values (20-40GPa) along the [100] while the relationship $E_\beta[100] < E_\beta[110] < E_\beta[111]$ was found for Ti-Nb-based alloys.

3.1.3 Conclusions

The main scope of this chapter was to identify possible relations between the mechanical, the structural and the electronic properties of the Ti-Nb alloys for their experimentally observed α′, ω, β and α″ phases. The quantum mechanical calculations predicted various phases that depend on Nb concentration, while in all structures the unit cell volume increases with Nb addition, in agreement with the experimental data.

From the EDOS it came out that the electronic depletion at the Fermi level (E_F) for α′ and ω Ti-($x \leq 9.375$)at%Nb is related with the phase stability at low Nb concentrations. In addition, the Nb-Ti *d*-electron hybridizations are responsible for the depletion of the occupied electronic states at the Fermi level, which characterize the β-Ti, thus leading in a stable bcc structure. Moreover, we found that Nb enrichment results in the enhancement of the number of *d*-electrons, while the main Nb contributions in the electronic density of states (EDOS) are located around -1eV. Furthermore, small Nb additions (≤ 18.75at%Nb) render the α″ structure more stable than the α′ or ω, whereas for Nb compositions above 25at%Nb the orthorhombic structure is unfavoured compared to the β-phase. From the partial EDOS of all phases, the maximum contribution is due to the *d*-electrons, which are located between -3.5 eV and E_F, and are, therefore, responsible for the states at the Fermi level. In addition, the partial *p*-electrons reveal a broad band located approximately between -6eV and E_F, while the *s* electrons occupy the lowest states (between -1eV and -6eV). These theoretical predictions are in agreement with the experimental results according to which the Ti-Nb system exhibits a variety of phases (including α′, ω, β and α″) depending on the Nb concentration.

Furthermore, the mechanical properties of the Ti-Nb alloys were studied good agreement between the experimental and theoretical results referring to the elastic constants were depicted. The mechanical stability conditions show destabilization of the α′ and ω structures upon Nb addition along with the stabilization of the β-phase for Nb-rich compositions (> 15at%Nb). Moreover, the ω-phase presents the highest Young´s moduli, 185GPa for pure Ti, while the corresponding values for the α′ phase are $E_{\alpha'}$ (Ti) = 134GPa. For both phases, E decreases linearly upon Nb addition. The shear moduli follow an analogous behavior compared to E, with 51GPa < $G_{\alpha'}$ < 26GPa and 75GPa < G_{ω} < 13GPa, respectively for the lowest (pure Ti) and the highest (Ti-33.33at%Nb) Nb concentrations. The bulk modulus of the α′ structure increases linearly from $E_{\alpha'}$(Ti) =

112GPa to $E_{\alpha'}$ (Ti-33.33at%Nb) = 135GPa whereas in ω-phase B presents a constant value of 120GPa. Concerning the ω-phase Poisson's ratio the pure Ti has the ν_{ω} (Ti) = 0.2 value which becomes double for the highest Nb composition (Ti-33.33at%Nb). For the hcp case, the Poisson's ration varies from $\nu_{\alpha'}$ (Ti) = 0.3 and $\nu_{\alpha'}$ (Ti-33at%Nb) = 0.4 for the pure and rich Nb content, respectively. Regarding the α″-phase, the elastic constants remain almost constant revealing the $B_{\alpha''}$ = 116GPa, $G_{\alpha''}$ = 39GPa, $\nu_{\alpha''}$ = 0.34 and $E_{\alpha''}$ = 105GPa for Ti-xNb (9at%Nb < x < 25at%Nb) values. On the other hand the higher E values were found for Nb compositions bellow 9at%Nb, while non linear behavior was predicted for the bulk moduli indicating instability. For β-Ti-xNb (15at%Nb ≤ x ≤ 31.25at%) the calculated elastic constants were approximately G_{β} = 31GPa, ν_{β} = 0.38 and E_{β} = 87GPa. B_{β} shows a linearly increasing behavior from B_{β} = 106GPa for pure Ti up to B_{β} = 132GPa for Ti-31.25at%Nb. Interestingly Ti-xNb (x < 12.5at%) compositions present extremely high Poisson's ratio values while E and G depict low moduli suggesting instability of β-Ti-xNb alloys with low Nb concentration. Another important outcome is that, according to the Pugh's law, the Nb substitution in the TiNb alloys could be related with the improvement of the ductility.

The calculated VRH-Young's moduli of all phases, reveals the sequence of $E_{\omega} > E_{\alpha'} > E_{\alpha''} > E_{\beta}$ for the Nb constants where all these phases coexist, in line with previous experimental works. Therefore, in this chapter is predicted that the well known w-shaped curve could be derived from the weighted average of the Ti-Nb phases that may coexist in the polycrystalline system. The α′ and ω directional elastic modulus exhibits the maximum E along the [001] direction ($E_{\alpha'}$ = 140-150GPa and E_{ω} = 200-250GPa), while the lowest moduli values (E < 40GPa) are located along the [111] direction. The α″-phase exhibits the lowest elastic moduli values, around 30GPa along the [010] and [100] directions, while the maximum modulus (~160GPa) is found at θ = ±30° or equivalent θ ±150° (y = 0 plane) directions. The β phase presents the lowest Young's moduli values (20-40GPa) along the [100] and the equivalent [010]-[001] directions. These results are in agreement with previous studies where the $E_{\beta}[100] < E_{\beta}[110] < E_{\beta}[111]$ sequence was found for Ti-Nb-based alloys [32]. These results could be used for the understanding of the phase transition on Ti-Nb systems and for the design of low-rigidity Ti-Nb-X alloys for biomedical implants.

3.1.4 References

1. D.L. Moffat, D.C. Larbalestier. The competition between martensite and omega in quenched Ti-Nb alloys. Metallurgical Transactions (1988) Volume 19, Issue 7, 1677-1686.
2. D. L. Moffat, D. C. Larbalestier. The competition between the alpha and omega phases in aged Ti-Nb alloys. Metallurgical Transactions (1988) Volume 19, Issue 7, 1687-1694.
3. D.L. Moffat, U.R. Kattner. The pressure-temperature phase diagram of pure titanium. The Stable and Metastable Ti-Nb Phase Diagrams. Metallurgical Transactions A. Volume 19A (1998) 2389-2397.
4. P. Söderlind, O. Eriksson, J.M. Wills, A. M. Boring. Theory of elastic constants of cubic transition metals and alloys Physical Review B 48 (1993) 5844.
5. H.Y. Kim, Y. Ikehara, J.I. Kim, H. Hosoda, S. Miyazaki. Martensitic transformation, shape memory effect and superelasticity of Ti–Nb binary alloys. Acta Materialia 54 (2006) 2419–2429.
6. A.T. Balcerzak, S.L. Sass. The Formation of the ω phase in Ti-Nb Alloys Metallurgical and Materials Transactions B. 3 (1972) 6.
7. M. Bönisch, M. Calin, L. Giebeler, A. Helth, A. Gebert, W. Skrotzki, J. Eckert. Composition-dependent magnitude of atomic shuffles in Ti-Nb martensites. Journal of Applied Crystallography 47 (2014) 1374-1379.
8. T. Ozaki, H. Matsumoto, S. Watanabe, S. Hanada. Beta Ti Alloys with Low Young's Modulus. Materials Transactions 45 (2004) 2776-2779.
9. J. Sun, Q. Yao, H. Xing, W.Y. Guo. Elastic properties of β, α" and ω metastable phases in Ti–Nb alloy from first-principles. J. Phys. Condens. Matter 19 (2007) 486215.
10. A.J. Prabha, S. Raju, B. Jeyaganesh, A.K. Rai, M. Behera, M. Vijayalakshmi, G. Paneerselvam, I. Johnson. Thermodynamics of α"-β phase transformation and heat capacity measurements in Ti–15at% Nb alloy. Physica B 406 (2011) 4200–4209.
11. A. Cremasco, P.N. Andrade, R.J. Contieri, E.S.N. Lopes, C.R.M. Afonso, R. Caram. Correlations between aging heat treatment, ω phase precipitation and mechanical properties of a cast Ti–Nb alloy. Materials and Design 32 (2011) 2387–2390.

12. T. Ahmed, H.J. Rack. Martensitic transformations in Ti-(16-26 at %) Nb alloys. Journal of Materials Science 31 (1996) 4267-4276.
13. D.L Moffat, D.C. Larbalestier. The competition between martensite and omega in quenched Ti-Nb alloys. Metallurgical Transactions 19 (1988) 1677.
14. R. I. Jaffee, N. E. Promisel. The science technology and application of titanium: proceedings of an international conference organized by the Institute of Metals and held at the Royal Festival Hall, London, (1968) Pergamon, Oxford.
15. A.R.G. Brown, D. Clark, J. Eastabrook, K.S. Jepson. The Titanium–Niobium System. Nature 210 (1964) 914–15.
16. S. Banumathy, R. K. Mandal, A.K. Singh. Structure of orthorhombic martensitic phase in binary Ti–Nb alloys. Journal of Applied Physics 106 (2009) 093518.
17. M. Bönisch, M. Calin, T. Waitz, A. Panigrahi, M. Zehetbauer, A. Gebert, W. Skrotzki, J. Eckert. Thermal stability and phase transformations of martensitic Ti–Nb alloys. Science and Technology of Advanced Materials 14 (2013) 055004.
18. R. Golesorkhtabar, P. Pavone, J. Spitaler, P. Puschnig, C. Draxl. ElaStic: A tool for calculating second-order elastic constants from first principles. Computer Physics Communications 184 (2013) 1861–1873.
19. J.F. Nye. Physical Properties of Crystals. Oxford University Press, Oxford (1985).
20. R.G. Hennig, T.J. Lenosky, D.R. Trinkle, S.P. Rudin, J.W. Wilkins. Classical potential describes martensitic phase transformations between the alpha, beta and omega titanium phases. Physical Review B 78 (2006) 054121.
21. E.S. Fisher, C.J. Renken. Single-Crystal Elastic Moduli and the hcp - bcc Transformation in Ti, Zr, and Hf. Physical Review 135 (1964) A482.
22. M. Ledbetter, H. Ogi, S. Kai, S. Kim, M. Hirao. Elastic constants of titanium's b.c.c. monocrystals. Applied Physics 95 (2004) 4642.
23. W. Petry, A. Heiming, J. Trampenau, M. Alba, C. Herzig, H.R. Schober. Phonon dispersion of the bcc phase of group-IV metals. I. bcc titanium. Physical Review B 43 (1991) 10933.
24. M. Tane, Y. Okuda, Y. Todaka, H. Ogi, A. Nagakubo. Elastic properties of single-crystalline omega phase in titanium. Acta Materialia 61 (2013) 7543-7554.
25. S. Miyazaki, H.Y. Kim, H. Hosoda. Development and characterization of Ni-free Ti-base shape memory and superelastic alloys. Materials Science and Engineering A 438– 440 (2006) 18–24

26. H. Hosoda, Y. Fukui, T. Inamura, K. Wakashima, S. Miyazaki, K. Inoue. Mechanical properties of Ti-based shape memory alloys. Materials Science Forum 426– 432 (2003) 3121–6.
27. R. Hill. The elastic behavior of a crystalline aggregate. Proceedings of the Physical Society. Section A Volume 65 Number 5 (1952).
28. C. Man, M. Huang. A Simple Explicit Formula for the Voigt-Reuss-Hill Average of Elastic Polycrystals with Arbitrary Crystal and Texture Symmetries. Journal of Elasticity 105 (2011) 29–48.
29. S.F. Pugh. Relations between the elastic moduli and the plastic properties of polycrystalline pure metals. Philosophical Magazine Series 7 45:367 (1954) 823-843.
30. G. Duffing, Die Schmiermittelreibung bei Gleitflächen von endlicher Breite; in Handbuch der Physikalischen und Technischen Mechanik, Bd. 3, Edited by F. Auerbach, W. Hort, Barth, Leipzig (1931) 249.
31. Q. Hu, S. Li, Y. Hao, R. Yang, B. Johansson, L. Vitos. Phase stability and elastic modulus of Ti alloys containing Nb, Zr, and/or Sn from first-principles calculations. Applied Physics Letters 93 (2008) 121902.
32. R. Hermann, H. Hermann, M. Calin, B. Buechner, J. Eckert. Elastic constants of single crystalline beta-Ti70Nb30, Scripta Materialia 66 (2012) 198-201.
33. M. Tane, S. Akita, T. Nakano, K. Hagihara, Y. Umakoshi, M. Niinomi, H. Nakajima. Peculiar elastic behavior of Ti–Nb–Ta–Zr single crystals. Acta Materialia 56 (2008) 2856–2863.
34. T. Inamura, H. Hosoda, K. Wakashima, S. Miyazaki. Anisotropy and Temperature Dependence of Young's Modulus in Textured TiNbAl Biomedical Shape Memory Alloy. Materials Transactions. 46 (2005) 1597–1603.
35. Y.W. Zhang, S.J. Li, E.G. Obbard, H. Wang, S.C. Wang, Y.L. Hao, R. Yang. Elastic properties of Ti–24Nb–4Zr–8Sn single crystals with bcc crystal structure. Acta Materialia 59 (2011) 3081–3090.

3.2 Ti-Nb-Hf alloys

3.2.1 Introduction

Implants' surfaces play an extremely important role in the response of the biological environment to the artificial medical devices [1-2]. In titanium implants the normal manufacturing steps usually lead to an oxidized, contaminated surface layer that is often stressed and plastically deformed, non-uniform and rather poorly defined [3].

Whereas it is known that for the low Nb substitution, the bulk Ti-Nb alloys exhibit several hexagonal or tetragonal phases (like α′, ω or α″) [4-7], Ti-xNb (22at%<x<95at%) thin films exhibit mainly the β-cubic phase [8]. Apart Nb, Hf is a non-toxic element fully miscible to Ti forming α+β solid solutions without intermetallic compounds, while its chemical similarities with Ti and its excellent corrosion resistant properties render the Ti-Hf system an interesting passive film for biomedical applications [9, 10]. The oxidation of the Ti-Hf films depends on the composition, while the XRD measurements exhibit mainly the α′-phase for these films without intermediate compound structures [11]. Interestingly, small amounts of Hf slightly affect the TiHf's dynamic Young's moduli, while they increase the tensile strength of the system [12].

The study of the ternary Ti-Nb-Hf system that may combine the two Ti-binary alloys' bio-friendly properties, emphasizing on the β-phase stabilization ability would be particularly interesting. Especially, in the thin film form, these Ti-Nb-Hf alloys could be of valuable use as coatings. However, to our knowledge reports on this topic are rather scarce.

In this chapter, a systematic analysis of the structural and electronic properties Ti-18.75at%Nb-xHf ($0 \leq x \leq 25$at%) alloys upon Hf substitutions has been carried out by means of the DFT-LAPW calculations. The ab initio calculations were compared with thin Ti-based films grown by Magnetron Sputtering and characterized by energy dispersive X-ray spectroscopy (EDS). The experimental part of this work has been carried out by our colleagues in the Department of Physics at the University of Ioannina. These results could be used for the understanding of the β-Ti based alloy's formation mechanisms having *sd* dopants aiming in the design of biocompatible materials.

3.2.2 Results and discussion

a) Structural and mechanical properties

The total energy calculations for the α″ versus the β phases are presented in Figure 3.2.1 for selective Hf substitution cases. The α″-orthorhombic phase is found energetically favoured compared to the β-phase with an energy difference of 0.05eV/atom. It should be notted that the α″ total energy's minimum values have been shifted to zero energy for comparison reasons. Although the α″ phase is found energetically favoured compared to the β-phase upon Hf substitution, the relative total energy difference between the two phases decreases which could indicates the initiation of the β-phase stabilization. Moreover, for both phases we found a shift of the total energy minimum to higher volumes, denoting a unit cell enlargement above 1 $Å^3$/atom between the lowest (Ti-18.75at%Nb-6.25at%Hf) and the highest (Ti-18.75at%Nb-25at%Hf) Hf compositions.

The initial structures were subjected under hydrostatic pressure and the total energy versus volume of the primitive unit cell curve was fitted determining the bulk moduli (inset in Figure 3.2.1) and the optimum lattice parameters (Figure 3.2.2(b)). The bulk modulus is given by the second derivative of the polynomium that was used in order to fit the ab initio Total Energy vs. Volume curve (Birch-Murnaghan equation of state). The estimated B values for the β-phase alloys show an inversely proportional increase of the moduli as a result of the Hf addition. In particular, the B_β for Ti-18.75at%Nb-6.25at%Hf was found 121GPa, while for the Ti-18.75at%Nb-25at%Hf a modulus of 116GPa was calculated. On the other hand, $B_{\alpha''}$ increases for the compositions between 6.25at%Hf and 18.75at%Hf, with values of $B_{\alpha''}$ = 125GPa and $B_{\alpha''}$ = 128GPa respectively for the low and high Hf concentrations. Nevertheless, $B_{\alpha''}$ decreases down to 127GPa for the highest Hf composition (Ti-18.75at%Nb-25at%Hf). It is interesting to note that the α″-phase's B values are higher than the B_β ones for all the simulated stoichiometries.

Figure 3.2.2(a) depicts the grazing incidence X-ray diffraction patterns of the deposited Ti-based films. A textured growth is preferred for the direction of the [002] lattice planes in contrast to the bulk Ti-based alloys for which the [110] peak was mainly observed. Small amounts of Nb and Hf result in the growth of the martensitic α″-phase. Keeping the Nb content constant at 17±1at% and increasing the Hf content causes a small shift of the [002] peak for Hf content above 10at% and gradually to the

deformation of the [021] lattice planes. For atomic Hf concentrations of 16at% the observed [021] peak is completely deformed simultaneously with a strong peak shift of the [002] to larger lattice distances (lower angles of detection). This finding suggests that Hf substitutions in the α″ phase (especially of the Ti atoms) induce strong deformation in the α″ lattice, eventually leading to phase transformation in the β-Ti. In Figure 3.2.2(a) the Ti-16at%Nb-16at%Hf film (blue line) is referred as β-Ti since the peak observed corresponds (although shifted possibly due to the internal film stresses) to the [110] peak position of the β TiNb structure.

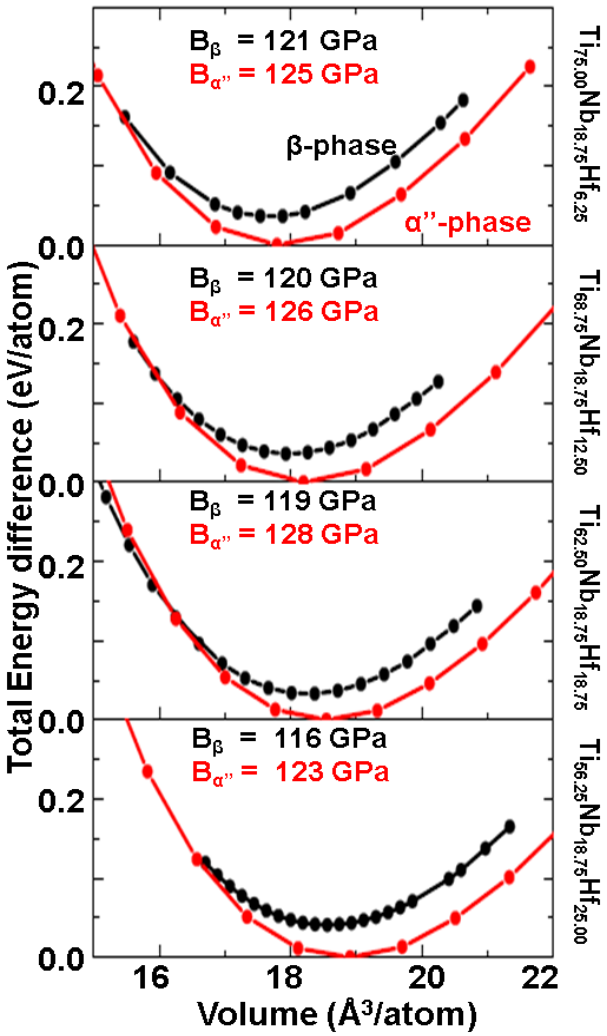

Figure 3.2.1 *Total energy under hydrostatic pressure versus unit cell's volume of* **a)** *Ti-18.75at%Nb-6.25at%Hf,* **b)** *Ti-18.75at%Nb-12.5at%Hf,* **c)** *Ti-18.75at%Nb-18.75at%Hf and* **d)** *Ti-18.75at%Nb-25at%Hf. Red and black points correspond to the α″ and β structures, respectively. The insets show the bulk moduli of the different lattices for all the stoichiometries.*

From the equilibrium volume we derived the crystals' lattice constants. In Figure 3.2.1(b), we present the ab initio results (filled circles) along with the available XRD data (open circles). Interestingly, although the theoretical data are made for small periodic unit cells they exhibit the same slope with the experimental thin film's data. Nevertheless all cases agree that upon Hf substitution the individual α″ and β lattice constants increase almost linearly following the Vegard's law.

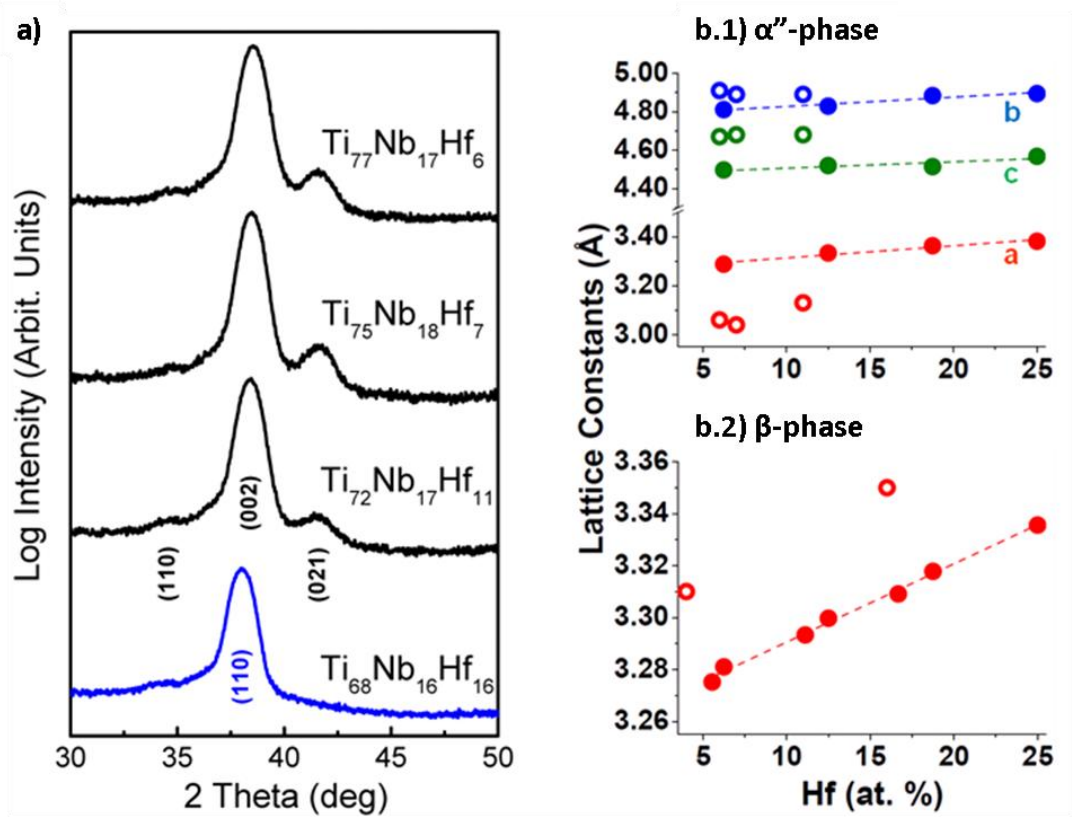

Figure 3.2.2 a) *Grazing incidence X-ray diffraction patterns of Ti-Nb-Hf films in distorted α″-Ti (black lines) and β-Ti (blue line) crystal structure.* **b)** *Lattice constants versus Hf substitution for: b.1) α″ and b.2) β phases. Filled and open circles correspond to ab initio and experimental data*

In line with the Ti-Nb phases transitions (Introduction chapter (1.3.2)), the α″-orthorhombic structure may be viewed as a transition between the hcp and bcc structures [13]. For instance, the hcp structure is obtained when y =1/6 and $b/a = \sqrt{3}$ while the bcc structure is obtained when y = 0 and $b/a = c/a = \sqrt{2}$ [14].

In Figure 3.2.3 the evolution of the y-parameter upon Hf addition is represented for the different first neighbour pairs of the energetically favoured conformation. The black dashed line depicts the perfect orthorhombic y-parameter (y = 0.10).

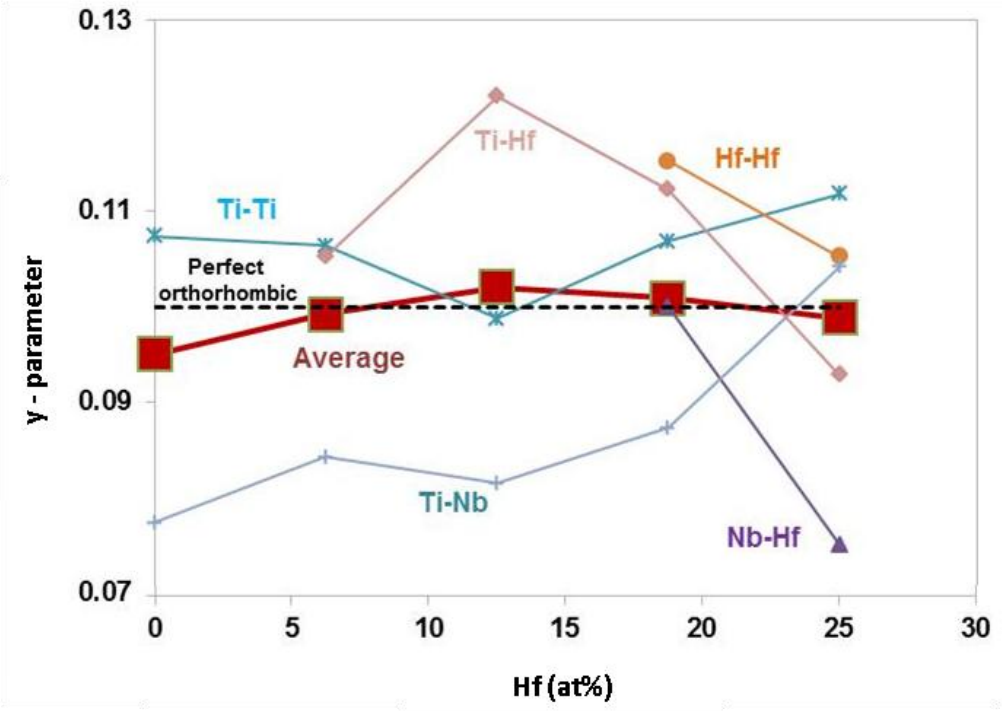

Figure 3.2.3 *Orthorhombic y-parameter as a function of the Hf addition for Ti-18.75at%Nb-xHf. The different lines correspond to each possible atomic pairs.*

All Hf atoms, including pairs (Nb-Hf, Ti-Hf and Hf-Hf), contribute to the decrease of the total *y* values that is characteristic for the $\alpha'' \rightarrow \beta$ phase transition. It is important to note that in Hf-rich alloys, the number of Hf containing pairs is higher resulting in an overall decrease of the *y* value leading to the experimentally measured $\alpha'' \rightarrow \beta$ phase transition. In addition, Ti-Nb pairs take values below 0.09 for Ti-18.75at%Nb-(x ≤ 18.75)at%Hf, while for the highest Hf composition y increases above 0.10. The Ti-Nb y values are important for the transition to bcc phase, while the high y values at the Ti-18.75at%Nb-25at%Hf is less significant due to the small percentage of Ti-Nb pairs in the Hf-rich compounds. Concluding, it seams that at low Hf concentration the Ti-Nb pairs contribute in the transition from the α″ to β phase, while the *y*-parameter will decrease progressively as a result of the Hf substitution, with a main contribution of the Nb-Hf pairs. It is worth to be noted, that our ab initio calculations were limited by the small unit cells' size, containing only 16 atoms. Nevertheless, the results of this chapter could be used for the understanding of the y value behavior in the Ti-Nb-Hf system.

b) Electronic properties

For the energetically favoured atomic rearengement of the ternary alloys and the equilibrium lattice of all stoichiometries and phases, the Electronic Density of States'

(EDOS) have been calculated aiming to understand to possible electronic origin of the α″ → β phase transition [15]. In Figure 3.2.4, we present the α″ and β Ti-18.75at%Nb-xHf (x = 6.25 and 25.00at%) total and partial density of states. The row sequence corresponds to the total, *d*, *p* and *s* electron contributions, while the perfect structure and the structure after ionic relaxation EDOSs are respectively depicted by thin and bold traces.

In Figures 3.2.4 and 3.2.5 we can observe that the α″ and β phases exhibit low electron occupation (pseudogap) at the E_F and higher occupation of states bellow E_F, especially at high Hf compositions. These features are characterized by a highly occupied local minima at E_F, which is visible in α″ and β Ti-18.75at%Nb-(6.25 ≤ x ≤ 25)at%Hf compositions, revealing the metastable character of these structures. Concerning the partial EDOS we can observe that Nb *d*-electrons are distributed between -3.5eV and E_F with the presence of two main peaks at -1eV and -2eV. The *d*-Ti-Nb-Hf hybridizations are mainly responsible for the states around the Fermi level and subsequently responsible of the stabilization or destabilization of the different structures. Moreover we can see that Nb and Ti dominate the *d*-EDOS, especially below -1.5eV, while in the *p* - EDOS all atoms contribute equally close to the Fermi level. In addition the partial *p*-electrons, although with a contribution of almost ten times smaller compared to *d*-electrons, also participate in the depletion of the E_F. In analogy to the *p*-electrons, the *s* electron occupation is smaller compared to the participation of the *d*-electrons in the total EDOS around the Fermi level, while Hf has the highest occupation at the lowest energies of the *s*-EDOS. The Ti-Nb-Hf hybridizations are also visible in the *s*-electrons, where a broad band from approximately -6eV to -1eV appears with a peak located around -2.5eV, reaching an occupation of approximately 0.15 states/eV/atom.

In addition Hf *f*-electrons play a very important role, being responsible for a very high peak at low energy values, which is visible in the total EDOS bellow -11eV of Hf-rich compositions. These well bonded states are crucial for the stabilization or the destabilization of the α″ and β phases.

In the total orthorhombic EDOSs, similar features emerge in the region around the Fermi level upon Hf addition that are mainly due to the Ti *d*-electron participations with an overall depletion at the highest Hf (25at%). Although the different Hf contents result in comparable *d*-EDOSs, the states of 6.25at%Hf substitutions, referring to the α″-phase, are slightly enhanced around -0.5eV compared to 25at% Hf, while far below E_F

the opposite is true. In reference to the partial *s*, *p* and *d* orbitals there are not appreciable differences between the relaxed and unrelaxed system.

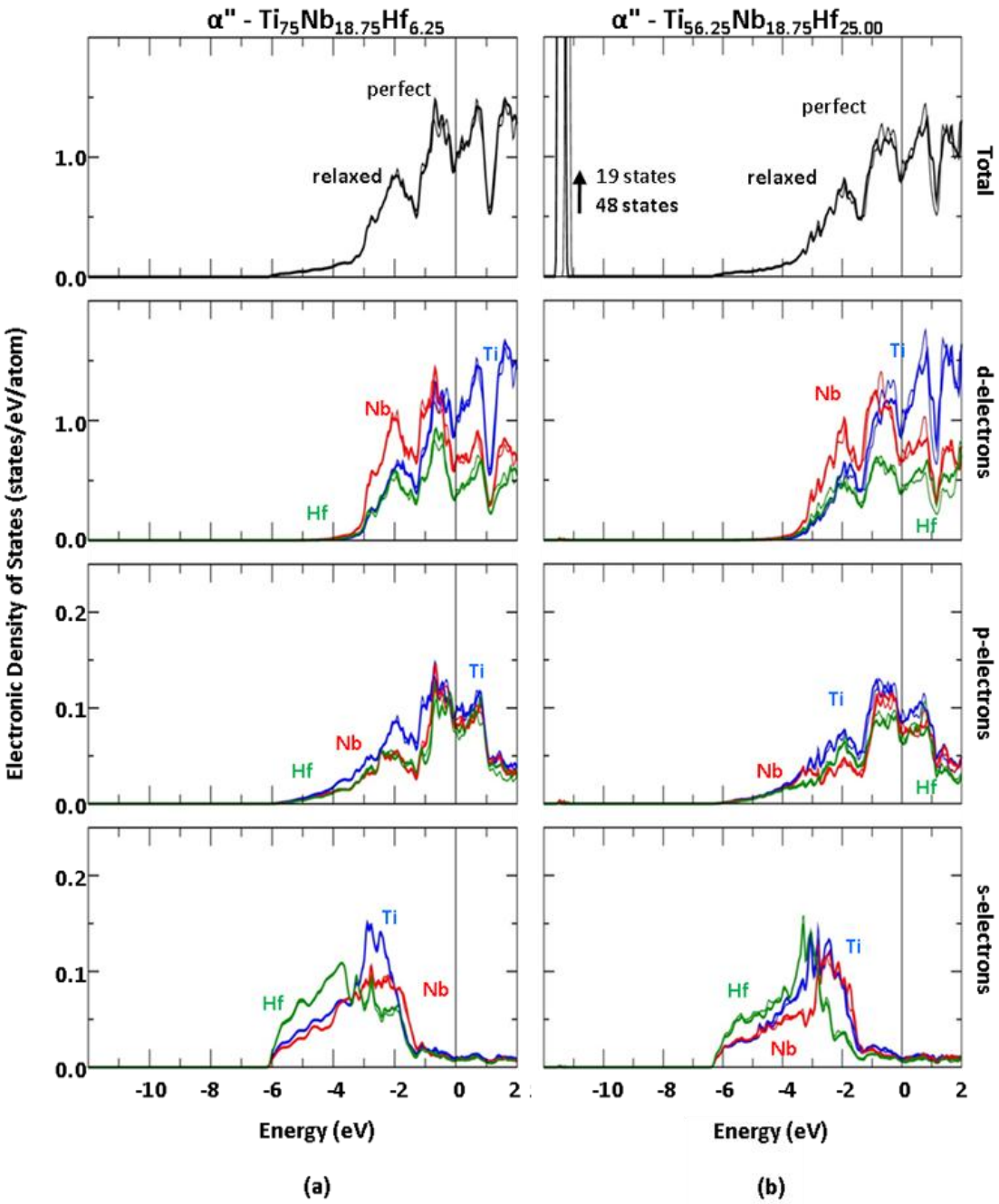

Figure 3.2.4 *Electronic density of states of α"-phase:* **a)** *Ti-18.75at%Nb-6.25at%Hf for the total, d, p and s contributions lied up from the first up to fourth row, respectively, and* **b)** *stands for Ti-18.75at%Nb-25at%Hf. The contribution due to perfect ideal structure is represented by a thin line and the final structure after ionic relaxation with a thicker trace.*

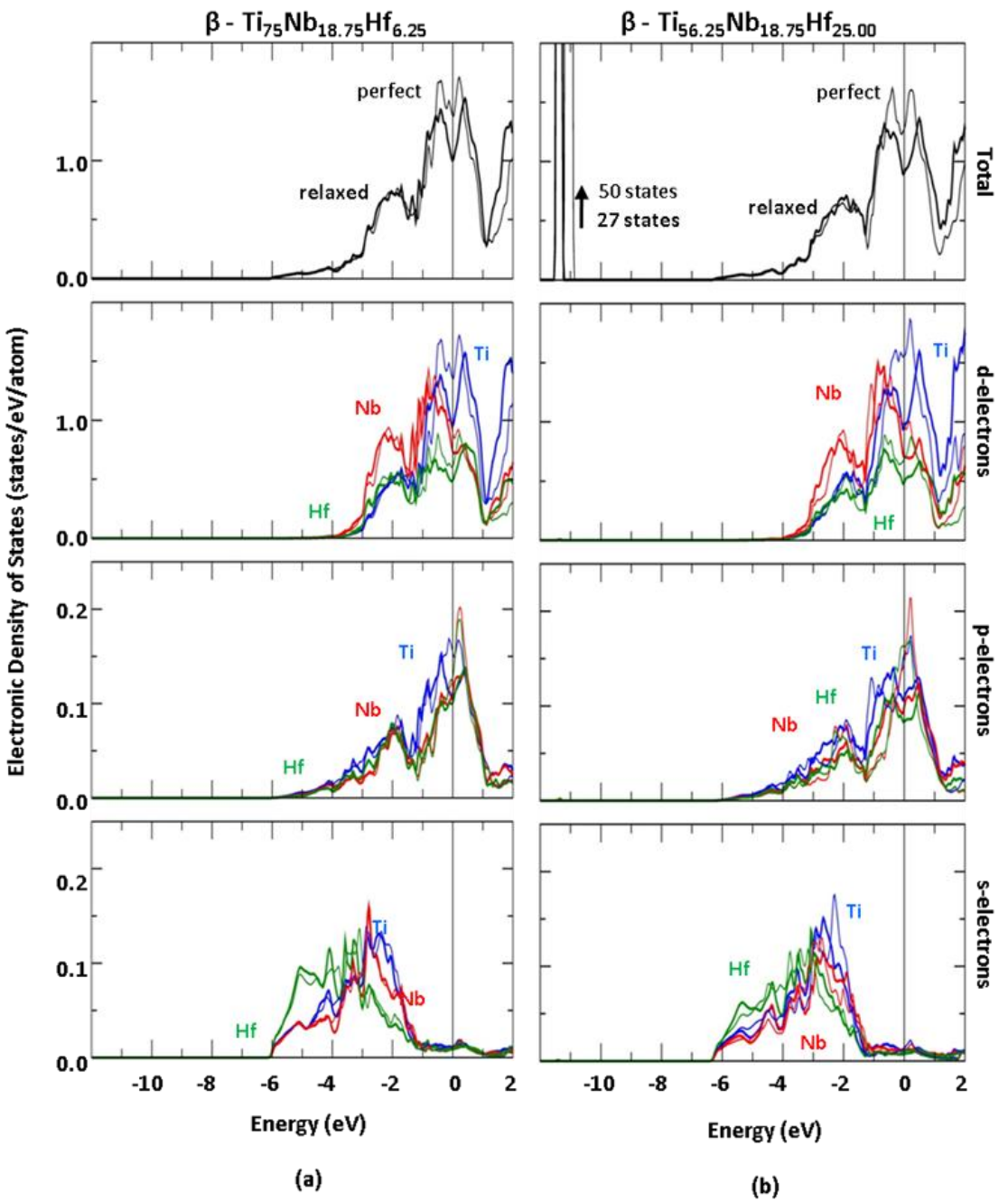

Figure 3.2.5 *Electronic density of states of β-phase:* **a)** *Ti-18.75at%Nb-6.25at%Hf for the total, d, p and s contributions lied up from the first up to fourth row, respectively, and* **b)** *stands for Ti-18.75at%Nb-25at%Hf. The contribution due to perfect ideal structure is represented by a thin line and the final structure after ionic relaxation with a thicker trace.*

It is interesting to note that for the α″-Ti-18.75at%Nb-12.5at%Hf alloy the low energy peak stands below -11eV, which is due to the *f*-Hf contribution presenting only in the perfect case due to the increase of the Hf-Hf distance after the ionic relaxation. It should be notted that the the sharp minimum of the α″ EDOS could be associated with the shape memory effect that characterizes the orthorhombic phase.

Turning on the β-phase EDOS (Figure 3.2.5) we revealed that the Hf *d*-electrons contributions are responsible for the depletion of the occupied electronic states at the Fermi level, crucial for the stability of the bcc structure. The *d*-electrons are located between -3.5eV and E_F being mainly responsible for the pseudogap at the Fermi level, while the main *d*-Nb contributions in the EDOS are located around -1eV. This diminution of states at the Fermi level can be also observed in the Hf and Nb *p*-electrons. Moreover, we can see that the *s*-electrons are shifted to lower energy states as a result of the Hf addition, favouring the β-phase stability. The combination of the depletion of states at E_F and the translation of states to lower energies denotes the stability of the bcc phase subsequent of the Hf substitution. In addition we can see again a high peak due to Hf *f*-electrons that appears in the β-Ti-18.75at%Nb-25at%Hf due to the Hf-Hf neighbourhood, which may influence the stabilization of β-Ti-Nb-Hf alloys. This atomic conformation, with Hf-Hf pairs as first neighbours, although in principle is not energetically favoured, is difficult to be avoided in rich-Hf stoichiometries. In addition, the difference between the relaxed and perfect system's EDOS is more pronounced in the β-phase compared to the orthorhombic. This difference in the DOS is more visible around E_F. In all β-phase systems, the reduction of the electrons in the region around $E_{F,}$ after ionic relaxation, leads the system to an expected more stable structure. This variation is more visible in the relaxed Ti-18.75at%Nb-25at%Hf where the states at the Fermi level are drastically reduced compared to the unrelaxed system even for the lower Hf compositions. This variation is mainly due to the difference between the unrelaxed and the relaxed *d*-Ti contribution. The combination of these phenomena may induce the progressive stabilization of the bcc phase subsequent to the substitutional addition of Hf.

In conclusion, the physical insight of the β emergence and the interrelated destabilization of α″ could be related to the new electronic features caused by the Ti-Nb-Hf hybridization. The partial EDOS shows an analogous behavior of the α″ and β phases, while the maximum contribution next to the Fermi level is due to the *d*-electrons. In the orthorhombic case the maximum contribution at the Fermi level is due to *d*-Ti contribution whereas in the bcc structure the *d*-Ti electrons present a minimum at E_F contributing to the stabilization of the β phase. On the other hand, an energy state with the absolute Hf *f*-electrons character is localized at low energy states (< 11 eV) appearing in both the α″- Ti-18.75at%Nb-(x ≥ 18.75)at%Hf and the β-(Ti-18.75at%Nb-

25at%Hf) due to Hf-Hf nearest neighbours interaction lowering therefore the corresponding band energy. In addition the partial *p*-electrons of the β-phase, although with a smaller contribution compared to *d*-electrons, are also responsible for the depletion of the states at E_F while the *s*-electrons are shifted to lower energy values upon Hf addition. These variations may help to stabilize the β structure against the α″-orthorhombic for rich-Hf stoichiometries.

3.2.3 Conclusions

In this chapter, a combination of theoretical and experimental data concerning the phase stability of α″ and β phases of Ti-Nb-Hf was presented. Ti-based thin films with Nb around 17at% and various Hf substitutions were grown by Magnetron Sputtering. At low Hf compositions the α″-phase is the preferred structure, while there is a critical composition, between 11at%Hf and 16at%Hf attending to the XRD measurements, in which a transition from α″ to β phase is found. Both thin films measurements and bulk total energy calculations agree that the unit cell volume and the corresponding lattice constants increase upon Hf substitution. The overall decrease of the *y*-parameter suggests the progressive $\alpha'' \rightarrow \beta$ phase transition subsequent to the Hf addition. The physical or the electronic origin of this phenomenon is attributed to the Hf 5d hybridizations that decrease the total *d*-electron occupation at the Fermi level and shift the lowest energy *s*-electrons' states below -6eV, in conjunction with *p*-electron hybridizations occurring close to E_F. In addition the Hf *f*-electrons reveal an inhanced peak at states bellow -11eV due to the Hf-Hf first neighbours' interactions which may influence critically the stabilization of the β structure. These results could be of use for the design of β-Ti-Nb-Hf alloys suitable for biomedical applications.

3.2.4 References

1. X. Liu, P.K. Chu, C. Ding. Surface modification of titanium, titanium alloys, and related materials for biomedical applications. Materials Science and Engineering Reports, Volume 47, Issue 3-4 (2004) 49-121.
2. M. Lorenzetti, E. Pellicer, J. Sort, M.D. Baró, J. Kovač, S. Novak, S. Kobe. Improvement to the Corrosion Resistance of Ti-Based Implants Using Hydrothermally Synthesized Nanostructured Anatase Coatings. Materials 2014, 7(1), 180-194; doi:10.3390/ma7010180.
3. M. Niinomi. Metals for biomedical devices. Woodhead Publishing Limited (2010)
4. T. Ozaki, H. Matsumoto, S. Watanabe and S. Hanada. Beta Ti Alloys with Low Young's Modulus. Materials Transactions 45 (2004) 2776-2779.
5. C.M. Lee, C.P. Ju, J.H. Chern Lin. Structure–property relationship of cast Ti–Nb alloys. Journal of Oral Rehabilitation Volume 29, Issue 4 (2002) 314–322.
6. R. Hermann, H. Hermann, M. Calin, B. Büchnera, J. Eckert. Elastic constants of single crystalline beta-Ti70Nb30. Scripta Materialia 66 (2012) 198-201.
7. S. Banumathy, R.K. Mandal, A.K. Singh. Structure of orthorhombic martensitic phase in binary Ti–Nb alloys. Journal of Applied Physics106 (2009) 093518.
8. A.I. Mardare, A. Savanb, A. Ludwigb, A. D. Wieckb, A. W. Hasselet. High-throughput synthesis and characterization of anodic oxides on Nb–Ti alloys. Electrochimica Acta 54 (2009) 5973–5980.
9. J.L. Murray, in: T. Massalski, H. Okamoto, P. Subramanian, L. Kacprzak. Binary Alloy Phase Diagrams (1990) 2118.
10. Z. Cai, M. Koike, H. Sato, M. Brezner, Q. Guo, M. Komatsu, O. Okuno, T. Okabe. Electrochemical characterization of cast Ti-Hf binary alloys. Acta Biomaterialia 1 (2005) 353–356.
11. A. I. Mardarea, A. Ludwigb, A. Savanb, A. D. Wieckb, A. W. Hassela. High-throughput study of the anodic oxidation of Hf–Ti thin films. Electrochimica Acta 54 (2009) 5171–5178.
12. Y.L. Zhoua, M. Niinomi, T. Akahori. Changes in Mechanical Properties of Ti Alloys in Relation to Alloy ing Additions of Ta and Hf. Materials Science and Engineering A 483–484 (2008) 153–156.

13. J.P. Morniroli, M. Gantois. Investigation of the conditions for omega phase formation in Ti-Nb and Ti-Mb alloys. Memoires et etudes scientifiques de la revue de metallurgie. 70 (1973) 831-842.
14. C. Li, H. Luo, Q. Hu, R. Yang, F. Yin, O. Umezawa, L. Vitos. Lattice parameters and relative stability of α″ phase in binary titanium alloys by first-principles calculations. Solid State Communications 159 (2013) 70-75.
15. P. Soederlind, O. Eriksson, J. M. Wills, A.M. Boring. Theory of elastic constants of cubic transition metals and alloys. Physical Review B 48 (1993) 5844.

3.3 Ti-Nb-In alloys

3.3.1 Introduction

In this chapter, the influence of In substitution in the Ti-25at%Nb alloy has been studied. Indium has *s* and *p* valence electrons, which possess an electronic configuration ($4d^{10}5s^{2}5p^{1}$), very similar to Sn ($4d^{10}5s^{2}5p^{2}$). Therefore, the addition of In to Ti-25at%Nb is expected to resul similar properties with the Sn case. Indium has been also suggested to act as a β-stabilizer element [1, 2] while interestingly it's pure In tetragonal phase (space group I4/*mmm* No. 139) presents very low Young's modulus (E_{In} = 11GPa). In addition, indium is biocompatible [3-5] and its low melting point ($T_{m,In}$ = 429K) could also decrease the high Ti-Nb alloy melting temperature. Moreover, the indium presence in the Ti alloys has been reported [6-8] to generate a wide range of microstructures with improved characteristics (e.g. low Young's modulus) [7-9]. For these reasons, we considered the Ti-25at%Nb-xIn ternary alloys as promising candidates in the field of biomaterials.

In this thesis the effect of indium (In) additions in the structural and electronic characteristics of β-Ti-25at%Nb-xIn (x≤25at%) alloys were investigated by DFT calculations while the theoretical results were compared with the β-type (Ti-40wt%Nb)-xIn alloys (with x ≤ 5.2 wt%) produced by cold-crucible casting and subsequently heat treated at 1273K (single β-phase) and water quenched. The experimental part was carried out by our colleagues at IFW Dresden [9].

3.3.2 Results and discussion

a) Structural properties

Figure 3.3.1 depicts the X-ray diffraction patterns (XRD) of (Ti-40wt%Nb)-(x ≤ 5wt%)In together with the lattice constants calculated from the XRD data and ab initio calculations of β-Ti-25at.%Nb-(x ≤ 12.5at%)In. The XRD measurements in Figure 3.3.1(a) revealed a solid solution microstructure in the β-phase for all studied alloys, probably due to high amount of β-stabilizers and the high cooling rates, while no evidenced of a secondary phase like α″ or ω as a result of indium addition were found that explain a further increase of the Young's modulus [7]. In line with the bulk Ti-based alloys, the highest intensity first peak corresponds to the [110] orientation which is the preferred one and corresponces to the first textured preferred growth direction.

Figure 3.3.1(b) shows a linear increase dependence between the In content and the lattice parameter of the β-Ti-25at%Nb-(x ≤ 25at%)In. This could be related with the radius of In (r_{In} = 0.1659 Å) that is about 13.9% higher compared to Nb and Ti (r_{Ti} = 0.14615 Å, r_{Nb} = 0.1429 Å). Consequently, the substitution of indium atoms expands the lattice constant leading to the increase of the β-phase lattice constant as manifested in both experimental and theoretical approaches. These results are in line with the experimental XRD measurements performed by Rietveld analysis [8] where the differences in the absolute values could be attributed to the tiny monocrystalline unit cells of DFT simulations along with the different temperature and pressure conditions (0K and 0GPa in ab initio versus room conditions in the experiment). Nevertheless, the slopes obtained by both methods are very similar, confirming the enlargement of the bcc lattice parameter upon indium inclusion.

In the ab initio calculations the atomic distribution of Ti, Nb and In atoms in the unit cell were considered and although the lattice constant values were not affected, the total energy and the electronic properties were altered between the several rearrengements. Using the ab initio total energy difference (ΔE), we obtained valuable information regarding the bcc phase characteristic, helping us to an easier comparison among various atomic environments and indium contents. The calculated total energy difference shows several values depending on the indium's first neighbourhood (FN). Figure 3.3.2 illustrates the ΔE evolution with indium amount for the three studied compositions in Ti-FN, Nb-FN and mixed (Ti-Nb)-FN atomic environments. The change of ΔE as a function of atomic environment is: $\Delta E_{Ti\text{-}FN} < \Delta E_{(Ti\text{-}Nb)\text{-}FN} < \Delta E_{Nb\text{-}FN}$ for each studied ternary composition, where a lower ΔE indicates a more energetically favoured configuration. These results show that In always prefers the Ti first neighbourhood (Ti-FF) (illustrated in inset of Figure 3.3.2) against In and Nb (Nb-FF), in line with the experimental findings referring to the homogenous solution of In [9]. Interestingly, Nb atoms are the energetically unfavoured In's first neighbours (Nb-FN).

This was also confirmed by EDOSs and WFs [9] calculations which revealed that in all energy states In-Nb bonding orbitals are absent. No hybridisation was found for the In-Nb pairs, in line with the large positive heat of mixing ($\Delta H_{mix,Nb\text{-}In}$ = 15 KJ/mol) between these atoms [9]. The positive heat of mixing between In and Nb may allow compositional modulations (or phase separation) in the β-type Nb-rich solid solution [10]. Such compositional modulations were recently reported in some β-type Ti-based

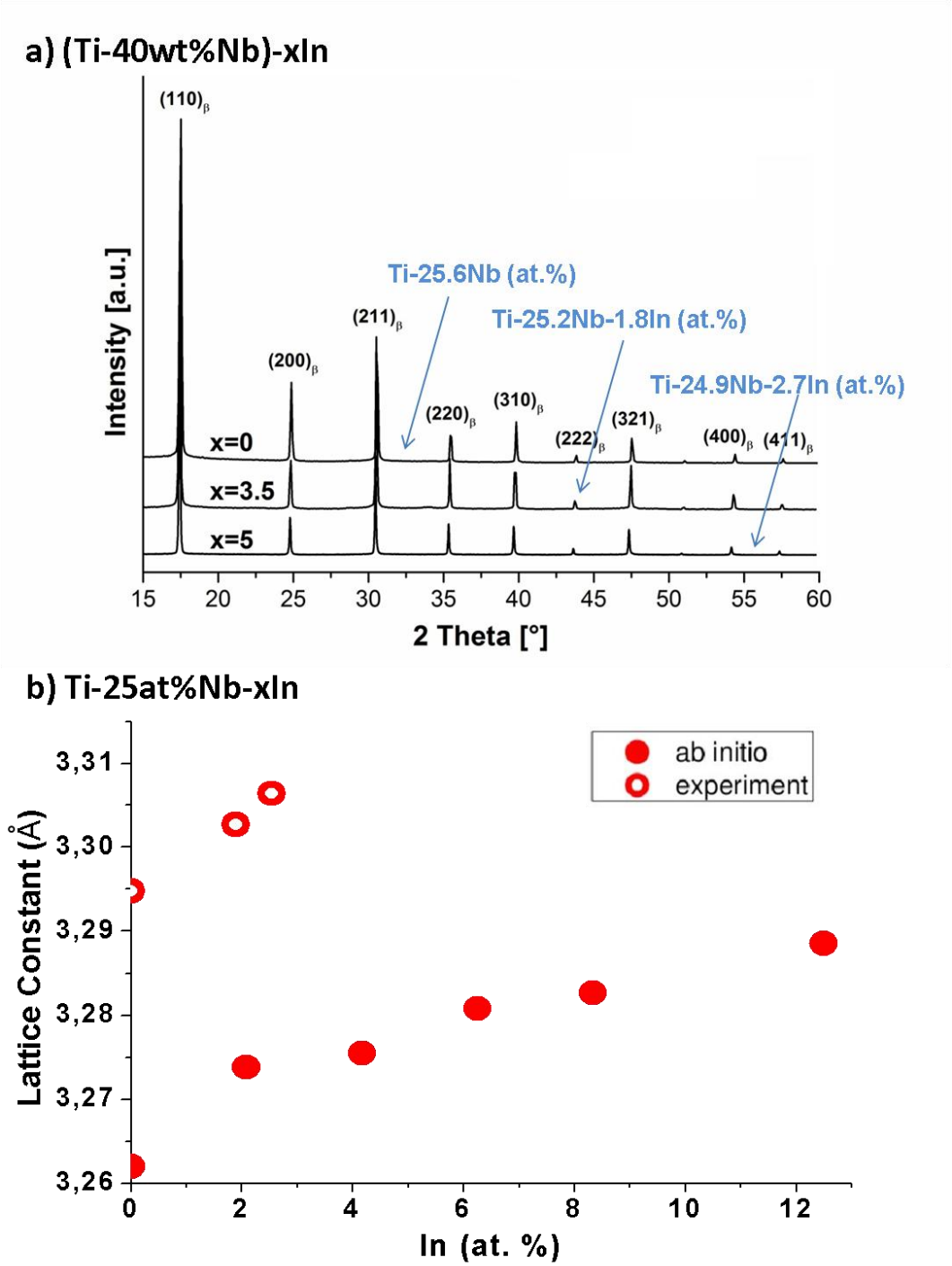

Figure 3.3.1 a) *XRD patterns of (Ti-40Nb)-xIn (x = 0, 3.5 and 5 wt%) samples revealing a single β-phase structure* **b)** *β-Ti-25at%Nb-xIn lattice constants varying with In substitution. Filled and open circles correspond to ab initio and experimental data, respectively.*

alloys with high β-stabilizers concentrations, e.g. in Ti-Mo [11] For the ternary Ti-25at%Nb-2.08at%In case, the Ti-FN is the energetically favoured conformation, while the total energy difference between the Ti-FN and TiNb-FN atomic rearrangements is

almost 0.5eV. These findings suggest that in this atomic environment, indium may act as supplementary bcc β-phase stabilizer along with Nb, while for the Nb-FN environment the opposite is true. For the Ti-25at%Nb-2.78at%In composition, the ΔE values are higher than the binary case for all atomic environments. In addition the total energy difference between the preference of Ti-FN against TiIn-FN or TiNb-FN may vary from 0.5 up to 1eV. These higher ΔE values suggest that the highest In-containing alloy tends to form less stable bcc crystal lattice than the binary (In-free) Ti-25at%Nb composition. As a summary, we can say that the present ab initio simulations showed that depending on the atomic environment, and especially at higher content, In destabilizes the bcc phase.

b) Electronic properties

The influence of In in the Ti-25at%Nb binary alloy concerning the electronic character and the β-phase stabilization or destabilization could be described using the EDOS features. For the energetically favoured Ti-FN atomic environment we evaluated the electronic density of states for the β-type Ti-25at%Nb-xIn (x = 2.08 and 12.5at%) (Figure 3.3.3), ternary alloys. The EDOS of the pure Ti and Nb as well as Ti-25at%Nb EDOS have been also included in the first column for comparison. Regarding the pure β-Ti EDOS, we observe two main energy bands located around -2eV and at the Fermi level (E_F = 0 eV) separated by a minimum at -1eV. Close to E_F a local pseudogap at +0.1eV is found between the highest occupied state (around -0.5eV) and the first unoccupied one (at 0.25eV), which denotes metastability for this structure. Such a minimum was also depicted in the binary Ti-25at%Nb and ternary Ti-25at%Nb- (In ≤ 4.17)at%In cases. The pure β-Nb EDOS exhibits a low energy band around -2.5 eV, while the next one is located far from E_F, denoting higher stability of the Nb β-phase compared to the previous cases. For these low In stoichiometries, the total-EDOS bands of ternary compositions are mainly situated from -5.5eV up to the Fermi level similarly to the Ti-25at%Nb EDOS. Nevertheless the presence of In introduces a well localized low energy peak between -6.5 eV and -7 eV, which has a clear *s* character, denoting stability increase. This state is approximately 1eV lower than the other energy states denoting its stability. In addition, the maximum at -2eV and the pseudogap located at the Fermi level remain almost unaltered for small additions of In, denoting the metastability of the β-phase Ti-25at%Nb-(In ≤ 4.17)at%In ternary alloys.

Regarding the stoichiometries with higher In concentration, Ti-25at%Nb-(In ≥ 8.33)at%, we can observe some significant changes in the EDOS compared to the smaller compositions. Upon In addition the EDOS exhibits a peak at the Fermi level, filling the minimum that was present at low In compositions. In addition, the low energy peak is drastically depleted, resulting in a general reduced occupancy in the occupied states. These two main features denote the instability of the β-phase for these compositions [6]. In the case of the highest indium content, Ti-25at%Nb-25at%In, the EDOS exhibits a deep minimum around 0.5eV, which is shifted to low energy states compared to the lower In compositions. Nevertheless, the decreasing occupancy trend from the occupied to the unoccupied states denotes instability, which is visible due to the depletion of the energy states around -2eV. In addition the small filling of the EDOS depicted in the broad energy band from between -10eV and -5eV suggests that the 25at%In β-phase is energetically unfavoured compared to Ti-25at%Nb-(x ≤ 4.17)at%In substitutional cases [6]. It is worth to be noted that, following an analogous behavior compared to Ti-25at%Nb-Sn alloys [12], the alterations at E_F are due to the relative compositional changes upon In substitutions and not to direct In contributions. This behavior is depicted in the partial *s*, *p* and *d* EDOSs, in which we can see that the *d*-electron EDOS is mainly due to Nb and Ti partial contributions.

Concerning the partial EDOS we can see *d*-electron contribution above -4eV that is due to Nb and Ti atoms. In particular, Ti is mainly responsible for the EDOS features at E_F, while there is almost no contribution of In at this state.

These *d*-electrons hybridizations as well as the presence of a local total- or *d*-EDOS minimum at the E_F are very important, since the shape and filling of the *d*-band is known to be correlated with the phase stability [6]. Such a minimum was also found in the similar case of Ti-25at%2.08at%Sn (Ti-38wt%Nb-4wt%Sn) ternary alloy EDOS [12]. Furthermore, the *p*-EDOS is also present below -4.0eV, mainly due to In-*5p* electrons, while the Ti-*3p* and Nb-*4p* semi-core electrons contribute mainly at energies higher than -1eV.

For the 12.5at% and 25at% In percentages the Nb d-electron states are shifted to higher energies, up to the Fermi level contributing to the destabilization of these compositions. This phenomenon was also present in Ti-Nb-Sn alloys, at much higher Sn contents (Ti-25at.%Nb-12.5at.%Sn or Ti-34wt%Nb-21wt%Sn) where the β-phase instability is denoted by a peak at the Fermi level [12], whereas In atoms are dominant in the *s* and *p*

partial EDOSs and the lowest energy states. A broad band energy from E_F to -5eV are due to the *p*-electron EDOS, while the states from -5eV until -8eV are due to the *s*-electrons contribution. These findings suggest that the substitutional addition of In may influence the stabilization of the bcc phase for low In concentrations (Ti-25at%Nb-(x ≤ 4.17)at%In) by the appearance of lower energy states, while higher substitutions could lead to the destabilization of this phase.

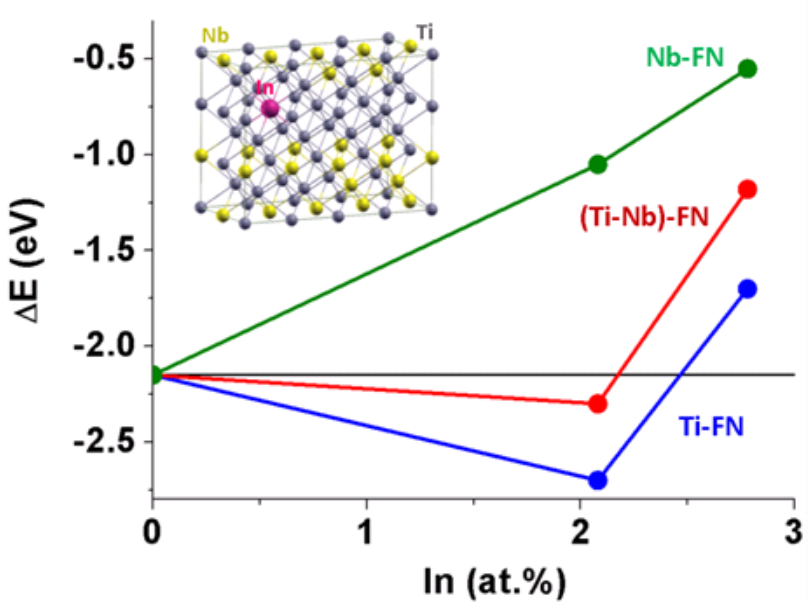

Figure 3.3.2 *Total energy difference (ΔE) of Ti-25at%Nb, Ti-25at%Nb-2.08at%In and Ti-25at%Nb-2.78at%In for the Ti-FN (blue), Nb-FN (green) and the mixed TiNb-FN (red) atomic environments. ΔE of binary composition (black line) is set as the reference level. In the inset, the Ti-FN energetically favoured atomic configuration is shown; where grey, yellow and magenta balls correspond to Ti, Nb and In atoms.*

The main Ti, Nb and In EDOSs' peaks are interesting for the existence of possible hybridizations and therefore were investigated in detail. At minor In additions, the analysis found low energy states with *s* character that exhibit basically antibonding features with the Ti first neighbouring atoms and with the Ti-Nb second neighbouring atoms. This phenomenon will lead to a weakening of the chemical bonds in the system and the subsequent elastic softening. At higher In contents, In atoms may become first or second neighbours revealing strong σ-bond features while the presence of In-In bonding or In-Ti and In-Nb antibonding features for the successive low energy eigenvalues are related with the system's instability. This effect may not only alter the decreasing trend of the Young's modulus, but may result in enhancement of the material's rigidity.

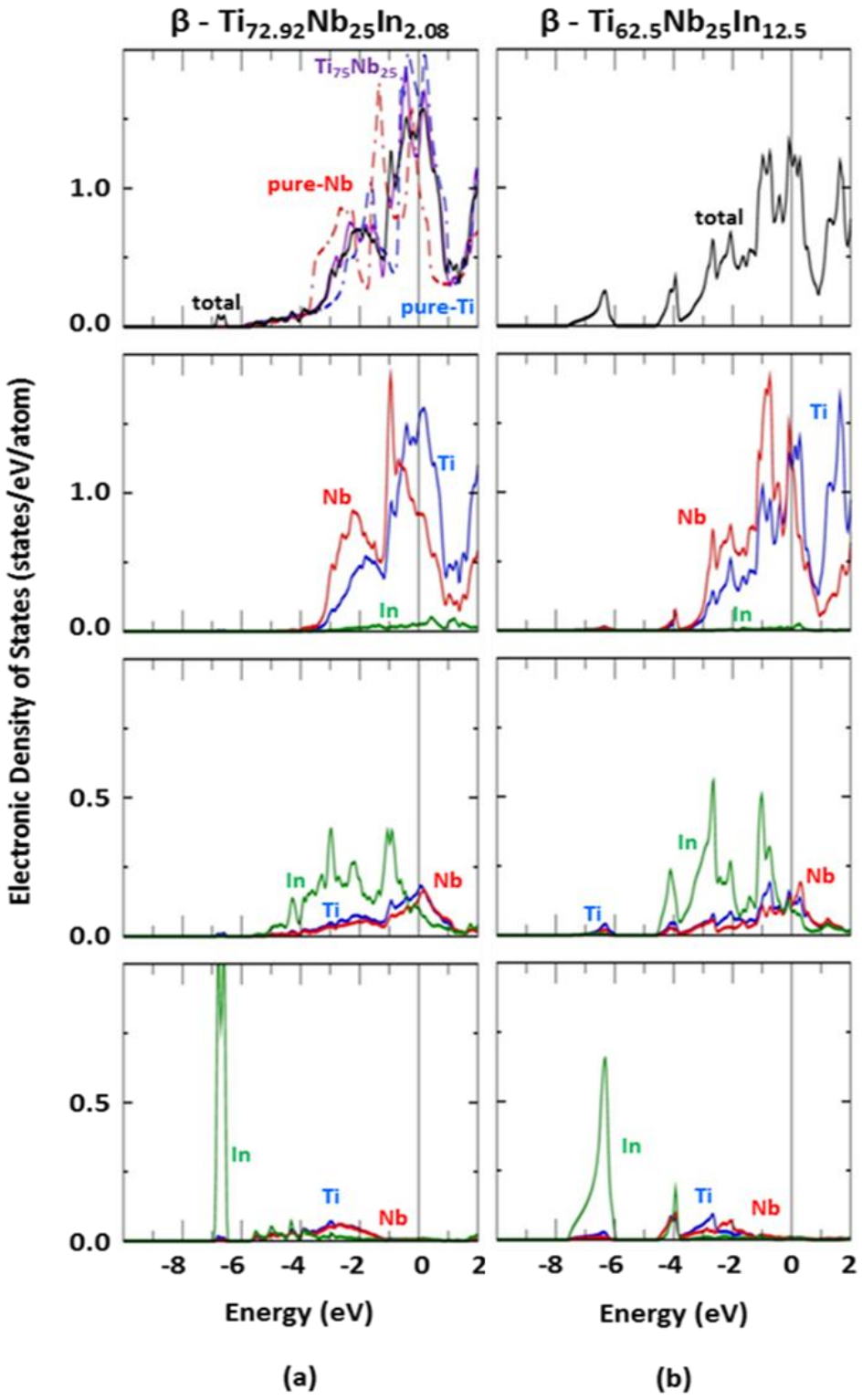

Figure 3.3.3 *Electronic density of states of β-phase:* **a)** *pure Ti, pure Nb, Ti-25at%Nb and Ti-25at%Nb-2.08at%In (dotted blue, dotted red, purple and black lines, respectively) for the total, d, p and s contributions (first up to fourth row, respectively) while* **b)** *stands for Ti-25at%Nb-12.5at%In.*

From the EDOSs of the low In compositions (Ti-25at%Nb-(x ≤ 2.87)at%In) the electronic band energy (E_b) has been calculated for different indium's atomic environments. In line with the total energy results, the calculated E_b shows different values depending on the In's first neighbourhood.

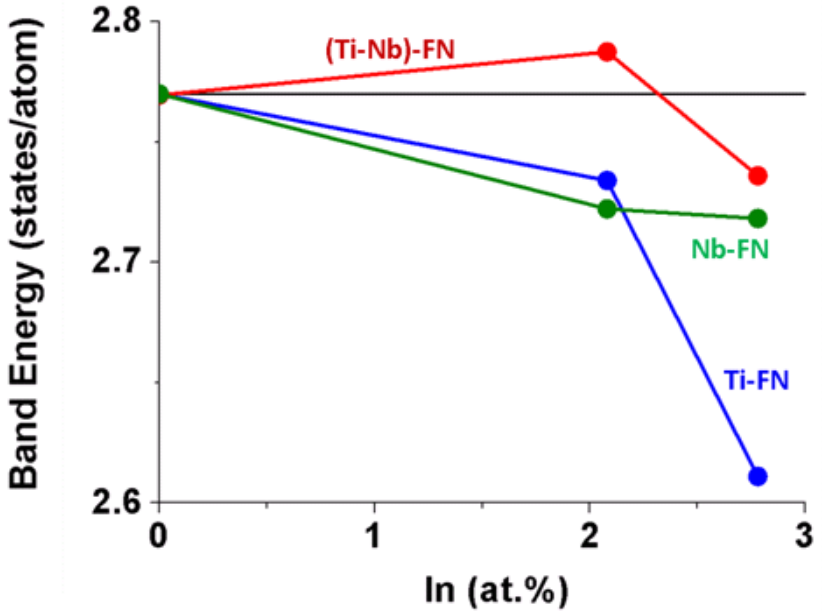

Figure 3.3.4 *Band Energy of Ti-25at%Nb, Ti-25at%Nb-2.08at%In and Ti-25at%Nb-2.78at%In for the Ti-FN (blue), Nb-FN (green) and the mixed TiNb-FN (red) atomic environments. ΔE of binary composition (black line) is set as the reference level. In the inset, the Ti-FN energetically favoured atomic configuration is shown; where grey, yellow and magenta balls correspond to Ti, Nb and In atoms.*

Taken into account that the system's band energy has been related with the crystal stability [6], the influence of In additions on the band energy data for different atomic environments and In amounts were analysed. In Figure 3.3.4 we present the band energy for the binary β-TiNb system (dashed line) along with the ternary for the Ti-FN and mixed TiNb-FN environments for comparison reasons. In particular, for the Ti-25at%Nb-2.08%In case, the mixed TiNb-FN is slightly higher (2%) than that of the binary Ti-25at%Nb system (black line) suggesting that in this atomic environment In may act as supplementary β-phase stabilizer along with Nb while for the Ti-FN environment the opposite is true. For the higher In-content alloy (Ti-25at%Nb-2.78at%In), the E_b value is up to 4% lower for all environments than in the binary case, suggesting a β-phase destabilizing effect.

c) Mechanical properties

In order to validate our theoretical predictions and to further study the mechanical properties, several β-type (Ti-40wt%Nb)-xIn alloys were produced by cold-crucible casting and room temperature mechanical tests were performed by the IFW colleagues in Dresden. The measurements revealed that by 5 wt% In additions to the binary Ti-40Nb alloy a reduction of the Young's modulus from 69GPa to 49GPa was obtained, together with a change of the ultimate fracture strength of from 1421MPa to 775MPa, large plastic strains above 20% and a remarkable strain hardening. In the same way with Sn, minor additions of indium are effective in lowering the Young's modulus of Ti-25at%Nb, improving their biomechanical compatibility. Concluding, the computational and experimental results suggested a twofold effect of indium in decreasing the Young's modulus: a) On one side, In atoms soften the bcc phase crystal lattice by expanding its unit cell volume and b) on the other side, In introduces low energy antibonding states that weaken the bonding character of the binary system.

3.3.4 Conclusions

In this chapter, the theoretical data on the β-Ti-25at%Nb-xIn ($x \leq 25$at%) were studied and compared with the experimental results on the Ti~25at%Nb-xIn ($x < 3$at%) alloys which have been designed and casted for the first time. The analysis of the XRD patterns found that all studied alloys completely retain the β-phase in the quenched condition. The ab initio calculations found an increase trend of the lattice constants upon In substitution, while the experimental lattice parameters calculated from the XRD follow the same behaviour. This may be due to the larger atomic radius of In compared to that of Ti and Nb. Furthermore binding energy calculations were used to reveal the preference of a particular structure against another one. The results predict a destabilization of the bcc upon indium content, which depends also on atomic environments. The calculated total energy showed that the indium atom always prefers the Ti-first neighbourhood (Ti-FN), while the Nb-FN and Ti-Nb-FN environments are less energetically favoured especially for the Ti-25at%Nb-2.78at%In composition.

The electronic density of states revealed that the lowest energy states between -6.5 eV and -7 eV of Ti-25at%Nb-($x \leq 8.33$at%)In are mainly due to In *s*-electrons while the In *p*-electrons are responsible for the states at energies above -5eV. Nevertheless, the main contribution at the Fermi level is due to Ti *d*-electrons. In addition, the β-phase Ti-

25at%Nb-(x ≥ 12.5at%)In is energetically unfavoured compared to the lower In content compositions. The alterations of the chemical bonding due to the In atoms presence were also investigated though the investigation of the wavefunction at selective energies [9]. The results revealed the presence of In-5s with Ti-4s or Nb-5s antibonding low energy states introduced in the In neighbourhood that weaken the bonding character of the Ti-25at%Nb, showing for the first time the alterations in the nature of the atomic bonding due to In additions and explaining the ternary's lower values of the Young's modulus. At higher In contents (>> 3at%In), first and second neighbourhood include In-In pairs that exhibit strong σ bonding features, thus increasing the Young's moduli and inducing instability in the system.

Moreover, it was experimentally measured that the addition of 5.2wt% indium to Ti–40wt%Nb expands the bcc lattice parameter lowering at the same time the Young's modulus from E = 69GPa to E = 49GPa. The Young's modulus of (Ti-40wt%Nb)-5wt%In (and Ti-24.9at%Nb-2.7at%In) is much lower compared to other commercial alloys like Ti-6Al-4V (E = 112GPa) and rather close to that of a bone (< 30GPa), thus helping to overcome the stress shielding effect. These findings suggest that the elastic softening of β-Ti-25at%Nb by indium additions may be due to the lattice expansion induced by the indium addition and most importantly due to the presence of antibonding low energy electron states between In neighbouring atoms that weaken the chemical bonds. Summarizing, we can conclude that since Ti-Nb-In alloys satisfy all the non-toxicity and mechanical biocompatibility conditions they could be characterized as promising candidates for the development of orthopaedical implants.

3.3.5 References

1. K. Anderko. The Binary Systems of Titanium with Gallium, Indium, Germanium and of Zirconium with Gallium and Indium. Zeitschrift fur Metallkunde 49, (1958) 165-172.
2. L.D. Gulay, J.C. Schuster. Investigation of the titanium–indium system. Journal of Alloys and Compounds 360 (2003) 137-142.
3. P. Blaha, K. Schwarz, G. K. H. Madsen, D. Kuasnicka, J. Luitz, WIEN2k, Augmented Plane Wave Local Orbitals Program for Calculating Crystal Properties, Vienna University of Technology, Vienna, 2001.
4. J.P. Perdew, K. Burke, M. Ernzerhoff, Generalized Gradient Approximation Made Simple. Physics Review Letters 77 (1996) 3865-3868.
5. F.D. Murnaghan. The Compressibility of Media under Extreme Pressures. Proceedings of the National Academy of Sciences of the United States of America 30 (9) (1944) 244–247
6. P. Soderlind, O. Eriksson, J.M. Wills, A.M. Boring. Theory of elastic constants of cubic transition metals and alloys. Physical Review B 48 (1993) 5844-5851.
7. M. Abdel-Hady Gepreel, M. Niinomi. Biocompatibility of Ti-alloys for long-term implantation. Journal of the Mechanical Behavior of Biomedical Materials 20, (2013) 407–415.
8. R.A. Young. The Rietveld Method. Oxford University Press, (1993) Oxford, UK.
9. M. Calin, A. Helth, J. Julio Gutiérrez Moreno, M. Boenisch, V. Brackmann, L. Giebeler, T. Gemming, Ch.E. Lekka, A. Gebert, R. Schnettler, J. Eckert. Elastic softeningof β-type Ti–Nb alloys by indium (In) additions. Journal of Mechanical Behavior of Biomedical materials 39 (2014) 162 – 174.
10. S. Nag, Y. Zheng, R.E.A. Williams, A. Devaraj, A. Boyne, Y. Wang, P.C. Collins, G.B. Viswanathan, J.S. Tiley, B.C. Muddle, R. Banerjee, H.L. Fraser. Non-classical homogeneous precipitation mediated by compositional fluctuations in titanium alloys, Acta Materialia 60 (2012) 6247–6256.
11. A. Devaraj, S. Nag, R. Srinivasan, R.E.A. Williams, S. Banerjee, H.L. Fraser. Experimental evidence of concurrent compositional and structural instabilities leading to ω precipitation in titanium-molybdenum alloys. Acta Materialia 60 (2012) 596-609.

12. J.J. Gutiérrez-Moreno, Y. Guo, K. Georgarakis, A.R. Yavari, G.A. Evangelakis,Ch.E. Lekka. The role of Sn doping in the β-type Ti-25at%Nb alloys: experiment and ab initio calculations. Journal of Alloys and Compounds 615 (2014) S676–S679.

3.4 Ti-Nb-Sn alloys

3.4.1 Introduction

The β-TiNbSn ternary alloys are very promising materials for orthopaedic applications due to their biocompatibility and their lower Young's moduli (40GPa) [1-5] compared to both Ti and Ti-Nb alloys [6-14]. Their reduced rigidity is attributed to the β-phase stabilization that is related to Nb and Sn compositions. In particular, in the binary Ti-Nb case, this structure becomes dominant among the other phases, i.e. α, ω and α″, at Nb composition of 25at% [2, 13]. The presence of the ω-phase is considered responsible for the increase of the Young's modulus in these alloys [2] due to the ω particles that are present in the Ti-25at%Nb [7, 13, 15]. Interestingly, the presence of Sn is experimentally suggested to suppresses this ω-formation [2, 3, 16] for the Ti-Nb based [2, 3] alloys as well as in the Ti-Mo and Ti-V based alloys [2, 16]. In previous studies [2, 3], it was found that depending on the heat treatment, the static Young's moduli of the β-(Ti-35wt%Nb)-4wt%Sn could reach 43GPa, while for higher Sn content, i.e. the β-(Ti-35wt%Nb)-7.9wt%Sn, although the β-phase was more easily obtained the mechanical properties were not significantly improved. It turns out therefore that the presence of Sn may alter the structure and the properties of these alloys. However, the role of Sn into the Ti-Nb binary systems is not identified, while a systematic study of β-TiNbSn alloys with increasing Sn contents, although interesting, is still lacking. The ab initio calculations were compared with the experimental results on the Ti-25.05at%Nb-2.04at%Sn alloy. To this end, in this chapter the β-Ti-25at%Nb-xSn ($x \leq 25$at%) alloys are studied by LAPW-DFT calculations and the corresponding structural and electronic properties were evaluated for various Sn substitutions. The ab initio calculations were compared with experimental results of the Ti-25.05at%Nb-2.04at%Sn alloy rods synthesized at INP Grenoble [1].

3.4.3 Results and discussion

a) Structural and mechanical properties

In Figure 3.4.1(a), the X-ray diffraction patterns (XRD) of Ti-25.05at%Nb-2.04at%Sn together with the simulated β-Ti-25at%Nb-2.08at%Sn powder diffraction pattern is depicted using the crystal features from the ab initio unit cell. From the experimental XRD, only the peaks which correspond to the β phase are identified, while no sign of

the ω-phase is observed. In line with the bulk Ti-based alloys, the highest intensity first peak corresponds to the (110) preferred orientation. That peak refers to the first textured preferred growth direction. It is interesting to notice that despite the limitations of the single phase monocrystalline matrix of the ab initio calculations, as well as the "powder" approximation of the VESTA software, there is an overall agreement between the experimental and the theoretical XRD diffraction data. In particular, in the inset of Figure 3.4.1(a) although the first XRD experimental peak is wider than the theoretical one, the corresponding angles of the main peak are almost the same. Finally, both the theoretical and the experimental relative distances between the XRD peaks are comparable.

In Figure 3.4.1(b), the lattice constants which were obtained by the ab initio computations (filled circles) are depicted along with the available experimental data from the XRD measurements (open circles). Interestingly, although the theoretical values are lower than the experimental ones, they both follow the same slope. The differences in the lattice constants' absolute values are attributed to the small periodic unit cells and to the zero pressure and temperature calculations compared to the experimental data of the polycrystalline alloys which were measured at room temperature. As have been commented in the computational details section, for the design of the unit cell, several different atomic configurations were used, in which the distributions of the Nb atoms and their short range Sn neighbourhood were systematically tested. The calculated total energy shows different values depending on the Sn's first neighbourhood (FN), where a lower energy indicates a more energetically favoured configuration. The results show that Sn prefers the Ti first neighbourhood (Ti-FF) against Sn and Nb (Nb-FF). The inset in Figure 3.4.1(b) shows a schematic representation of the energetically favoured conformation of β-Ti-25at%Nb-2.08at%Sn, were blue and green balls stand for Ti and Sn atoms, respectively. From all atomic configurations, the energetically favoured were chosen for further studies.

Furthermore from the ab initio total energy curves the bulk modulus (B) was calculated for all cases. The results of the B for several Sn substitutions in the Ti-Nb matrix are shown in Table 3.4.1. We found that upon Sn substitutions the B values are slightly increasing from 119GPa (2.08at%) to 127GPa for the maximum Sn concentration 25at%.

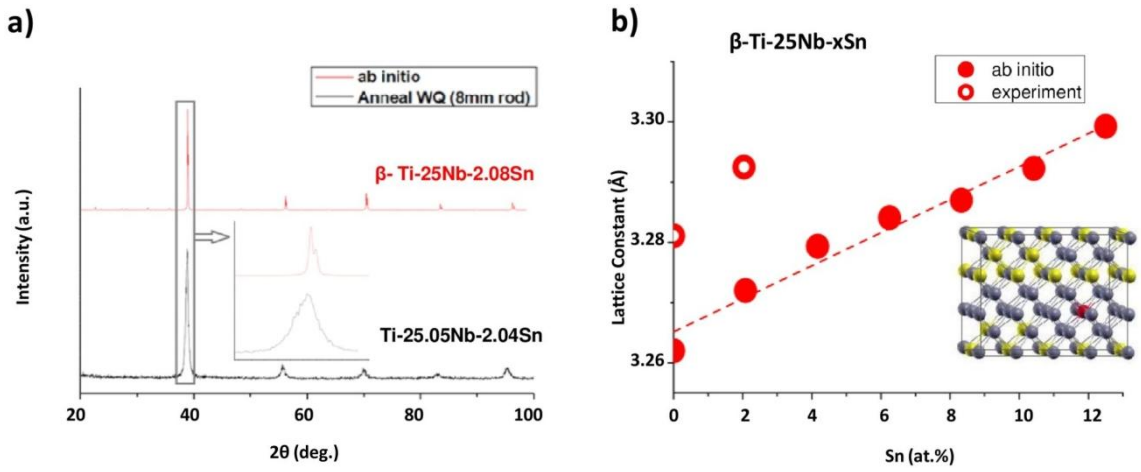

Figure 3.4.1 a) *The conventional Cu kα X-ray diffraction pattern of experimentally prepared Ti-25.05at%Nb-2.04at%Sn alloy compared with the X-ray diffraction pattern of Ti-25at%Nb- 2.08at%Sn alloy simulated with VESTA simulation package based on the β unit cell of the ab initio calculations.* **b)** *β-Ti-25at%Nb-xSn lattice constants varying with Sn substitution. Filled and open circles correspond to ab initio and experimental data, respectively. Inset shows a schematic representation of the energetically favoured conformation of β-Ti-25at%Nb-2.08at%Sn. Blue and green balls stand for Ti and Sn atoms, respectively.*

Sn (at%)	B (GPa)
0.00	120
2.08	119
4.17	122
6.25	123
12.50	127
25.00	127

Table 3.4.1 *Bulk modulus of β-Ti-25at%Nb-xSn alloys upon Sn addition.*

b) Electronic properties

Aiming in obtaining insight on the role of Sn in the Ti-Nb alloys for both β and ω phases we evaluated the Electronic Density of States (EDOS) of β-Ti-25at%Nb-xSn, x = 2.08 and 12.5at% (Figure 3.4.2), ω-Ti-25.93at%Nb-1.85at%Sn and ω-Ti-25at%Nb-2.78at%Sn (Figure 3.4.3) ternary alloys. The EDOS of pure Ti and Nb as well as Ti-25at%Nb EDOS have been also included for comparison reasons. Starting with the pure

β-Ti EDOS, we observe two main electron bands located around -2eV and at the Fermi level (E_F) separated by a minimum at -1eV. Close to E_F a local minimum at +0.1eV is found between the highest occupied state (around -0.5eV) and the first unoccupied one (at 0.25eV) that persists in the binary Ti-25at%Nb and ternary Ti-25at%Nb-(x ≤ 6.25)at%Sn cases. The pure β -Nb EDOS exhibits a low energy band around -2.5eV, while the next one is located far from E_F, denoting higher stability of the Nb β-phase compared to the previous cases.

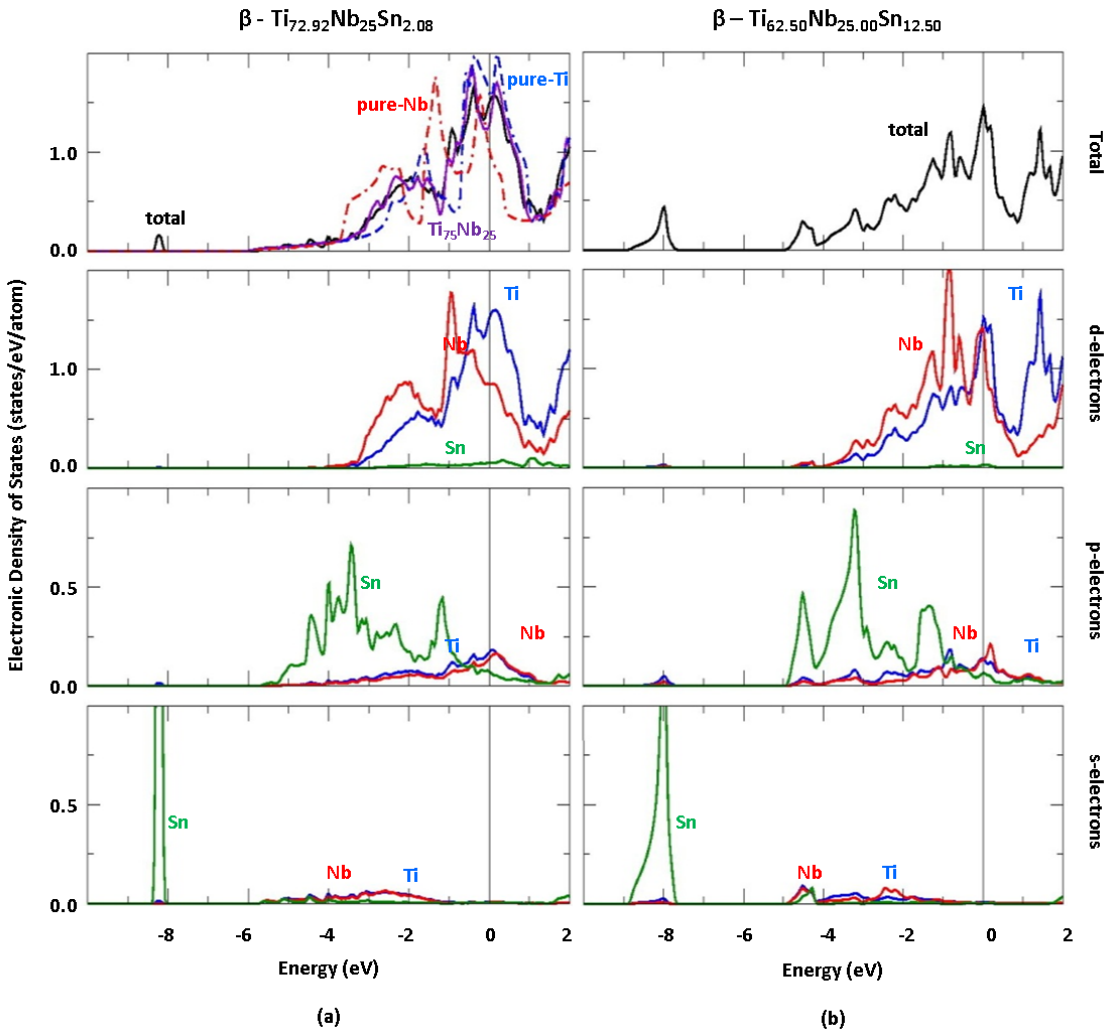

Figure 3.4.2 *Electronic density of states of β-phase:* **a)** *pure Ti, pure Nb, Ti-25at%Nb and Ti-25at%Nb-2.08at%Sn (dotted blue, dotted red, purple and black lines, respectively) for the total, d, p and s contributions (first up to fourth row, respectively) while* **b)** *stands for Ti-25at%Nb-12.5at%Sn.*

Regarding the pure ω-Ti EDOS, we observe at E_F a minimum with much lower occupation that the β-Ti which is within the highest occupied state (around -0.3eV) and the first unoccupied one (at 0.2eV) revealing the stability of this phase. Concerning the

ω-phase of the Ti-25at%Nb and the Ti-25.93at%Nb-1.85at%Sn, the enhancement of the occupation at E_F renders the ω structure of these alloys less stable compared to the pure Ti ω–phase. This change is more visible in ω-Ti-25at%Nb-2.78at%Sn, suggesting that the ω–phase of Ti-25at%Nb and Ti-25at%Nb-xSn as unfavoured, in comparison with the β-phase, in line with experimental results [2-5, 16]. The presence of Sn introduces a low energy state at -8.2eV in both phases, while slight depletion is found at the Fermi level without altering significantly the characteristics of the binary β-phase's EDOS.

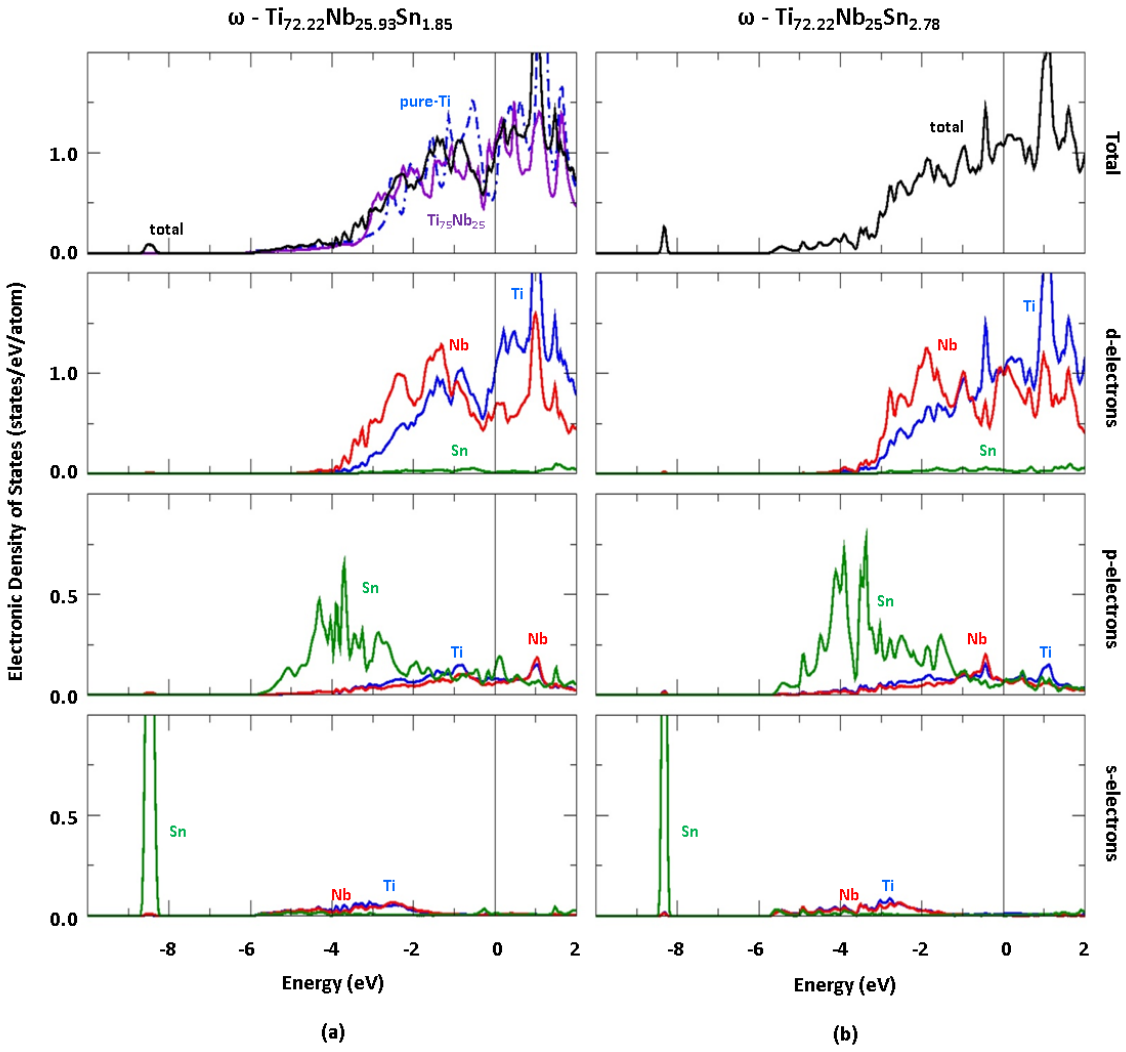

Figure 3.4.3 *Electronic density of states the ω-phase:* **a)** *pure Ti, Ti-25at%Nb and Ti-25.93at%Nb-1.85at%Sn (dashed blue, purple and black lines, respectively) for the total, d, p and s contributions (first up to fourth row, respectively),* **b)** *stand for the cases of Ti-25at%Nb-2.78at%Sn.*

In the β-Ti-25at%Nb-(x ≤ 6.25)at%Sn total EDOS, the energy states are depleted at E_F, causing an almost equivalent occupancy from -1eV up to 1eV, while no difference is found between the three Sn compositions at the lower energy states close to -8eV. On

the contrary, in Ti-25at%Nb-12.5at%Sn the EDOS exhibits a peak at E_F and a general reduced occupancy in the occupied states denoting instability of the β-phase for this composition [21]. In the case of the highest Sn content (25at%) the EDOS exhibits a deep minimum around 0.3eV and a decreasing occupancy trend from the occupied to the unoccupied states, denoting instability of the β-phase for this composition. Nevertheless, the energy states around -1eV and -2eV are also importantly depleted, while small filling of the EDOS is found in the broad energy band from -10eV up to -7eV and around -4eV. These variations suggest that the β-phase of both Ti-25at%Nb-12.5at%Sn and Ti-25at%Nb-25at%Sn are energetically unfavoured compared to Ti-25at%Nb-($x \leq 6.25$)at%Sn cases [21]. It worth's to be noted that the alterations at E_F are due to the relative compositional changes upon Sn substitutions and the enhancement of Ti content. This is illustrated in the calculated partial *s, p* and *d* EDOSs, Figure 3.4.2 and Figure 3.4.3, where the *d*-electron EDOS is absolute due to contributions of Nb and Ti atoms. Similar behavior is found for the ω-phase partial EDOS, where the *d*-electrons contributions are mainly due to the Nb and Ti atoms. In particular, the peaks located at -1eV and at +1eV show the *d*-Ti-Nb hybridization, while the states between -1eV and -4eV are mainly due to Nb *d*-electrons contribution. In analogy to β-phase, Sn atoms are dominant in the *s* and *p* partial EDOSs and basically in the lowest energy states. The majority of the *p*-electron occupation in the EDOS is located between -3eV and -5eV, while the high peak at -8.2eV is due to *s*-electrons. Regarding the β-phase partial EDOS of the smallest Sn compositions ($x \leq 6.25$)at%Sn, the *d*-electron EDOS are similarly to the high Sn compositions mainly due to Nb and Ti atoms having the Ti mainly responsible for the EDOS features at E_F. The states below -0.8eV are mainly due to Nb, while the peak around -1eV denotes hybridization between Nb and Ti *d*-electrons. Sn atoms are dominant in the *s* and *p* partial EDOSs and the lowest energy states. A broad band energy from -1eV down to -6eV characterizes the *p*-electron EDOS, while the states from -7eV till -9eV are due to *s*-electrons. Interestingly, in the Sn rich stoichiometries, 12.5at% and 25at% Sn, the Sn and Nb atoms may become first neighbours which results the appearance of Nb *d*-electron in the highest energy bands due to the Nb*4d*-Sn*5p* hybridizations. Nevertheless, for all cases, the Sn contributions are dominant in the *s* and *p* partial EDOSs. In particular, a broad band energy from -1eV down to -6eV characterizes the *p*-electron EDOS, while the states from -7eV down to -9eV are due to *s*-electrons. These findings suggest that the Sn substitutions influence

mainly the low energy states, while the states around E_F may be affected by the Sn-Ti and Sn-Nb hybridizations.

Figure 3.4.4 depicts the β-Ti-25at%Nb band structure compared to the β-Ti-25at%Nb-2.08at%Sn, which is the ternary alloy with the minimum addition of Sn (1/48 atoms). As we observed in the EDOS, the main Sn contribution (denoted with green light circles) is situated around -8.2eV and is almost equally distributed along all the k-points directions.

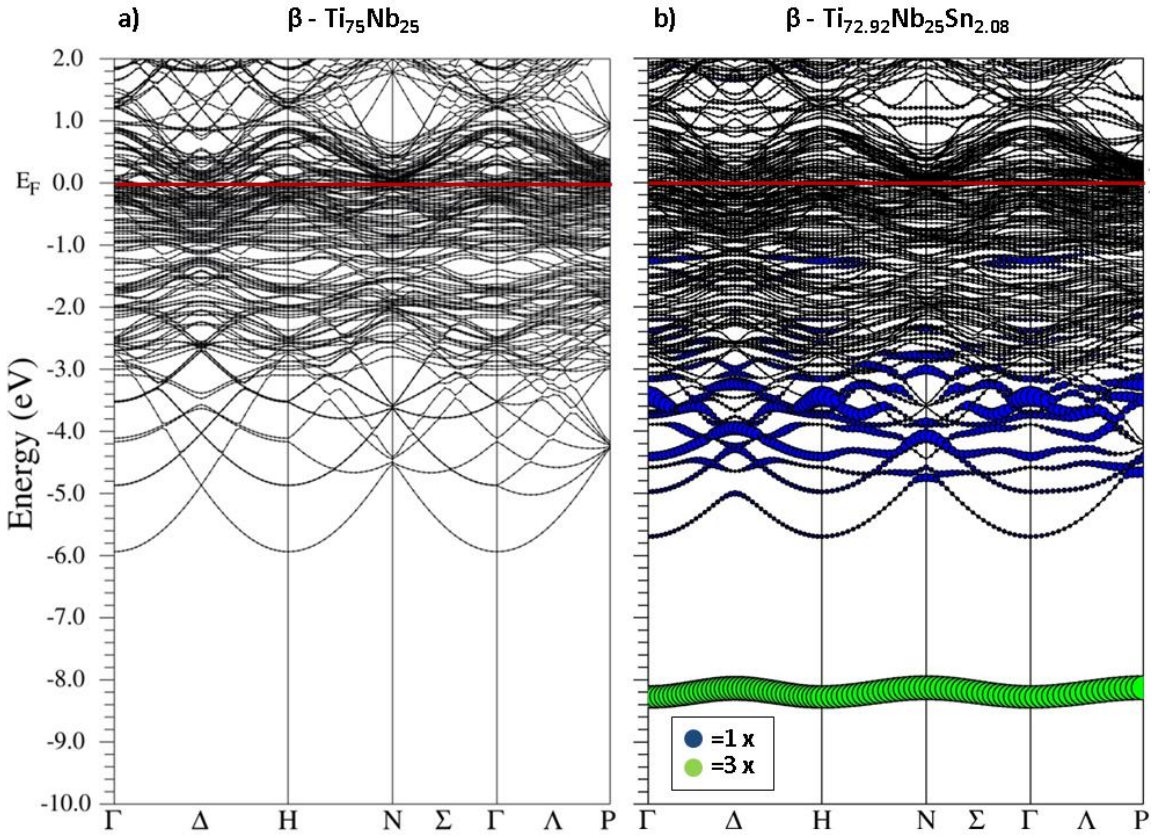

Figure 3.4.4 *Band structure of β-phase:* **a)** *Ti-25at%Nb and* **b)** *Ti-25at%-2.08at%Sn. The diameter of the colored circles represents the presence of Sn states, the contribution drawn in green has a weight of three time the blue circles.*

The Sn contribution is also visible in the bands located between -2.5eV and -5eV as well as around -1eV (blue dark circles). Not that the scale used gives to the green circles a value of 3 times the blue, denoting the higher weight of the lowest energy states.

In order to investigate the possibility of bonding hybridizations between the dopant and the Ti-Nb matrix, several the electron states were further analysed [21]. The findings suggested that relatively low Sn substitutions may reduce the system's rigidity (by

means of local antibonding sites), while high Sn content results in significant deterioration of the periodic symmetry of the electronic charge that may lead to mechanical instability.

3.4.4 Conclusions

In this chapter, the computational simulations correlated with experiments on the β and ω crystallographic structures of TiNbSn alloys were presented. From the XRD measurements an almost linear increase of the lattice constants upon Sn substitution was found, while although underestimated the ab-initio values follow the experimental behavior. The electronic density of states revealed that the 25at%Sn β-phase is energetically unfavoured compared to the 2.08at% and 6.25at% substitutions, while the binary and ternary ω-phase compositions are unfavoured compared to pure Ti. In both phases, Sn *s*-electrons are responsible for the lowest energy states around -8eV, the Sn *p*-electrons are located at energies below -3eV, while Ti *d*-electrons contribute mainly at the Fermi level. In addition, it came out that relatively low Sn substitutions result in local antibonding sites, while high Sn contents lead to significant modifications of the electronic charge symmetry and may head to mechanical instability. Regarding the study of the mechanical properties, it was found that the bulk modulus slightly increases upon Sn substitutions. These results could be used for the design of β-Ti-based alloys with non-toxic additions, suitable for orthopedic applications.

3.4.5 References

1. Y.Guo, K.Georgarakis, Y.Yokoyama, A.R.Yavari. On the mechanical properties of TiNb based alloys. Journal of Alloys and Compounds 571 (2013) 25–30.
2. T. Ozaki, H. Matsumoto, S. Watanabe and S. Hanada. Beta Ti Alloys with Low Young's Modulus. Materials Transactions 45 (2004) 2776-2779.
3. H. Matsumoto, S. Watanabe, S. Hanada. Effect of Deformation-Induced ω Phase on the Mechanical Properties of Metastable β-Type Ti-V Alloys. Materials Transactions 46 (2005) 1070-1078.
4. Taek-Kyun Jung, Satoshi Semboshi, Naoya Masahashi, Shuji Hanada. Mechanical properties and microstructures of β Ti–25Nb–11Sn ternary alloy for biomedical applications Materials Science and Engineering C 33 (2013) 1629–1635.
5. Hiroaki Matsumoto, Sadao Watanabe, Shuji Hanada. Beta TiNbSn Alloys with Low Young's Modulus and High Strength. Materials Transactions, Vol. 46 No. 5 (2005) 1070-1078.
6. C. M. Lee, C. P. Ju, J. H. Chern Lin. Structure–property relationship of cast Ti–Nb alloys. Journal of Oral Rehabilitation 29 (2002) 314-322.
7. D. L. Moffat, U.R. Kattner. Metallurgical and Materials Transactions A 19 (1998) 2389.
8. D.L. Moffat, U.R. Kattner. The stable and metastable Ti-Nb phase diagrams. Metallurgical Transactions A. Volume 19, Issue 10 (1998) 2389-2397.
9. E. W. Collings, Physical Metallurgy of Titanium Alloys American Society of Metals. Materials Park, Columbus (1984).
10. R. Boyer, G. Welsch, E.W. Collings, Materials Properties Handbook: Titanium Alloys. ASM International, Materials Park (1994).
11. R. Hermann, H. Hermann, M. Calin, B. Büchnera, J. Eckert. Elastic constants of single crystalline beta-Ti70Nb30. Scripta Materialia 66 (2012) 198-201.
12. S. Banumathy, R. K. Mandal, A. K. Singh. Structure of orthorhombic martensitic phase in binary Ti–Nb alloys. Journal of Applied Physics 106 (2009) 093518.
13. D. Kuroda, M. Niinomi, H. Fukui, M. Morinaga, A. Suzuki, J. Hasegawa. Tensile properties and cyto-toxicity of new biomedical beta-type titanium alloys. Tetsu to Hagane - Journal of the iron and steel institute of Japan. 86 (9), (2000) 602-609.

14. H.Y. Kim, Y. Ekehara, J.I. Kim, H. Hosoda, S. Miyazaki. Martensitic transformation, shape memory effect and superelasticity of Ti–Nb binary alloys. Acta Materialia, Volume 54, Issue 9 (2006) 2419-2429.
15. A.I. Mardare, A. Savanb, A. Ludwigb, A. D. Wieckb, A. W. Hasselet. High-throughput synthesis and characterization of anodic oxides on Nb–Ti alloys. Electrochimica Acta 54 (2009) 5973–5980.
16. Y.H. Hon, J.Y. Wang, Y.N. Pan. Composition/Phase Structure and Properties of Titanium-Niobium Alloys. Materials Transactions 44 (2003) 2384-2390.
17. J.C. Williams, B.S. Hickman, D.H. Leslie. The effect of ternary additions on the decomposition of metastable β-phase titanium alloys. Metallurgical and Materials Transactions A2 (1971) 477-484.
18. P. Blaha, K. Schwarz, G. K. H. Madsen, D. Kuasnicka, J. Luitz. WIEN2K, Augmented Plane Wave Local Orbitals Program for Calculating Crystal Properties. Vienna University of Technology, Vienna, Austria (2001).
19. J. P. Perdew, K. Burke, and M. Ernzerhof. Generalized Gradient Approximation Made Simple. Physical Review Letters 77 (1996) 3865.
20. K. Momma and F. Izumi, VESTA 3 for three-dimensional visualization of crystal, volumetric and morphology data, Journal of Applied Crystallography 44 (2011) 1272-1276.
21. P. Soederlind, O. Eriksson, J.M. Wills, A.M. Boring. Theory of elastic constants of cubic transition metals and alloys. Physical Review B 48 (1993) 5844.
13. J.J. Gutierrez-Moreno, Y. Guo, K. Georgarakis, A.R. Yavari, G.A. Evangelakis, Ch.E. Lekka. The role of Sn doping in the β-type Ti-25at%Nb alloys: experiment and ab initio calculations. Journal of Alloys and Compounds 615 (2014) S676–S679.

3.5 Ti-Zr-Hf alloys

3.5.1 Introduction

Zr and Hf are known to show very similar physical and chemical properties with Ti since they belong to the IVa group of the periodic table. Ti-alloys containing Zr have demonstrated two basic characteristics desirable for the development of a new generation of Ti-based alloys for orthopaedics: a) their mechanical strength is up to 2.5 times higher than the strength of commercial pure Ti, [1] and b) they present higher resistance to corrosion in biological fluids in comparison with the pure Ti [2-4]. Another advantage of the Ti-Zr alloys is their enhanced osseointegration compared to Ti implants most probably due to their α-phase, while the improved biocompatibility versus Ti has been established [5, 6]. Moreover Zr-based alloys having biocompatible elements, as the β-phase Zr–12Mo–xTi alloys exhibit high compressive and yield strength, high elastic energy, enhance plastic strain and low Young's modulus (32–35GPa) [7]. Furthermore, Hf has been suggested as an element which has the potential to improve the mechanical properties of Ti alloys. In fact Ti–Hf alloys exhibit lamellar hcp martensite (α′) structure, while the increase of Hf content (up to 40at%) can gently reduce the dynamic Young's modulus and strongly enhance the strength of Ti–Hf alloys [8-10]. Moreover, it is proved that Ti and Hf exhibit good biocompatibility and osteoconductivity [11]. Therefore, Ti alloys with Zr and Hf additions, may improve the mechanical properties and reveal better corrosion resistance and biocompatibility compared to Ti [12]. As an example, Ti-20at%Zr-20at%Hf-20at%Fe alloy is found to be harder, showing lower Young's modulus and better corrosion resistance than Ti–6Al–4V, while it also exhibits non-cytotoxicity characteristics [13]. Synthesized Ti–Zr, Ti–Hf, and Zr–Hf binary and Ti–Zr–Hf ternaries alloys are mainly stabilized in the α-phase, while ω-phase contributions persist at certain compositions [14-16]. Moreover previous studies regarding the ternary Ti-Nb-Hf alloys, detected the presence of ω-phase for Ti concentrations between 34at% and 60at% [17-19]. For this section we scaled-up from DFT to molecular dynamics simulations. Classical molecular dynamics simulations allow us to use larger and therefore more realistic systems. In addition MD allow us to perform time and temperature dependent simulations, in contrast to DFT where we work at constant T = 0K. Although it is interesting to simulate the properties of Ti-Zr-Hf systems using large scale simulations, such more realistic cases are still

lacking, due to the absence of the corresponding interatomic potentials. Therefore an interatomic potential was developed and molecular dynamics simulations were performed in order to study how the structural properties are related with the Hf or Zr alloying elements along with the Young's modulus.

3.5.2 Results and discussion

We performed large scale molecular dynamics simulations on Ti, Ti-25at%Zr, Ti-25at%Hf and Ti-12.5at%Zr-12.5at%Hf alloys. Starting from the α phase where the doping atoms were randomly placed, we carefully melted at 3000K and subsequently quenched the system to 300K, while after equilibrium at room temperature we applied tensile deformation. Since the final structure of the system is strongly related with the quenching ratio, we tested different ratios with the aim of creating different structures, including single-crystal and polycrystalline systems. The radial distribution function (Figure 3.5.1) seems to indicate a disordered polycrystalline structure for all alloys when the system is rapidly quenched at 10K/ps. On the other hand, when the system is quenched at lower ratios (up to 0.1K/ps) the final structure results in mono-crystalline system (single grain) with random orientation suggesting that the same calculation for a larger system could form a polycrystalline system.

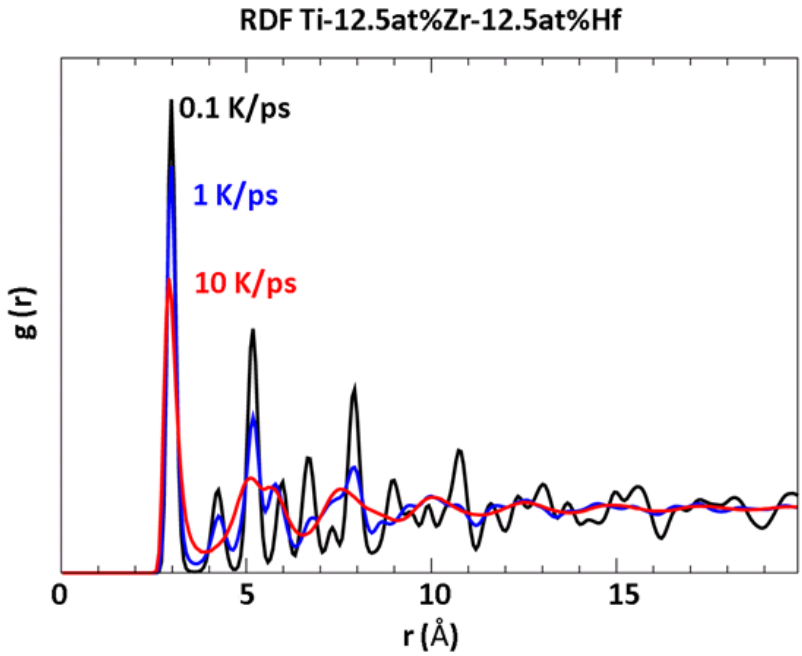

Figure 3.5.1 *Radial distributions function versus interatomic distance of Ti-12.5at%Zr-12.5at%Hf. The atoms have been relaxed at 300K after quenching by different ratios: 10 K/ps (red line), 1 K/ps (blue line) and 0.1 K/ps (black line).*

In Figure 3.5.2(b) the stress versus strain curves of pure Ti and different alloys are depicted. For all compositions studied, the stress-strain curves of the alloys are below the monocrystalline α-Ti hcp curve that was expanded along the [0100] direction. It is important to note that as an hcp single-crystal, the Young's modulus of Ti is highly dependented on the crystallographic direction. Due to that reason, the system was deformed along a chosen direction where a mean value of the Young's modulus is found. As it is depicted in the Table 3.5.2, the calculated Young's moduli predict higher elasticity, around 64GPa, for all the binary and ternary alloys quenched at 10K/ps compared to the monocrystalline Ti metal while interestingly this elastic modulus does not depent on the alloys' stoichiometry.

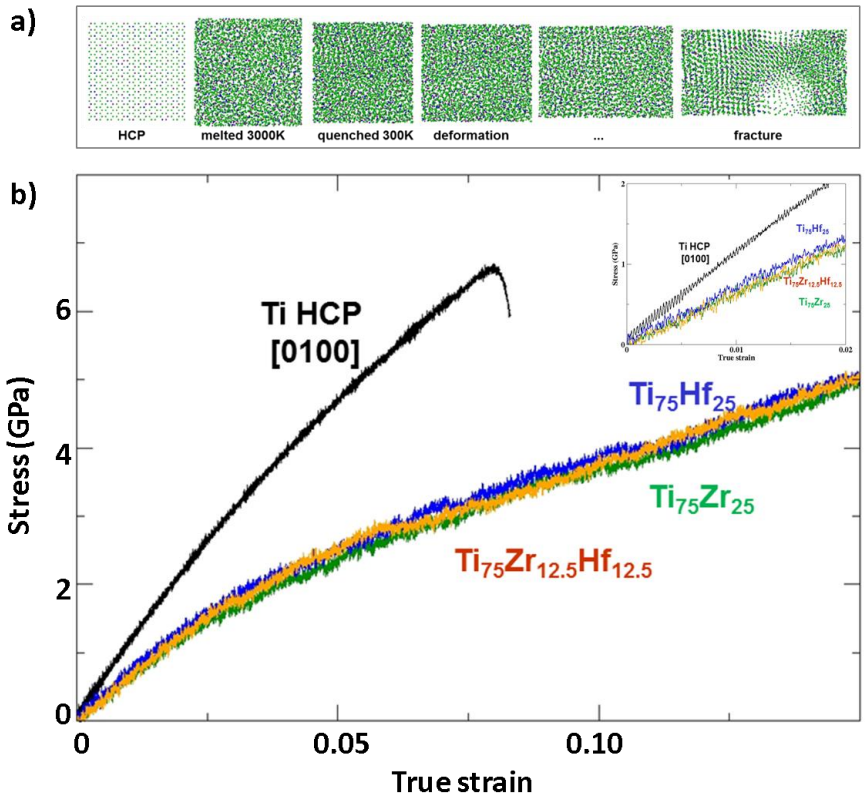

Figure 3.5.2 a) *Schematic representation of Ti-12.5at%Zr-12.5at%Hf system: hcp initial structure, melting at 3000K, quenching to 300K at 10K/ps and upon tensile deformation.* **b)** *Stress – strain curves of the Ti hcp along [0100] direction and the Ti-25at%Zr, Ti-25at%Hf and Ti-12.5at%Zr-12.5at%Hf alloys. Along we the calculated Young's moduli by a linear fitting of the elastic region, showed in the inset.*

Moreover in these cases, the elastic modulus values do not independent on the direction along which the strain is performed, due to the polycrystalline structure of these systems. The results of this chapter reveal the importance of the Ti-Zr-Hf systems towards the design of a biocompatible low Young's moduli alloy, that although present

higher modulus values compared to β-TiNb alloys, they could be of use for the design of novel alloys suitable for biomedical applications. Nevertheless, in order to acquire concluding results, more calculations having several stoichiometries in larger systems and slowly quenched alloys should be carried out.

Stoichiomety (at%)	**Young's modulus (GPa)**
Ti (hcp)	105
Ti-25Hf	65
Ti-25Zr	63
Ti-12.5Zr-12.5Hf	64

Table 3.5.1 *Young's moduli of disordered Ti (hcp phase) and disordered polycrystalline Ti-25at%Hf, Ti-25at%Zr and Ti-12.5at%Zr-12.5at%Hf.*

3.4.5 References

1. M. Grandin, S. Berner, M. Dard. A Review of Titanium Zirconium (TiZr) Alloys for Use in Endosseous Dental Implants. Materials 5 (2012) 1348-1360 doi:10.3390/ma5081348.
2. Y. Ikarashi, K. Toyoda, E. Kobayashi, H. Doi, T. Yoneyama, H. Hamanaka, T. Tsuchiya. Improved Biocompatibility of Titanium–Zirconium (Ti–Zr) Alloy: Tissue Reaction and Sensitization to Ti–Zr Alloy Compared with Pure Ti and Zr in Rat Implantation Study. Materials Transactions, Vol. 46, No. 10 (2005) 2260-2267.
3. M.A. Khan, R.L. Williams, D.F. Williams. Conjoint corrosion and wear in titanium alloys. Biomaterials 20 (1999) 765–772.
4. N. Bernhard, S. Berner, M. De Wild, M. Wieland. The binary TiZr alloy - A newly developed Ti alloy for use in dental implants. Forum Implantol. 5 (2009) 30–39.
5. Y.M. Zhang, F. Chai, J.C. Hornez, C.L. Li, Y.M. Zhao, M. Traisnel, H.F. Hildebrand. The corrosion and biological behaviour of titanium alloys in the presence of human lymphoid cells and MC3T3-E1 osteoblasts. Biomedical Materials (2009) 4, doi: 10.1088/1748-6041/4/1/015004.
6. T. Naganawa, Y. Ishihara, T. Iwata, A. Koide, M. Ohguchi, Y. Ohguchi, Y. Murase, H. Kamei, N. Sato, M. Mizuno, T. Noguchi. In vitro biocompatibility of a new titanium-29niobium-13tantalum-4.6zirconium alloy with osteoblast-like MG63 cells. Journal of Periodontology 75 (2004) 1701–1707.
7. Y. Ikarashi, K. Toyoda, E. Kobayashi, H. Doi, T. Yoneyama, H. Hamanaka, T. Tsuchiya. Improved biocompatibility of titanium-zirconium (Ti-Zr) alloy: Tissue reaction and sensitization to Ti-Zr alloy compared with pure Ti and Zr in rat implantation study. Materials Transactions 46 (2005) 2260–2267.
8. L. Nie, Y. Zhan, H. Liu, C. Tang. Novel β-type Zr–Mo–Ti alloys for biological hard tissue replacements. Materials and Design 53 (2014) 8–12
9. Y.L. Zhou, M. Niinomi, T. Akahori. Dynamic Young's Modulus and Mechanical Properties of Ti–Hf Alloys. Materials Transactions, Vol. 45, No. 5, (2004) 1549-1554.
10. Y. Song, D. S. Xu, R. Yang, D. Li, W. T. Wu, and Z. X. Guo. Materials Science and Engineering A260 (1999) 269–274.

11. Y. Song, R. Yang, Z.X. Guo, D. Li. Structural Biomaterials for 21st Century, TMS (2001) 273–280.
12. H. Matsuno, A. Yokoyama, F. Watari, M. Uo, T. Kawasaki. Biocompatibility and osteogenesis of refractory metal implants, titanium, hafnium, niobium, tantalum and rhenium. Biomaterials 22 (2001) 1253–1262.
13. B.B. Sun, M.L. Sui, Y.M. Wang, G. He, J. Eckert, E. Ma. Ultrafine composite microstructure in a bulk Ti alloy for high strength, strain hardening and tensile ductility. Acta Materialia 54 (2006) 1349–1357.
14. A. Hynowska, A. Blanquer, E. Pellicer, J. Fornell, S. Suriñach, M.D. Baró, S. González, E. Ibáñez, L. Barrios, C. Nogués, J. Sort. Novel Ti–Zr–Hf–Fe Nanostructured Alloy for Biomedical Applications. Materials 6 (2013) 4930-4945; doi:10.3390/ma6114930.
15. S.K. Dolukhanyan, A.G. Aleksanyan, O.P. Ter Galstyan, V.Sh. Shekhtman, M.K. Sakharov, G.E Abrosi. Specifics of the Formation of Alloys and Their Hydrides in the Ti–Zr–H System, Russian Journal of Physical Chemistry vol. 2, no. 6 (2007) 563–569.
16. V.Sh. Shekhtman, S.K. Dolukhanyan, A.G. Aleksanyan, O.P. Ter Galstyan, D.G. Mailyan, M.K. Sakharov, S.S. Khasanov. The Peculiarities of Formation of Alloys Structure in the Ti–Zr–Hf–H System, in Proceedings of International Conferences on Hydrogen Materials Science and Chemistry of Carbon Nanomaterials (ICHMS'2007), Sudak (Ukraine), (2007) 128–131.
17. S.K. Dolukhanyan, A.G. Aleksanyan, V.Th. Shekhtman, A.H. Manthashyan, D.G. Mailyan, O.P. Ter Galstyan. New Technique for Producing the Alloys Based on Transition Metals, Chemical Journal of Armenia, vol. 60, no. 4 (2007). 545–559.
18. ISSN 1061 3862, International Journal of Self Propagating High Temperature Synthesis. Allerton Press Inc. Vol. 19, No. 1 (2010) 34–39.
19. I.P. Swainson, S.K. Dolukanyan, A.G. Aleksanyan, V.Sh. Shekhtman, D.G. Mayilyan, A.L. Yonkeu. Omega-phase in Ti-Hf-Zr alloys produced by the hydride-cycle method. Canadian Journal of Physics 88 (2010) 741–749.

CHAPTER 4: Conclusions

4.1 Concluding remarks

This thesis investigates the structural, electronic and mechanical properties of non-toxic Ti-based alloys aiming to understand the characteristics that can lead in the achievement of bone-like Young's modulus, e.g. the β-phase stability.

Initially, we studied the Ti-Nb alloys in the experimentally observed α′, ω, β and α″ phases. The total energy calculations revealed that the α′ and ω phases are stable in the Ti-($x \leq 6.25$)at%Nb and that the β phase becomes energetically favoured in Ti-($x \geq 18.75$)at%Nb), while the α″ phase may exist in the intermediate stoichiometries (Ti-($9.375 \leq x \leq 18.75$)at%Nb). In addition, it came out that in all phases the unit cell increases upon Nb substitution, in agreement with available XRD experimental data. The EDOS relates the minimum located at the Fermi level (E_F) of α′ and ω phases in Ti-($x \leq 9.375$)at%Nb with stability features at low Nb concentrations, while the partial EDOSs of the α′, ω, α″ and β exhibit maxima in the range from -3.5eV up to E_F that are due to the *d*-electrons. In line with the total energy, the EDOSs and the XRD results, the calculated Ti-Nb mechanical stability conditions revealed destabilization of the α′ and ω structures upon Nb addition and initiation of the β-phase stabilization for Nb-rich compositions (> 15at%Nb). The negative E and G values as well as the high (> 0.5) Poisson's ratio ν values may also be used as indicators for the instability of β-Ti-($x <$ 10at%)Nb. Moreover, the sequence of $E_{\omega} > E_{\alpha'} > E_{\alpha''} > E_{\beta}$ was found for the Young's moduli, while for the β-Ti-xNb ($15\text{at\%Nb} \leq x \leq 31.25\text{at\%}$) the calculated elastic modulus theoretically saturates to the E_{β} = 87GPa. Therefore, we expect that the experimentally observed E dependence with Nb composition (w-shaped curve) should be a weighted average of the various Ti-Nb phases. The Young's modulus surfaces exhibit enhanced anisotropy for the α′, ω and α″ phases, contrary to the β-phase. Interestingly, the β-Ti-Nb alloys may exhibit really low elastic moduli, under 30GPa in the [100] and equivalent [010] - [001] directions, while the sequence of $E_{\beta}[100] < E_{\beta}[110] < E_{\beta}[111]$ is predicted. Therefore, in order to achieve bone-like Young's moduli using the Ti-xNb alloys, a single β-phase crystal with Nb less than 10at% should be grown along the [001] direction.

Since the stabilization of β-Ti-xNb can be experimentally obtained at high Nb substitutions (x > 22at%), an alternative pathway to achieve low rigidity is by means of a third element substitution in Ti-xNb (x ≥ 18.5at%), as experimentally found for the case of Ti-Nb-Sn alloys (E = 50.7GPa). In this thesis two main categories concerning the third element were studied: a) *sp* dopants (like Sn and In) and b) *sd* dopants (like Hf). For all ternaries, the ab initio calculations found an almost linear increase of the lattice constants upon the third element substitutions, in line with the available XRD measurements, whereas Hf is responsible for the highest lattice constant values. The calculated total energies showed that the In/Sn/Hf atoms always prefer the Ti-first neighbourhood (Ti-FN), while the Nb-FN and Ti-Nb-FN environments are less energetically favoured.

The *sp*-dopants were substituted in the stable β-Ti25at%Nb compositions in order to understand the experimentally observed lowering of E for specific stoichiometries. Interestingly, the partial EDOSs of the Ti-25at%Nb-(x ≤ 8.33at%)In/Sn show that the dopant's *s*-electrons are responsible for the new really low energy states around -8eV for Sn and -7eV for In, which exhibit antibonding features with the neighbouring atoms, thus leading in a weakening of the chemical bonds and consequently in elastic softening. The *p*-electrons occupy the states between -3eV and -5eV, while the Ti *d*-electrons are mainly contributing in the Fermi level without really affecting the ternaries' EDOSs. For high In/Sn contents (≥ 12.5at%), more In-In or Sn-Sn may become first or second neighbours exhibiting strong σ-bond features between the dopants and antibonding character with the Ti or Nb neighbouring atoms at these new lowest energy states. This results in significant deterioration of the periodic symmetry of the electronic charge, an effect that could lead to mechanical instability of the β-phase.

Furthermore, the sd-electron Hf was substituted in the Ti-18.75at%Nb where the a″ phase was experimentally found for small Hf substitution and the α″ → β transition was achieved for Hf 16at%. The ab initio calculations revealed the emergence of a new energy state around -11eV due to Hf 4*f* in Hf-Hf interactions, which may exist above Hf 12.5at% and correlates the stabilization of the β-phase with the pure Hf transitions upon pressure. The contributions of the Hf 5*d* at the Fermi level or the Hf 6*p* at lower energies do not significantly alter the binary's EDOS features, while these results are supported by the electronic band energy calculations.

Besides the Ti-Nb-based alloys, we also considered the study of Ti-based with *sd* elements like with Zr and Hf (Ti-xZr-yHf, x, y = 0, 12.5at%, 25at%). In these cases interatomic potential models became available, thus allowing us to study more realistic systems (in sizes) using large scale molecular dynamics simulations. For these alloys, the radial distribution functions predict a polycrystalline structure when the system is rapidly quenched (10K/ps), while when lower cooling rates were employed (down to 0.1K/ps) the final structures were close to mono-crystalline systems. The corresponding alloys' Young's moduli (63-65GPa) are lower than the α-Ti (105GPa), but still comparable to the β-Ti-25at%Nb, i.e. higher than 60GPa.

The results of this thesis could be used for the design of low-rigidity non-toxic Ti-based alloys suitable for biomedical implants.

4.2 Future work

In this thesis, a detailed study of the structural, electronic and mechanical properties of several Ti-based alloys have been carried out. Nevertheless there are still some open questions and work that could be done as a continuation of this thesis.

The β-phase alloys with Nb additions close to 10at%Nb exhibit a very low Young's modulus. Unfortunately the β-Ti-Nb is unstable at low Nb concentrations. Consequently β-Ti-(x < 10at%)Nb-X alloys with non-toxic additions could be an option for the β-phase stabilization at such compositions. In particular, a study of Ti-Nb-X alloys with other biocompatible additions like Pd, Pt or Sc or with biodegradable compounds like Ca or Mg. The calculation of these alloys mechanical properties could also be a future topic. The β-phase of the Ti-xNb ($x \geq 18.5$at%) has been proven to be the energetically favoured with a Young's modulus highly dependent on the crystallographic direction. Due to that reason, methods like cold rolling, heat treatments or the addition of other dopants could favoured the growth of β grains along the [100] diminishing the growth along [111], leading us to further elastic moduli reduction.

Other interesting topic for future study could be related with the Ti-Nb systems' size scale-up by means of molecular dynamics. The simulations of large scale systems would help us to perform a more realistic study of the structural properties and tensile deformations in polycrystalline systems. In addition the influence of the stoichiometry, pressure and temperature in the phase transition and their possible influence in the mechanical properties could be analyzed in more detail. Unfortunately, classical MD simulations require an interatomic potential to describe all atoms interactions, which although can be found for Ti (hcp phase) and Nb (bcc phase) metals, is not available for the binary system. Nevertheless, considering the technical problems related to the molecular dynamics calculations, the system's size could also be scaled-up (up to ~200 atoms) by any DFT with pseudopotential methodology.

Finally, regarding the study of Ti-Zr-Hf system by molecular dynamics, a wider range of stoichiometries, as well as larger systems could be simulated in order to get a better understanding of the phase transitions and more accurate calculations of the mechanical properties.

ANNEX

Dissemination

The most important research results of this thesis have been or will be submitted for publication in peer-reviewed journals as well as presented in international conferences and workshop enumerated below.

Scientific publications

- The role of Sn doping in the β-type Ti-25at%Nb alloys: experiment and ab initio calculations
  J.J. Gutiérrez Moreno, Y. Guo, K. Georgarakis, A.R. Yavari, G.A. Evangelakis, Ch. Lekka
  Journal of Alloys and Compounds 615 (2014) S676–S679

- Elastic softening of β-type Ti-Nb alloys by indium (In) additions
  M. Calin, A. Helth, J.J. Gutiérrez Moreno, M. Bönisch, V. Brackmann, L. Giebeler, T. Gemming, Ch. Lekka, A. Gebert, R. Schnettler, J. Eckert
  Journal of the Mechanical Behavior of Biomedical Materials 39 (2014) 162-174

- Electronic origin of α" to β phase transformation in TiNb-based thin films upon Hf microalloying
  J.J. Gutiérrez Moreno, N.T. Panagiotopoulos, Ch.E. Lekka, G.A. Evangelakis
  Manuscript in preparation

- Ti-Nb phase transitions from electronic structure calculations
  Ch.E. Lekka, J.J. Gutiérrez Moreno, G.A. Evangelakis
  Manuscript in preparation

- Structural and electronic properties of Ti-Nb alloys
  J.J. Gutiérrez Moreno, G.A. Evangelakis, Ch.E. Lekka
  Manuscript in preparation

- Mechanical properties of Ti-Nb alloys
  J.J. Gutiérrez Moreno, G.A. Evangelakis, Ch.E. Lekka
  Manuscript in preparation

Dissemination in conferences

- Binary & Ternary Ti-based alloys: A Computational Study
  J.J. Gutiérrez Moreno, G.A. Evangelakis, D.G. Papageorgiou, Ch.E. Lekka
  BioTiNet Winter School
  Talk

- Biocompatible Ti-Nb-X (X = Sn, In, Hf) alloys from ab initio calculations
  J.J. Gutiérrez Moreno, G.A. Evangelakis, Ch.E. Lekka
  XXIX Panhellenic Conference on Solid State Physics & Materials Science
  Poster

- Biocompatible Ti-xNb (14<x<40) alloys: Structural, electronic and mechanical properties
  J.J. Gutiérrez Moreno, D.G. Papageorgiou, G.A. Evangelakis, Ch.E. Lekka, M. Boenisch, A. Helth, M. Calin, A. Gebert, J. Eckert
  Euromat 2013
  Poster

- Biocompatible Ti-Nb-X (X = Sn, In, Hf) alloys from ab initio calculations
  J.J. Gutiérrez Moreno, G.A. Evangelakis, Ch.E. Lekka
  Euromat 2013
  Poster

- Biocompatible Ti-xNb (14<x<40) alloys: Structural, electronic and mechanical properties
  J.J. Gutiérrez Moreno, D.G. Papageorgiou, G.A. Evangelakis, Ch.E. Lekka, M. Boenisch, A. Helth, M. Calin, A. Gebert, J. Eckert
  Euro LightMAT 2013
  Talk

- Structural, electronic and mechanical properties of β-Ti-Nb-Sn alloys: Experiment vs. ab-initio calculations
  J.J. Gutiérrez Moreno, G.A. Evangelakis, Ch.E. Lekka, Y. Gou, K. Georgarakis, A.R. Yavari
  ISMANAM 2013, 20th International Symposium on Metastable, Amorphous and Nanostructured Materials
  Poster

- Structural, electronic and mechanical properties of β-Ti-Nb-In alloys: Experiment vs. ab-initio calculations
  J.J. Gutiérrez Moreno, G.B. Bokas, G.A. Evangelakis, Ch.E. Lekka, A. Helth, M. Boenisch, A. Gebert, M. Calin, J. Eckert
  ISMANAM 2013, 20th International Symposium on Metastable, Amorphous and Nanostructured Materials
  Poster

- On the design of Ti-Nb-X (X = In, Sn, Hf) alloys from ab-initio calculations
  J.J. Gutiérrez Moreno, G.A. Evangelakis, D.G. Papageorgiou, Ch.E. Lekka
  4th BioTiNet workshop – Biomaterials for Orthopaedic Applications
  Talk

- On the design of Ti-Nb-X (X = In, Sn, Hf) alloys from ab-initio calculations
  J.J. Gutiérrez Moreno, G.A. Evangelakis, D.G. Papageorgiou, Ch.E. Lekka
  4th BioTiNet workshop – Biomaterials for Orthopaedic Applications
  Poster

- Biocompatible Ti-Nb and Ti-Nb-Hf thin films by magnetron sputtering and ab-initio calculations
  J.J. Gutiérrez Moreno, N.T. Panagiotopoulos, P. Patsalas, Ch.E. Lekka, G.A. Evangelakis
  EMRS 2013 SPRING MEETING
  Poster

- Structural, electronic and mechanical properties of β-Ti-Nb-Sn alloys: Experiment vs. ab-initio calculations
  J.J. Gutiérrez Moreno, G.A. Evangelakis, Ch.E. Lekka, Y. Gou, K. Georgarakis, A.R. Yavari
  EMRS 2013 SPRING MEETING
  Poster

- Theory-guided bottom-up design of low-rigidity Ti-based alloys (ab initio and MD calculations)
  J.J. Gutiérrez Moreno, G.A. Evangelakis, D.G. Papageorgiou, Ch.E. Lekka
  3rd BioTiNet workshop – Surface science & engineering
  Talk

- Theory-guided bottom-up design of low-rigidity Ti-based alloys (ab initio and MD calculations)
  J.J. Gutiérrez Moreno, G.A. Evangelakis, D.G. Papageorgiou, Ch.E. Lekka
  BioTiNet Mid-term review meeting
  Talk

- Structural, electronic and mechanical properties of Ti-xNb (Nb<40 at.%)
  J.J. Gutiérrez Moreno, N.T. Panagiotopoulos, D.G. Papageorgiou, G.A. Evangelakis, Ch.E. Lekka
  ISMANAM 2012, 19th Internat. Symposium on Metastable, Amorphous and Nanostructured Materials
  Poster **(Best poster award)**

- Structural, electronic and mechanical properties of β-Ti alloys by means of ab-initio calculations
  J.J. Gutiérrez Moreno, G.A. Evangelakis, D.G. Papageorgiou, Ch.E. Lekka
  BioTiNet summerschool – Titanium in medicine
  Talk

- Structural, electronic and mechanical properties of β-Ti alloys by means of ab initio calculations
  J.J. Gutiérrez Moreno, G.A. Evangelakis, D.G. Papageorgiou, Ch.E. Lekka
  2nd BioTiNet workshop – Research methodology and research project management
  Talk

- Towards Ti-based alloys for biomedical applications by means of ab-initio calculations
  J.J. Gutiérrez Moreno, G.A. Evangelakis, D.G. Papageorgiou, Ch.E. Lekka
  1st BioTiNet workshop – Advanced Methods for Materials Characterization
  Talk

- On the design of β Ti-based alloys for ab-initio calculations
  J.J. Gutiérrez Moreno, G. Bokas, N.T. Panagiotopoulos, G.A. Evangelakis, Ch.E. Lekka
  SCIENCE: Passion, Mission, Responsibilities
  Poster

SUPPLEMENTARY MATERIAL

Electronic Density of States for the understudy stoichiometries

a) TiNb

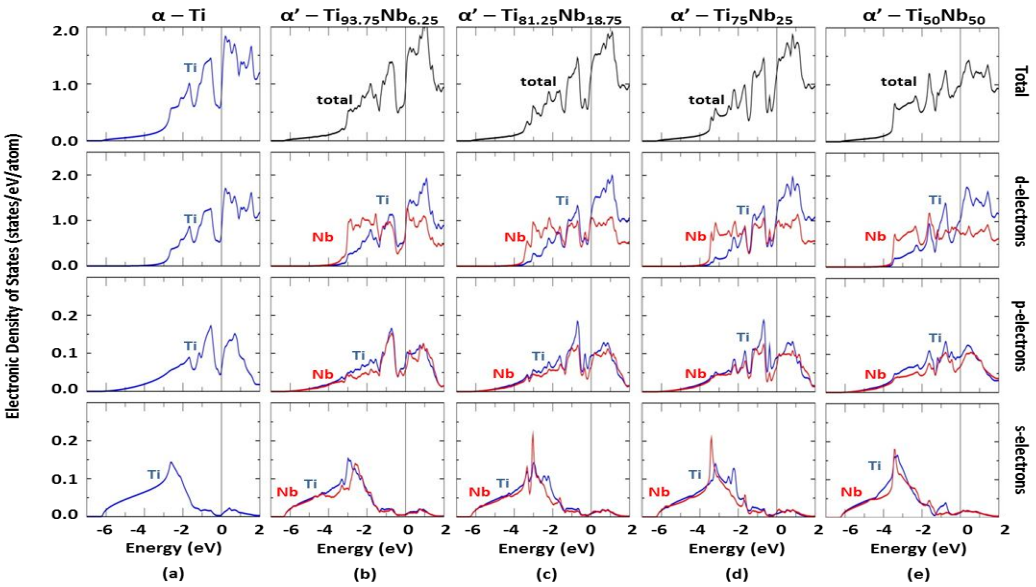

Figure SM 1 *Electronic density of states of α'-phase:* **a)** *pure α-Ti,* **b)** *Ti-6.25at%Nb,* **c)** *Ti-18.75at%Nb,* **d)** *Ti-25at%Nb and* **e)** *Ti-50at%Nb; for the total, d, p and s contributions (first up to fourth row, respectively).Blue lines stand for the Ti-partial contribution, red for the Nb-partial contribution and black for the total average.*

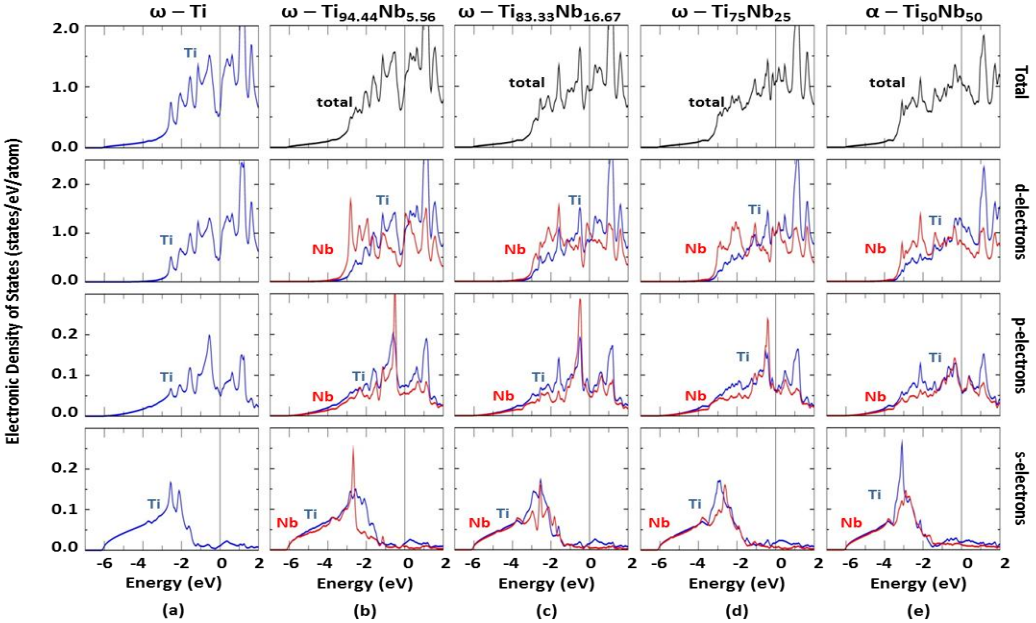

Figure SM 2 *Electronic density of states of ω-phase:* **a)** *pure Ti,* **b)** *Ti-6.25at%Nb,* **c)** *Ti-18.75at%Nb,* **d)** *Ti-25at%Nb and* **e)** *Ti-50at%Nb; for the total, d, p and s contributions (first up to fourth row, respectively).Blue lines stand for the Ti-partial contribution, red for the Nb-partial contribution and black for the total average.*

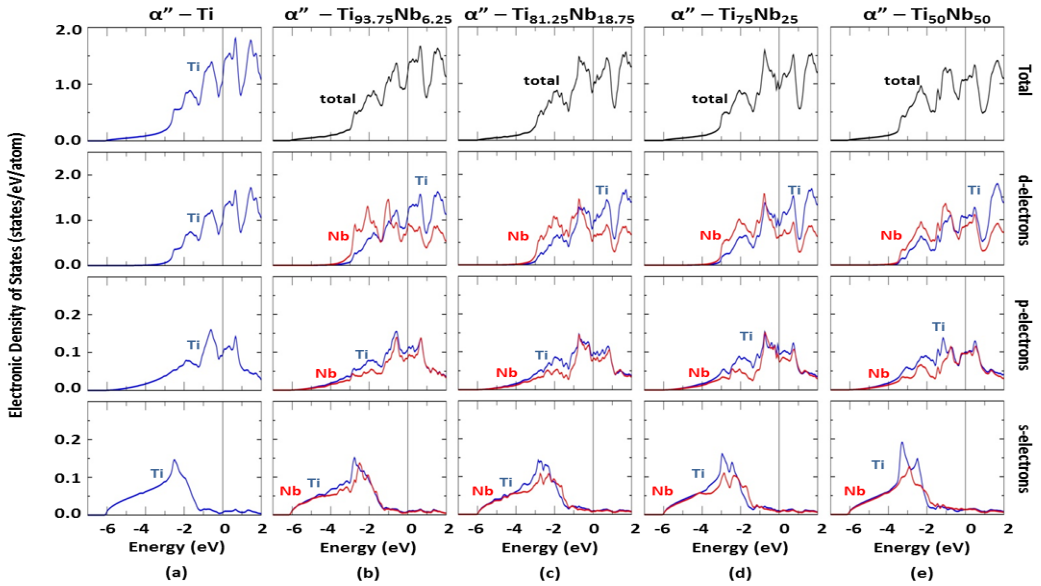

Figure SM 3 *Electronic density of states of α''-phase:* **a)** *pure α''-Ti,* **b)** *Ti-6.25at%Nb,* **c)** *Ti-18.75at%Nb,* **d)** *Ti-25at%Nb and* **e)** *Ti-50at%Nb; for the total, d, p and s contributions (first up to fourth row, respectively).Blue lines stand for the Ti-partial contribution, red for the Nb-partial contribution and black for the total average.*

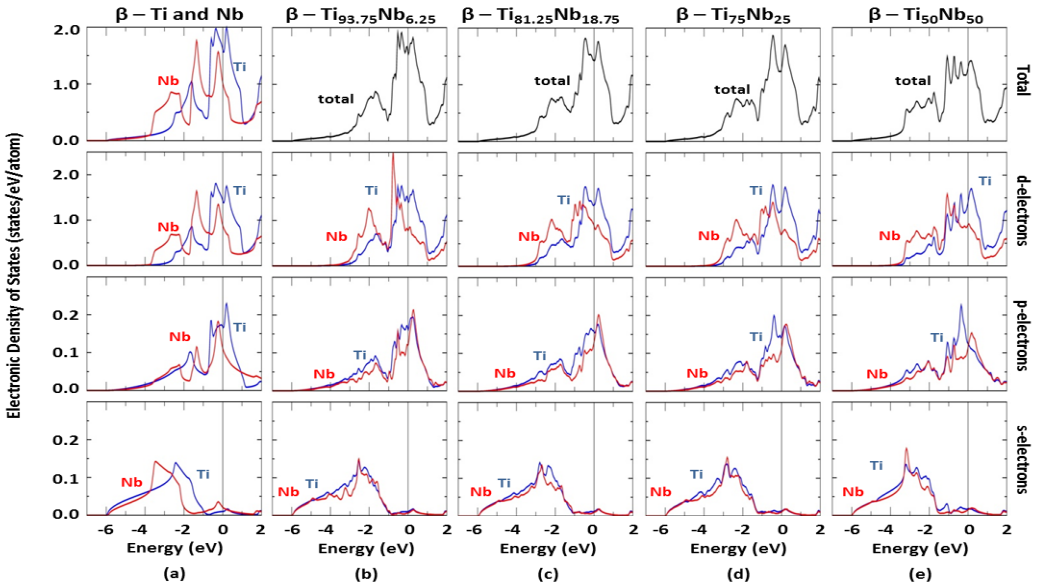

Figure SM 4 *Electronic density of states of β-phase:* **a)** *pure Ti and Nb,* **b)** *Ti-6.25at%Nb,* **c)** *Ti-18.75at%Nb,* **d)** *Ti-25at%Nb and* **e)** *Ti-50at%Nb; for the total, d, p and s contributions (first up to fourth row, respectively).Blue lines stand for the Ti-partial contribution, red for the Nb-partial contribution and black for the total average.*

b) TiNbHf

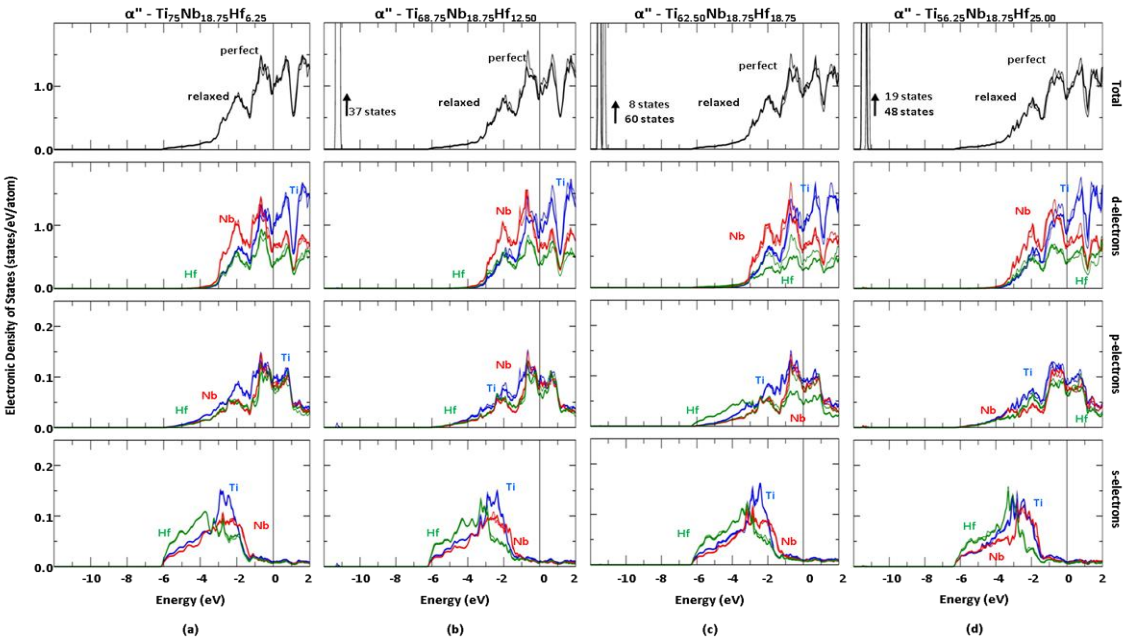

Figure SM 5 *Electronic density of states of α"-phase:* **a)** *Ti-18.75at%Nb-6.25at%Hf for the total, d, p and s contributions lied up from the first up to fourth row, respectively,* **b)**, **c)** *and* **d)** *stand for the cases of Ti Ti-18.75at%Nb-12.5at%Hf, Ti-18.75at%Nb-18.75at%Hf and Ti-18.75at%Nb-25at%Hf respectively. The contribution due to perfect ideal structure is represented by a thin line and the final structure after ionic relaxation with a thicker trace)*

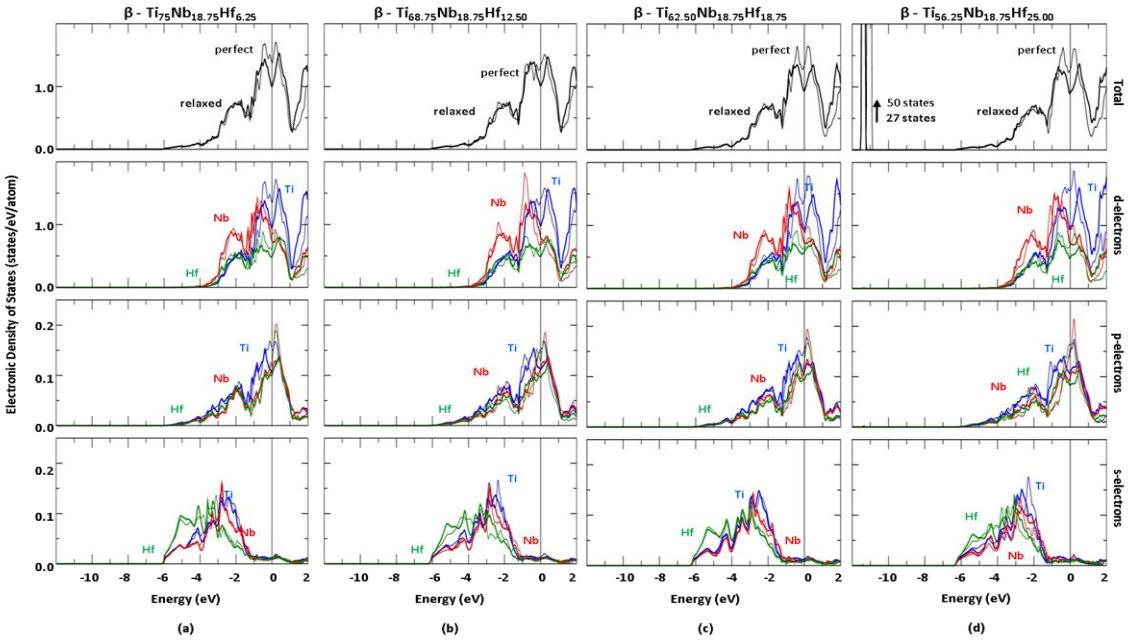

Figure SM 6 *Electronic density of states of β-phase:* **a)** *Ti-18.75at%Nb-6.25at%Hf for the total, d, p and s contributions lied up from the first up to fourth row, respectively,* **b)**, **c)** *and* **d)** *stand for the cases of Ti Ti-18.75at%Nb-12.5at%Hf, Ti-18.75at%Nb-18.75at%Hf and Ti-18.75at%Nb-25at%Hf respectively. The contribution due to perfect ideal structure is represented by a thin line and the final structure after ionic relaxation with a thicker trace)*

c) TiNbIn

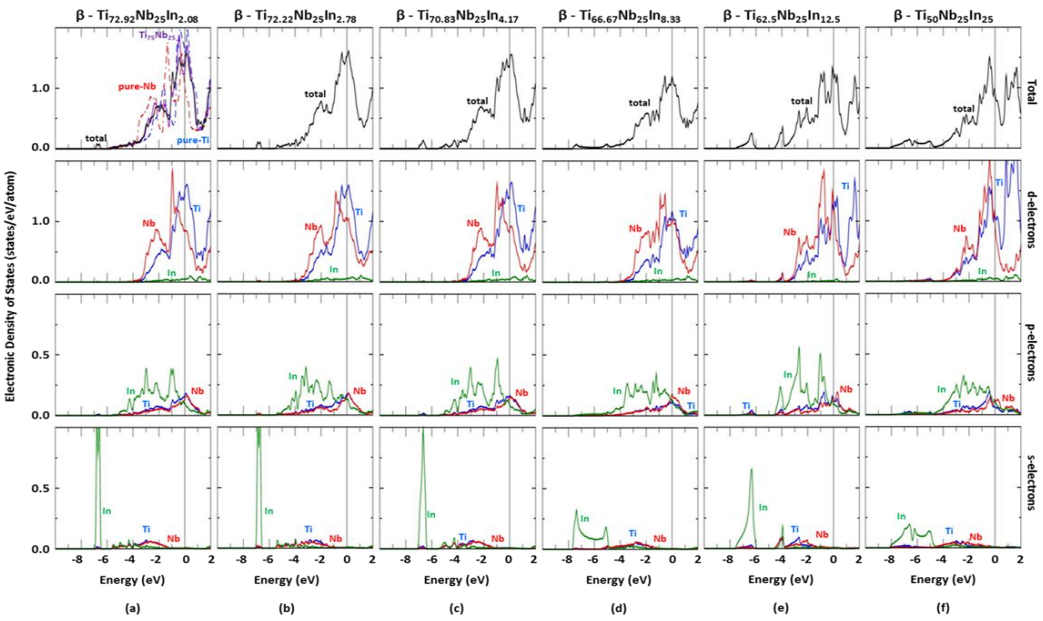

Figure SM 7 *Electronic density of states of β-phase:* **a)** *pure Ti, pure Nb, Ti-25at%Nb and Ti-25at%-2.08at%In (dotted blue, dotted red, purple and black lines, respectively) for the total, d, p and s contributions (first up to fourth row, respectively,* **b)**, **c)**, **d)**, **e)** *and f) stand for the cases of Ti-25at%Nb-2.78at%In, Ti-25at%Nb-4.17at%In, Ti-25at%Nb-8.33at%In, Ti-25at%Nb-12.5at%In and Ti-25at%Nb-25at%In respectively.*

d) TiNbSn

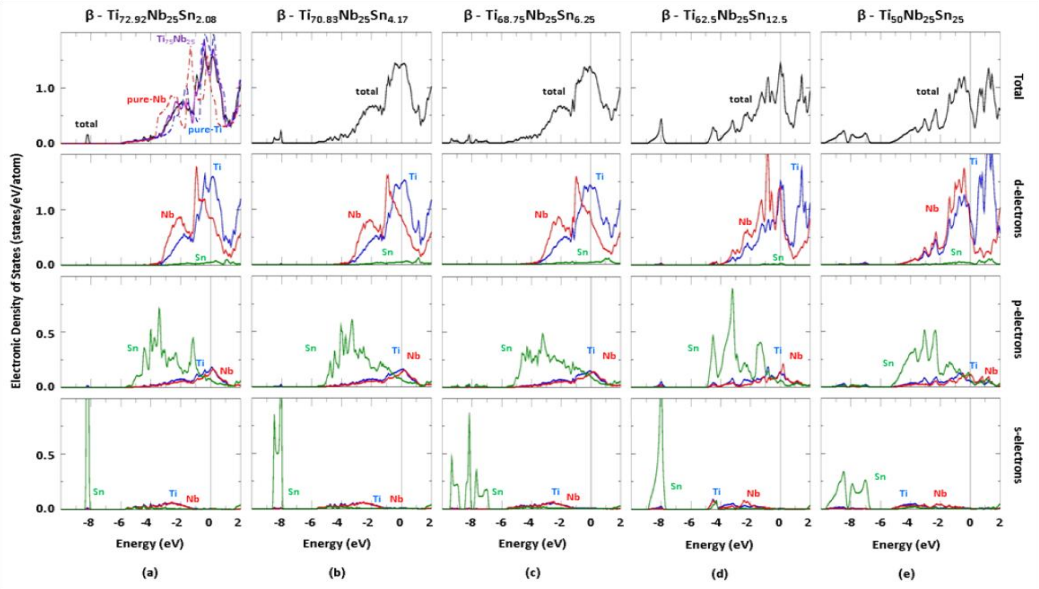

Figure SM 8 *Electronic density of states of β-phase:* **a)** *pure Ti, pure Nb, Ti-25at%Nb and Ti-25at%-2.08at%Sn (dotted blue, dotted red, purple and black lines, respectively) for the total, d, p and s contributions (first up to fourth row, respectively),* **b)**, **c)**, **d)** *and* **e)** *stand for the cases of Ti-25at%Nb-2.08at%Sn, Ti-25at%Nb-4.17at%Sn, Ti-25at%Nb-6.25at%Sn, Ti-25at%Nb-12.5at%Sn and Ti-25at%Nb-25at%Sn respectively.*